LONG TERM AND SAFE CLUSTER FLYING
FOR DISTRIBUTED SPACE SYSTEMS

A THESIS SUBMITTED TO
THE GRADUATE SCHOOL OF NATURAL AND APPLIED SCIENCES
OF
MIDDLE EAST TECHNICAL UNIVERSITY

BY

BURAK YAĞLIOĞLU

IN PARTIAL FULFILLMENT OF THE REQUIREMENTS
FOR
THE DEGREE OF DOCTOR OF PHILOSOPHY
IN
AEROSPACE ENGINEERING

JANUARY 2023

Approval of the thesis:

**LONG TERM AND SAFE CLUSTER FLYING
FOR DISTRIBUTED SPACE SYSTEMS**

submitted by **BURAK YAĞLIOĞLU** in partial fulfillment of the requirements for the degree of **Doctor of Philosophy** in **Aerospace Engineering, Middle East Technical University** by,

Prof. Dr. Halil Kalıpçılar
Dean, Graduate School of **Natural and Applied Sciences**　　　＿＿＿＿＿＿＿＿

Prof. Dr. Serkan Özgen
Head of the Department, **Aerospace Engineering**　　　＿＿＿＿＿＿＿＿

Prof. Dr. Ozan Tekinalp
Supervisor, **Aerospace Engineering, METU**　　　＿＿＿＿＿＿＿＿

Examining Committee Members:

Asst. Prof. Dr. Ali Türker Kutay
Aerospace Engineering, METU　　　＿＿＿＿＿＿＿＿

Prof. Dr. Ozan Tekinalp
Aerospace Engineering, METU　　　＿＿＿＿＿＿＿＿

Prof. Dr. Kemal Leblebicioğlu
Electrical and Electronics Engineering, METU　　　＿＿＿＿＿＿＿＿

Prof. Dr. Tahsin Çağrı Şişman
Astronautical Engineering, UTAA　　　＿＿＿＿＿＿＿＿

Prof. Dr. Gerhard Wilhelm Weber
Faculty of Engineering Management, PUT　　　＿＿＿＿＿＿＿＿

Date: 24.01.2023

I hereby declare that all information in this document has been obtained and presented in accordance with academic rules and ethical conduct. I also declare that, as required by these rules and conduct, I have fully cited and referenced all material and results that are not original to this work.

Name Last name : Burak Yağlıoğlu

Signature :

ABSTRACT

LONG TERM AND SAFE CLUSTER FLYING
FOR DISTRIBUTED SPACE SYSTEMS

Yağlıoğlu, Burak
Doctor of Philosophy, Aerospace Engineering
Supervisor: Prof. Dr. Ozan Tekinalp

January 2023, 173 pages

To fill the gap between the formation flying and swarm missions, cluster flying is introduced with relatively loose geometry constraints and control accuracy requirements as well as considering more spacecraft compared to formation flying which typically accommodates two spacecraft (a leader and a follower). The problem of long-term relative orbit design for and maintenance of spacecraft clusters with realistic operational considerations such as safety, station keeping and inter-spacecraft distance constraints is addressed. Two different methodologies of cluster flying design are developed in terms of station keeping and safety objectives. In the first methodology, relative orbit configurations are found minimizing deviations from reference mean orbit which would maximize the station-keeping objective. In second one, relative configurations are found from a reference initial condition by minimizing probability of collision, hence maximizing the safety objective, between the spacecraft in the cluster which are propagated numerically through a high precision orbit propagator. For the design optimization, a derivative free algorithm is proposed. Effectiveness of the methodologies is demonstrated through simulations. Using this design framework, several configurations can be found by exploring the limits of the clusters in terms of spacecraft number, distance bounds

and probabilities of collision for long time intervals and various mission requirements. To accommodate different types of missions, the problem of radio frequency geolocation cluster design is also addressed. For maintenance of the clusters, reconfiguration algorithms are developed to minimize total maneuvering effort while maximizing station-keeping and ensuring safety objectives. In the first algorithm, sequential cluster configurations are found by minimizing deviations from a reference mean orbit for long time intervals and, then, spacecraft are associated into new configurations using auction algorithm which minimizes total maneuvering effort for whole cluster. For reconfiguration, optimal impulsive transfer, model predictive control and nonlinear optimal control methodologies with linear time invariant and time variant dynamic models are implemented and compared. Finally, another reconfiguration algorithm is proposed by considering relative orbital element differences as design variables and its effectiveness is shown in terms of significantly improved maneuvering requirements for whole cluster. With the developed cluster flying framework, it becomes possible to assess what type of clusters are operationally possible or not for a given set of parameters regarding constraints, availabilities, capabilities, physical characteristics, navigation uncertainties and mission requirements. Therefore, the proposed framework is a powerful design and operational analysis tool for maximizing the feasibility and mission return of cluster missions. In this manner, different types of clusters with specific mission requirements can be designed and evaluated with reasonable or small computational demand for long term uninterrupted service and safety in all phases of distributed space missions.

ÖZ

DAĞITIK UZAY SİSTEMLERİ İÇİN
UZUN VADELİ VE GÜVENLİ KÜME UÇUŞU

Yağlıoğlu, Burak
Doktora, Havacılık ve Uzay Mühendisliği
Tez Yöneticisi: Prof. Dr. Ozan Tekinalp

Ocak 2023, 173 sayfa

Koluçuşu ve sürü görevleri arasındaki boşluğu doldurmak amacıyla görece daha az geometrik kısıt ve kontrol doğruluğu gerektiren ve genellikle lider ve takipçi olmak üzere iki uzay aracı olarak düşünülen koluçuşu problemlerine göre daha fazla uzay aracı hesaba katılan küme uydu uçuşu tanımlanmıştır. Küme uçuşları için uzun vadeli bağıl yörüngelerin tasarımı ve idamesi problemi güvenlik, mevzi koruma ve uzay araçları arası mesafe kısıtları gibi gerçekçi operasyonel etmenler ile birlikte ele alınmıştır. Küme uydu uçuşu tasarımı kapsamında mevzi koruma ve güvenlik amaçlarının ele alındığı iki farklı yöntem geliştirilmiştir. İlk yöntemde, bağıl yörünge konfigürasyonları, referans bir ortalama yörünge etrafındaki sapmalar en aza indirilerek dolayısıyla mevzi koruma amacı en iyilenerek bulunmaktadır. İkinci yöntemde ise bağıl yörünge konfigürasyonları referans bir ilk durumdan yüksek doğruluklu sayısal bir yörünge ilerletici vasıtasıyla ilerletilen uzay araçları arasındaki çarpışma olasılığı en aza indirilerek dolayısıyla güvenlik amacı en iyilenerek bulunmaktadır. Tasarım eniyilemesi için türevsiz bir algoritma geliştirilmiştir. Yöntemlerin etkinliği çeşitli benzetimler yoluyla gösterilmiştir. Bu tasarım yaklaşımı ile uzun vadeli ve farklı görev gereksinimleri için uzay aracı sayısı, mesafe kısıtları ve çarpışma olasılıkları hesaba katılarak çeşitli konfigürasyonların

bulunması mümkün kılınmaktadır. Farklı görev gereksinimlerinin değerlendirilmesi kapsamında radyo frekanslı yer konumlandırma sistemi için küme uçuşu tasarımı problemi ele alınmıştır. Uzay aracı kümelerinin idamesi kapsamında ise mevzi koruma amacını eniyilerken ve güvenlik amacını temin ederken toplam manevra gereksinimini en aza indiren yeniden kümelenme algoritmaları geliştirilmiştir. İlk algoritma ile uzun zaman aralıkları için referans bir ortalama yörünge etrafındaki sapmaları en aza indiren ardışık küme konfigürasyonları bulunarak açık artırma ile toplam manevra gereksinimini tüm küme için en aza indirecek şekilde uzay araçlarının yeni kümelere tahsis edilmesi sağlanmaktadır. Yeniden kümelenme için, eniyilenmiş tek ateşlemeli transfer, model öngörülü kontrol ve doğrusal olmayan eniyilenmiş kontrol yöntemleri doğrusal-zaman bağımsız ve zaman bağımlı dinamik modeller uygulanmış ve karşılaştırılmıştır. Son olarak, bağıl yörünge elemanlarına küçük farkların eklenmesi yoluyla başka bir yeniden kümelenme algoritması geliştirilmiş ve bu yöntemin etkinliği tüm küme için manevra gereksiniminin kayda değer şekilde düşürülmesi yoluyla gösterilmiştir. Geliştirilen küme uçuşu yöntemleri ile belirli kısıtlar, imkanlar, kabiliyetler, fiziksel özellikler, seyrüsefer belirsizlikleri ve görev gereksinimleri ele alınarak hangi tip kümelerin operasyonel olarak mümkün olup olmadığı değerlendirilebilmektedir. Böylelikle, geliştirilen yöntemler küme uçuşu görevlerinin elverişliliğini ve bu görevlerinden elde edilecek değeri eniyileyen oldukça güçlü tasarım ve operasyonel analiz araçları sağlamaktadır. Bu bağlamda, belirli görev gereksinimlerine sahip çeşitli türlerdeki kümeler, dağıtık uzay sistemlerinin tüm evrelerinde hatrı sayılır veya düşük hesaplama ihtiyacı ile uzun vadeli ve güvenli olarak kesintisiz hizmet verecek şekilde tasarlanarak değerlendirebilmektedir.

Anahtar Kelimeler: Uzay Aracı Küme Uçuşu, Dağıtık Uzay Sistemleri, Yüksek Doğruluklu Bağıl Yörünge Tasarımı ve Analizi, Çarpışma Önleme, Yeniden Kümelenme

To Feray and my Little Moon

ACKNOWLEDGEMENTS

TABLE OF CONTENTS

LIST OF TABLES

LIST OF FIGURES

FIGURES

xvi

LIST OF ABBREVIATIONS

ABBREVIATIONS

CDF: Cumulative Distribution Function

CSpOC: Combined Space Operations Center

DOP: Dilution of Precision

ECI: Earth Centered Inertial

ECEF: Earth Centered Earth Fixed

ESOC: European Space Operations Center

FDOA: Frequency Difference of Arrival

FoV: Field of View

HCW: Hill-Clohess-Wiltshire Equations

LEO: Low Earth Orbit

LHS: Latin Hypercube Sampling

LVLH: Local Vertical Local Horizontal

LTAN: Local Time of the Ascending Node

LTI: Linear Time Invariant

LTV: Linear Time Variant

MPC: Model Predictive Control

MPS: Monopropellant Propulsion System

NOC: Nonlinear Optimal Control

OIT: Optimal Impulsive Transfer

PDF: Probability Density Function

PoC: Probability of Collision

qns: Quasi Non-Singular

RAAN: Right Ascension of the Ascending Node

RF: Radio Frequency

RFGL: Radio Frequency Geolocation

RK4: Runge-Kutta fourth-order method

RTN: Radial, Transversal and Normal

SGP4: Simplified General Perturbations Model No. 4

SSO: Sun Synchronous Orbit

STM: State Transition Matrix

TDOA: Time Difference of Arrival

TEME: True Equator Mean Equinox

TLE: Two-Line Elements

UT: Unscented Transform

LIST OF SYMBOLS

SYMBOLS

μ: Gravitational Constant

$R_\oplus$: Radius of Earth

J_2: Constant of Earth's Oblateness

a: Semi-major Axis

e: Eccentricity

i: Inclination

Ω: Right Ascension of Ascending Node

ω: Argument of Perigee

ν: True Anomaly

M: Mean Anomaly

E: Eccentric Anomaly

n: Mean Motion

ε: Orbital Energy

$\vec{r}$: Position Vector

$\vec{r}_A$: Position Vector in Frame A

$\mathcal{R}_A$: Rotation Matrix about Axis A

β_B^A: Transformation Matrix from Frame A to Frame B

m_i: Mass of Spacecraft

C_r: Solar Radiation Pressure Coefficient

A_r: Solar Radiation Pressure Area

ρ: Atmospheric Density

C_d: Drag Coefficient

A_d: Drag Area

β^*: Drag Parameter for SGP4 Theory

$\alpha_{i,j}^A$: Orbital Element Vector of Spacecraft i at Instant j of Type A

$\Delta\alpha_i^A$: Relative Orbital Element Vector of Spacecraft i of Type A

Φ: State Transition Matrix

Γ: Control Input Matrix

C_k^N: Number of k combinations of the set that has N elements

$X_{i,j}^A$: Cartesian State Vector of Spacecraft i at Instant j Expressed in Frame A

$\Delta X_{n,j}^A$: Relative Distance Vector of Combination n at Instant j Expressed in Frame A

$P_{i,j}$: Covariance Matrix of Spacecraft i at Instant j

P_c: Probability of Collision

$PoC_{n,j}$: Probability of Collision of Combination n at Instant j

r_c: Radius of Conjunction Area

σ_i: Standard Deviation in Direction i

ρ_i: Design Variables for Spacecraft i

$RO_{i,tj}$: i^{th} Relative Orbit at Time Interval tj

$\Delta V_{i,j}^A$: Delta Velocity Vector of Spacecraft i at Instant j Expressed in Direction A

CHAPTER 1

INTRODUCTION

Distributed space systems are utilized when there is a need for common observation of a region with multiple sensors, parallel observation of multiple regions, improved coverage, revisit or response time over a region of interest, realization of interferometry missions with long baselines, spacecraft networks and/or improved understanding and resolution through sensor fusion. Distributed space systems not only realize such needs but also offer flexibility (scalability, evolvability, maintainability, adaptability, etc.) and robustness (survivability, fault tolerance, reliability, etc.). Missions that utilize distributed space systems can be categorized with respect to inter-spacecraft distances and required control accuracy (Gill, 2011) which is illustrated in Figure 1.1.
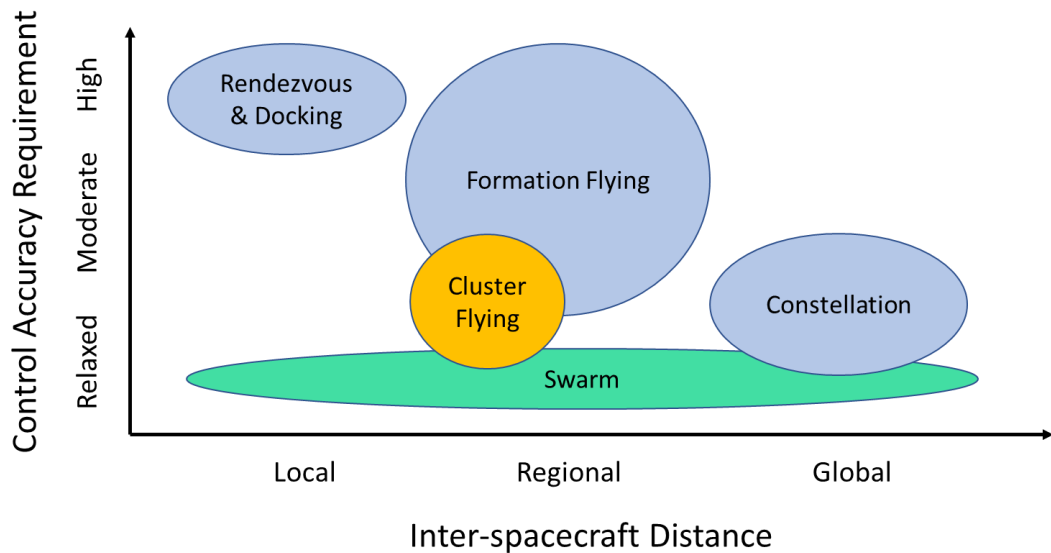
Figure 1.1. Categorization of Distributed Space Missions in terms of Distance and Control Accuracy

Here, local systems with separations between the spacecraft of a few meters can be referred as rendezvous and docking; regional systems with separations from a few 10 meters to several hundreds of kilometers can be referred as formation flying and global systems with separations of more than a thousand kilometers can be referred as constellations. The control accuracy requirements are the most stringent for rendezvous and docking where the inter-spacecraft distances are lowest. For formation flying, the mission objectives drive the requirements on the control accuracy. For instance, the control accuracy demand becomes high for a mission with tight geometry constraints. However, missions that would not require such tight geometry constraints can be handled with relatively less control accuracy. In addition, swarm missions with thousands of spacecraft can be considered to support collecting in-situ data with local, regional and global coverage. The drawback of swarms would be the limited control accuracy for individual spacecraft because of the limited budget per spacecraft for such a system.

Another categorization of distributed space systems can be in terms homogeneity of the system. Here, a distributed space system can be called homogeneous if all the spacecraft are identical in a system and heterogeneous if all the spacecraft are totally different. A third category can be named as hybrid with combination of identical and totally different spacecraft. These categories are illustrated in Figure 1.2.
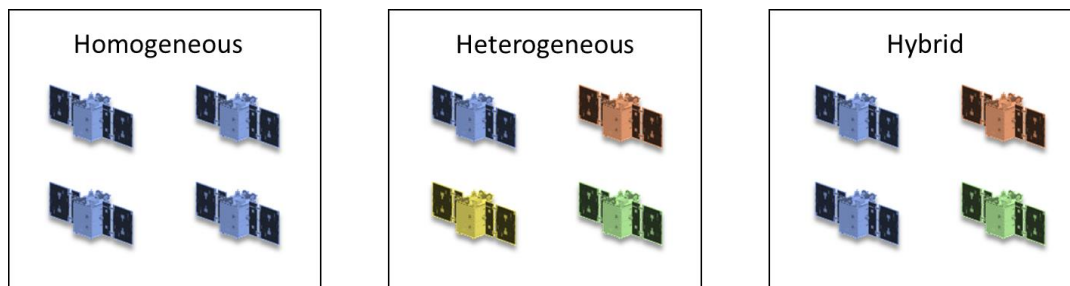
Figure 1.2. Categorization of Distributed Space Missions in terms of Homogeneity

The differences between systems may occur in terms of physical characteristics such as mass, area, shape, ballistic coefficient, inertia, reflectivity parameters, etc.; capabilities such as sensor and actuator performances, propellant mass, etc. and

availabilities due to mission requirements, failures, limited resources, etc. In this study, mainly physical characteristics are referred when considering heterogeneous systems.

To fill the gap between the formation flying and swarm missions, cluster flying is introduced with relatively loose geometry constraints and control accuracy requirements and more spacecraft are considered compared to formation flying which typically accommodates two spacecraft (a leader and a follower). However, as it will be explained in detail, there are several considerations to be addressed for cluster flying. Mainly, passively safe relative orbit configurations to support long-duration semi-autonomous operations shall be provided. This would also require incorporating realistic operational constraints such as station-keeping, collision or evaporation avoidance as well as mission/spacecraft specific parameters, constraints, capabilities and availabilities. Finally, sustaining a system with specific number of spacecraft for long term requires not only designing cluster configurations but also reconfiguration in the case of violation of a safety and/or distance constraints. Therefore, propellant optimal configuration and reconfiguration solutions are also vital for the feasibility and mission return of such cluster missions.

In this manner, it is aimed in this thesis to propose a set of algorithms that enable the long-term station keeping and reconfiguration of distance bounded multi-spacecraft clusters under realistic operational considerations. These considerations include safety and availability as well as spacecraft physical characteristics, capabilities, navigation uncertainties and high-fidelity orbital dynamics.

1.1   Literature Survey of Cluster Flying for Distributed Space Missions

(Brown & Eremenko, 2006) discusses that distributed space systems and spacecraft clusters have several advantages when compared to missions carried out using single spacecraft in terms of flexibility and robustness which would increase the net value or mission return. (Selva, et al., 2017) provides an extensive summary and

assessment of modern concepts and key enabling technologies of distributed functionality in space. One of the important factors for these distributed space systems is the design of relative orbit configurations for a cluster of spacecraft. For the case of cluster flying with a heterogeneously distributed system, it can be considered that a number of spacecraft, differing in platform characteristics, fly closely in formation with relatively loose geometry constraints (Yaglioglu B. , 2011). In this manner, there are several aspects to consider for the realization of cluster flying in terms of safety, and inter-spacecraft communication availability in addition to the regular station keeping and mission operations constraints (Yaglioglu & Wang, 2011).

So far, design and control of relative motion are widely studied in academia and industry with an emphasis on station keeping and/or reconfiguration objectives and constraints. Among these, (D'Amico & Montenbruck, 2006) provided a basis for relative orbit design with safety considerations by developing the parallel separation of relative E/I vectors method for Low Earth Orbit (LEO) close proximity formation flying missions. (Yaglioglu & Wang, 2011) and (Wang & Nakasuka, 2012) adopt the relative E/I vectors method to propose an intuitive cluster flying design method with passive relative orbits for fractionated spacecraft incorporating visibility and safety constraints. (Lim, Jung, & Bang, 2018) also uses this method to achieve safe formation keeping. (Hur-Diaz & O'Connor, 2014) discusses the application of cluster flying for fractionated space systems. Guidance problems with safety objective are also studied by (Wen, Zhang, & Gurfil, 2015) and (Pengfei, Xiaoqian, & Yong, 2019) for clusters especially after deployment from launchers. However, (Scharf, Hadaegh, Y., & Ploen, 2003) noted that the usefulness of passive relative orbits depends on the fidelity of the model used in their design because minimal disturbances prolonged over the mission lifetime affect formation keeping, and thus hinder the functions enabled by precise relative positioning. In addition, (Campbell, 2005) introduces a quantitative safety measure based on contours of probability, defined using state uncertainty ellipsoids, which are used to monitor and predict potential collisions over time.

Also, the relative dynamics, guidance, navigation, coordination, control, reconfiguration and optimization issues has been well studied in the literature by (Tillerson, Inalhan, & How, 2002), (Scharf, Hadaegh, Y., & Ploen, 2003), (Schaub & Junkins, 2003), (Scharf, Hadaegh F., & Ploen, 2004), (Alfriend & Yan, Evaluation and Comparison of Relative Motion Theories, 2005), (Alfriend, Vadali, Gurfil, How, & Breger, 2010), (Mueller, Griesemer, & Thomas, 2013), (Morgan, Chung, & Hadaegh, Model Predictive Control of Swarms of Spacecraft Using Sequential Convex Programming, 2014), (Morgan, Subramanian, P., Chung, & Hadaegh, 2016) and (Sullivan, Grimberg, & D'Amico, 2017). This wide literature provides an insight on the formulation of the relative dynamics, definition of constraints and linearization techniques. In addition to these, (Wang, Mengali, Quarta, & Yuan, 2017) and (Zhang, Dang, Fan, & Wang, 2017) introduce useful tools to calculate minimum and maximum relative distances effectively. (Paek, Kim, & de Weck, 2019) presents a framework for designing reconfigurable satellite constellations based on sampling and derivative free optimization techniques. A recent methodological development of cluster control algorithms supporting the various use cases of the mission with an emphasis on the algorithm's structure, information flow, and implementation is presented by (Edlerman & Gurfil, 2019). Finally, the latest developments in robust and safe cluster design and control applications with perturbed near-circular orbits are provided by (Koeing & D'Amico, 2018).

This important literature guides the development of an infrastructure for cluster flying design; however, a wholistic approach utilizing these building blocks with realistic considerations for long term cluster flying design and maintenance is still to be developed and/or advanced.

1.2 Thesis Overview

To provide an insight of this thesis work, the posed research questions, original contributions and thesis organization are summarized in following subchapters.

1.2.1 Research Questions

While conducting research on passively safe relative orbit configurations to support long-duration semi-autonomous spacecraft cluster operations, several research questions are posed:

- How to distribute multiple spacecraft into passively safe relative orbits?
- Are passively safe relative orbit configurations over long time intervals (~days) possible?
- How to incorporate the station-keeping and distance constraints as well as navigation uncertainties?
- How to distribute multiple spacecraft to sequential long-term relative orbits?
- How to transfer a cluster of spacecraft from the current configuration to the next one minimizing maneuver effort?

1.2.2 Original Contributions

The presented work in this thesis is aimed at improving the time validity analysis of cluster configurations and the fidelity of cluster flying design by incorporating realistic orbital dynamics, spacecraft parameters and navigation uncertainties as well as operational considerations. In terms of realistic dynamics, a high-fidelity orbit propagation is utilized to harness the natural dynamics in benefit of cluster flying design to reduce unnecessary control and therefore propulsion activities. In addition, heterogeneous systems with differences in spacecraft parameters and their effects on the dynamics of relative motion are considered inherently while designing cluster configurations. In terms of operational considerations and constraints, safety is treated not only as a constraint but another objective in addition to the traditional station keeping objectives and distance constraints. While addressing these, one method is developed to define general boundaries of a cluster with relatively less computational demand. On the other hand, another method is developed to maximize the safety for a cluster in the existence of navigation uncertainties with high fidelity

and, therefore, relatively higher computational demand. However, both methods can be used to design cluster configurations and assess their time validity (until control actions are necessary) whether in a design or operations phase of a cluster mission. To elaborate more, the objective function in first method is defined such that the deviation from a reference orbit for each spacecraft within the cluster is minimized, hence maximizing the station-keeping objective. In the second one, state or navigation uncertainties are also considered and the probability of collision between the spacecraft is minimized with the aim of maximizing the safety objective. For both approaches, minimum and maximum bounds on distances between the spacecraft and on the design variables (relative orbital elements) are defined by considering realistic mission and system specific parameters such as minimum and maximum ranges. In addition, different physical characteristics are introduced through drag parameters and the radiation pressure parameters in order to simulate a heterogeneous system. Finally, these two approaches are formulated and solved providing passively safe long-term operations which would not require any reconfiguration over a specific time interval therefore maximizing the mission return without any maneuver operation.

For cases when the time validity of a cluster is exceeded, i.e. the constraints are violated, the reconfiguration solutions are also found. Here, sequential cluster configurations are found by minimizing the total maneuvering effort for whole cluster while bounding deviations from a reference mean orbit for long time intervals. The optimal reconfiguration is investigated via model predictive control as well as nonlinear optimal control. The minimization of total maneuvering effort is realized through generating delta-V maps and associating relative orbits on the current configuration to the next one using an auction algorithm. Finally, to reduce total maneuvering effort further, reconfigurations are also found by slightly modifying individual relative orbits that still satisfies the cluster flying requirements.

To sum up original contributions can be summarized as follows:

- Utilization of a high-fidelity orbit propagation for cluster flying design,

- Consideration of heterogeneous systems with different physical parameters,
- Cluster flying design methodology supporting time validity analyses,
- Cluster flying design methodology identifying general time-space boundaries with less computational demand,
- Cluster flying design methodology with consideration of safety as an objective through minimizing probability of collision,
- Reconfiguration algorithm that supports cluster time-space validity through sequential design of clusters,
- Reconfiguration algorithm that considers spacecraft capabilities while minimizing total maneuvering effort for whole cluster.

1.2.3   Thesis Organization

A general guide to the cluster flying design and evaluation methodologies which are developed in this thesis is provided here. In Chapter 2, the high-fidelity modeling and analysis of absolute and relative motion are provided. This chapter serves as the introduction and validation of orbital dynamics models that are utilized for the cluster flying design and evaluation. In Chapter 3, the formulations and algorithms used in this thesis are introduced. First, the methodologies and related assumptions for relative orbit design and propagation as well as uncertainty propagation and calculation of collision probability are summarized. Then, the constraints, objective functions and design variables are defined. Finally, the methodology and the proposed algorithm for the design space exploration and optimization are provided. In Chapter 4, Chapter 5 and Chapter 6 cluster flying design cases are introduced with their results for maximizing the station keeping and safety objectives as well as minimizing dilution of precision respectively. In Chapter 7, reconfiguration methodology for spacecraft clusters is introduced. Here, two-impulse optimal transfer, model predictive control and nonlinear optimal control strategies are also compared. At the end of the thesis, the major outcomes, conclusions and potential future work items are summarized.

CHAPTER 2

HIGH FIDELITY MODELING AND ANALYSIS OF ABSOLUTE AND RELATIVE ORBITAL MOTION

In this chapter, the construction of a highly accurate absolute orbit and relative orbit models are introduced. For predicting orbital motion with high accuracy, it is necessary to consider all related aspects which include reference frames and systems, instantaneous and long-term orbit representation, perturbation effects, maneuvering and propagation of orbits. All these aspects are introduced and explained in the following subchapters.

2.1   Representation and Propagation of Orbital Motion

2.1.1   Reference Frames and Systems for Orbital Motion

The representation and derivation of equations of motion for the orbital motion require the definition of reference frames and systems. Here, reference frames, systems and coordinates can be differentiated as follows:

- Coordinate System is a mathematical expression for representation where the origin and orientation of the axes are defined.
- Reference Frame is the materialization of a reference system in real world where specification of elements and assumptions for realization are defined.
- Reference System is formed by specification of the reference frame and its origin where it consists of the adopted coordinate system, a set of constants, models and parameters.

For orbital motion, inertial, body fixed and local reference frames can be considered. The ones utilized in this thesis are briefly introduced as follows:

2.1.1.1   Earth Centered Inertial (ECI) Frame

An inertial frame has a fixed orientation in space and therefore the axes of the coordinate system do not rotate. Also, the Newton's 2nd law is valid in this frame. In this thesis, the assumptions of the inertial frame are defined as follows:

- Coordinate System: Cartesian
- Origin: Center of mass of the Earth
- Orientation of Axes: Fixed inertial direction along the intersection of the Earth's equatorial plane and the ecliptic. X axis points at Vernal Equinox at 1 January 2000, 11:58:55.816 [UTC], Z axis points along the spin axis of Earth at same time and Y axis completes right-handed coordinate system.
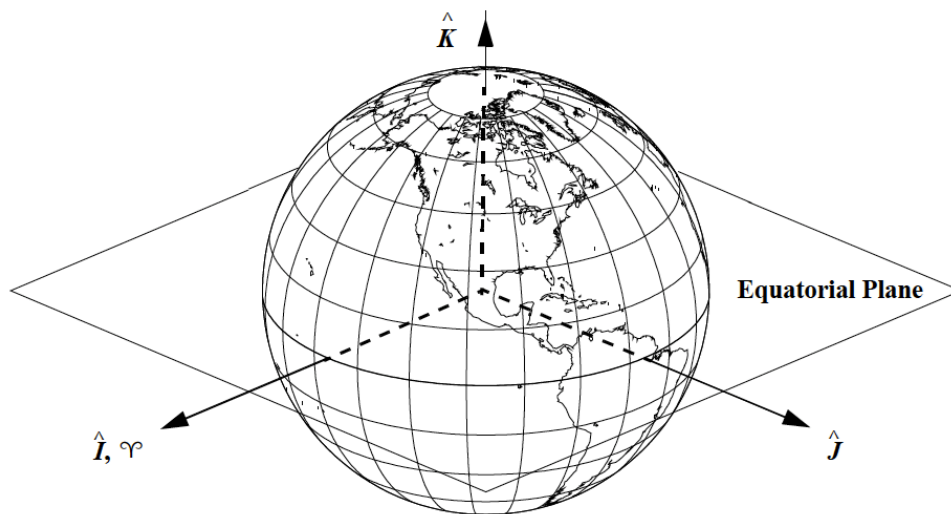
Figure 2.1. Representation of Earth Centered Inertial Frame with unit vectors I, J, K for X, Y, Z directions respectively where X points at Vernal Equinox ♈. (Vallado, 2013)

The ECI frame defined here is also referred as J2000. In addition to J2000, there is also True Equator Mean Equinox (TEME) which is another Earth centered inertial frame defined as:

- Coordinate System: Cartesian
- Origin: Center of mass of the Earth
- Orientation of Axes: Z axis points toward the true rotation axis at the current epoch, X axis points toward the mean vernal equinox at the current epoch and Y axis completes right-handed coordinate system.

The distinction of the TEME from conventional ECI is that the nutation of the Earth's obliquity (the angle between the equatorial plane and the ecliptic) and the precession of the vernal equinox are not calculated. Therefore, this frame is actually a quasi-inertial one. The precession and nutation motions are shown in Figure 2.2 where Luni-solar effects are larger than the planetary effects.
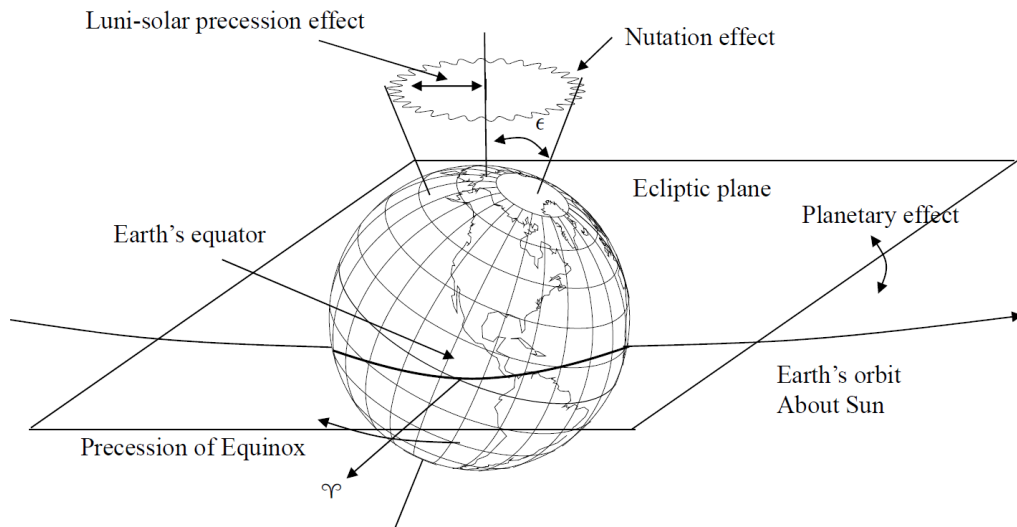
Figure 2.2. Representation of precession and nutation effects on the spin axis due to perturbation forces on the Earth. (Vallado, 2013)

2.1.1.2   Earth Centered Earth Fixed (ECEF or ECF)

A body fixed frame is tied to the central body where the orbital motion is considered around. In this thesis, Earth is considered as the central body and therefore the axes of the coordinate system are rotating and osculating (with precession and nutation) with Earth for a body fixed frame. The assumptions of the Earth Centered Earth Fixed (or Earth Centered Fixed) frame are defined as follows:

- Coordinate System: Cartesian
- Origin: Center of mass of the Earth
- Orientation of Axes: X axis points along the osculating vector from center of Earth toward the equator along the Prime Meridian (Greenwich, 0° Longitude), Z axis points along osculating spin-axis vector and Y axis completes right-handed coordinate system.
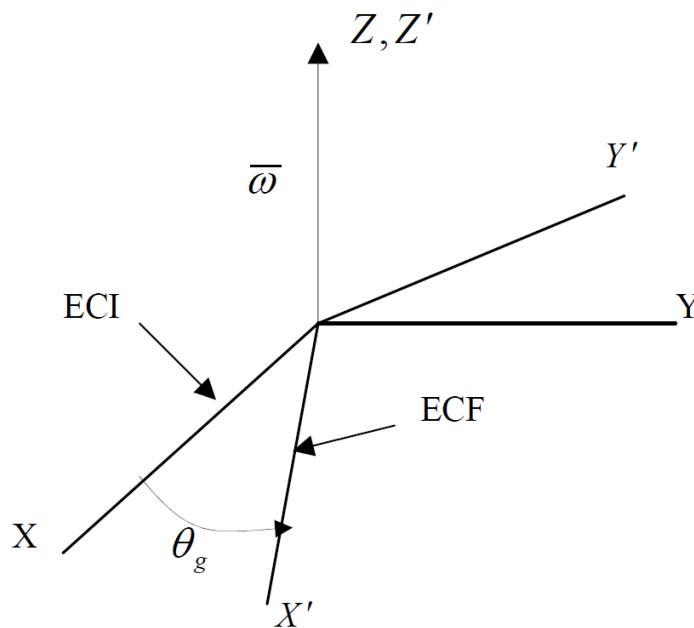
Figure 2.3. Simplified Representation of Earth Centered Earth Fixed Frame with respect to Earth Centered Inertial Frame

Based on simplified representation given in Figure 2.3, the transformation matrix $\mathcal{R}_3$ from ECI to ECEF can be written as in Eq. (1)

$$\mathcal{R}_3(\Theta_g) = \begin{bmatrix} \cos(\Theta_g) & \sin(\Theta_g) & 0 \\ -\sin(\Theta_g) & \cos(\Theta_g) & 0 \\ 0 & 0 & 1 \end{bmatrix} \tag{1}$$

where Θ_g is the Greenwich true sidereal angle which is calculated using Eq. (2).

$$\Theta_g = \Theta_{g,0} + \omega_\oplus(t - t_0) \tag{2}$$

Here $\Theta_{g,0}$ is the Greenwich hour angle at the epoch t_0 and $\omega_\oplus$ is the angular velocity of the Earth's rotation around its spin axis ($\omega_\oplus = 7.29212 \times 10^{-5}$ rad/s). However, in reality there is also other transformations needed to compensate the motion of the Earth's poles as well as the precession and nutation of the spin axis. Therefore, the final transformation matrix to transform an ECI vector to an ECEF vector, $\vec{r}_{ECEF} = \mathcal{R}_{ECEF}^{ECI}(t, \Theta_g) \vec{r}_{ECI}$, is written in Eq. (3).

$$\mathcal{R}_{ECEF}^{ECI}(t, \Theta_g) = \mathcal{W}(t)\, \mathcal{R}_3(\Theta_g)\, \mathcal{N}(t)\, \mathcal{P}(t) \tag{3}$$

Here $\mathcal{P}(t)$ represents the precession, $\mathcal{N}(t)$ represents the nutation and $\mathcal{W}(t)$ represents the polar motion compensations. The details of the calculation of such compensation matrices are provided in Chapter 3 of (Vallado, 2013). When transforming from TEME to ECEF, $\mathcal{P}(t)$ and $\mathcal{N}(t)$ are not calculated and mean sidereal angle is used instead of Greenwich true sidereal angle.

2.1.1.3 Spacecraft Centered Local Frames

Local frames are useful when the state representation is expressed with respect to a reference observer. In this thesis, the reference observer is the reference spacecraft as the main concern is the representation of relative motion. In this manner, this frame is a vehicle carried and rotating one defined as follows:

- Coordinate System: Cartesian
- Origin: Reference spacecraft

- Orientation of Axes: X axis points along the direction of the spacecraft position vector, Z axis points along the direction of the orbit normal vector and Y axis completes right-handed coordinate system.

Here, X, Y, Z axes can be named as Radial, Transversal and Normal (RTN) respectively and can be represented in Figure 2.4.
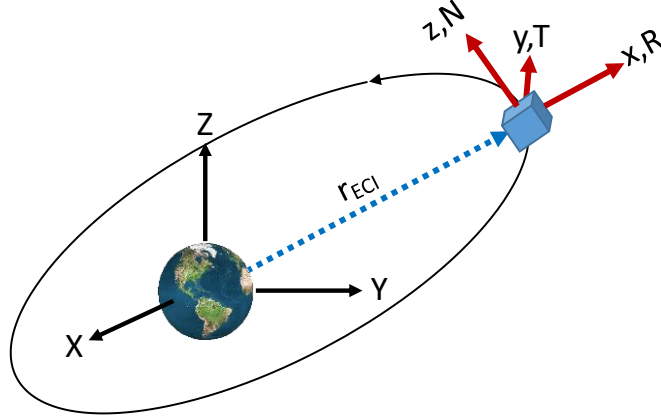
Figure 2.4. RTN frame centered in the reference spacecraft

The transformation from an ECI vector to RTN can be dest

$$\vec{r} = \vec{r}_{ECI} \tag{4}$$

$$\vec{R} = \frac{\vec{r}}{|\vec{r}|} \tag{5}$$

$$\vec{N} = \frac{\vec{r} \times \vec{v}}{|\vec{r} \times \vec{v}|} \tag{6}$$

$$\vec{T} = \vec{N} \times \vec{R} \tag{7}$$

$$\vec{r}_{RTN} = [R \vdots T \vdots N]^T \, \vec{r}_{ECI} = \beta_{RTN}^{ECI} \, \vec{r}_{ECI} \tag{8}$$

$$\vec{r}_{RTN} = \begin{bmatrix} R_X & R_Y & R_Z \\ T_X & T_Y & T_Z \\ N_X & N_Y & N_Z \end{bmatrix} \vec{r}_{ECI} \tag{9}$$

$$\vec{r}_{ECI} = \beta_{RTN}^{ECI}{}^T \, \vec{r}_{RTN} \tag{10}$$

As it can be deduced from above formulation, the T direction is aligned with the velocity vector and can be called Along-Track for a circular reference orbit.

This spacecraft centered local frame can be also referred as Local Vertical Local Horizontal where the orientation of axes is changed such that Z axis is oriented in the direction of the center of Earth (Local Vertical), Y axis is along the negative direction to the orbit normal and X axis completes right-handed coordinate system.

2.1.2   Keplerian Orbital Elements

First of all, an orbit in two-dimensional space is represented by an ellipse which is shown in the Figure 2.5.
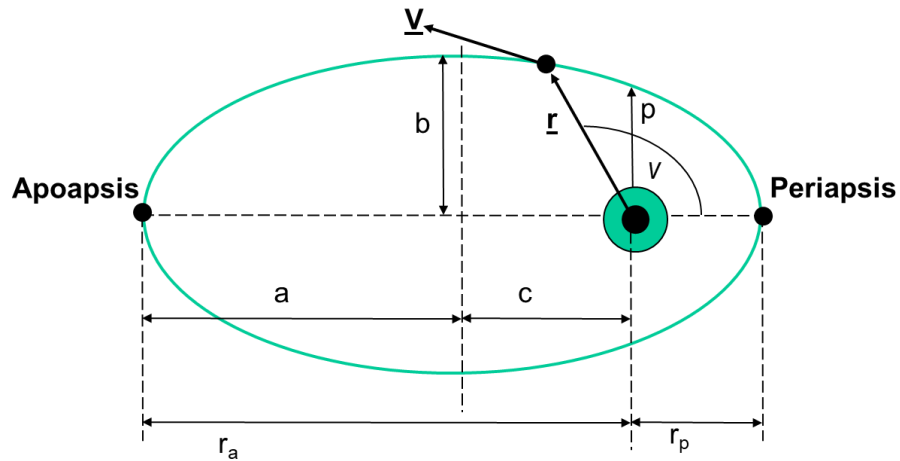
Figure 2.5. Two-dimensional orbital elements with respect to inertial frame

The ellipse describes the shape and size of an orbit where semimajor axis, a, is a measure of the size and eccentricity, e, describes ellipticity or circularity of the orbit. Here, $e = 0$ defines a perfectly circular orbit and, $0 < e < 1$ is an elliptic orbit. In addition, while $e = 1$ corresponds to parabolic orbit, $1 < e$ corresponds to hyperbolic one and both are not closed orbits. The governing equations for two-dimensional orbits are provided as follows:

$$a = (r_a + r_p)/2 \tag{11}$$

$$e = (r_a - r_p)/(r_a + r_p) \tag{12}$$

$$\varepsilon = \frac{v^2}{2} - \frac{\mu}{r} = -\frac{\mu}{2a} \tag{13}$$

$$T = 2\pi \sqrt{\frac{a^3}{\mu}} \tag{14}$$

$$n = \sqrt{\frac{\mu}{a^3}} \tag{15}$$

Where r_a is the apoapsis radius which is the furthest point from the focal point, r_p is the periapsis radius which is the closest point from the focal point, ε is the orbital energy, T is the orbital period and n is the mean motion and μ is the gravitational constant. The last parameter for two-dimensional, or planar, representation of the orbit is the true anomaly, v, which describes the position of the spacecraft. Finally, the position, r, can be found using Eq. (16).

$$r = \frac{p}{1 + e \cos v} = \frac{a(1 - e^2)}{1 + e \cos v} \tag{16}$$

For representing orbits in three-dimensional space, the orientation parameters of the orbital plane with respect to inertial frame are also needed. With these orientation parameters, the full orbital elements are shown in the Figure 2.6.
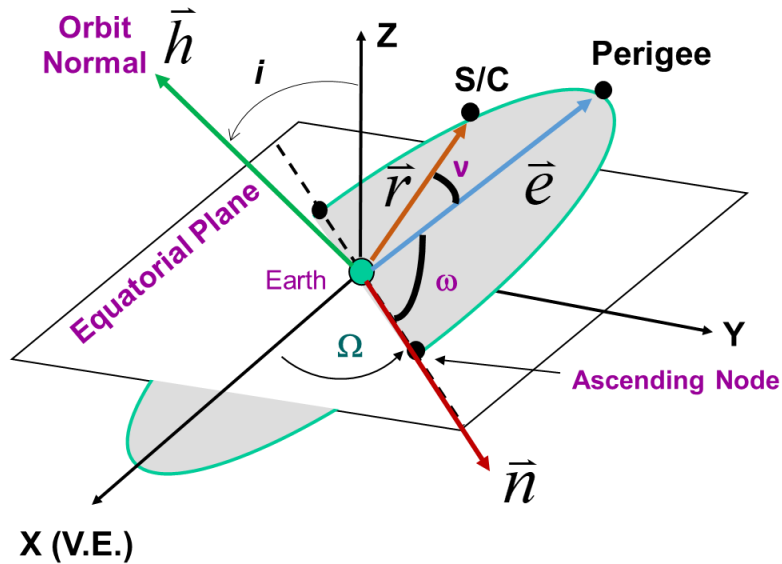
Figure 2.6. Three-dimensional orbital elements with respect to inertial frame

Here, several vectors are defined which are eccentricity vector, $\vec{e}$, angular momentum vector, $\vec{h} = \vec{r} \times \vec{v}$, and node vector, $\vec{n} = \vec{K} \times \vec{h}$. The eccentricity vector points toward the periapsis and is calculated using the relation given in Eq. (17)

$$\vec{e} = \frac{\vec{v} \times \vec{h}}{\mu} - \frac{\vec{r}}{r} \qquad (17)$$

where $|\vec{e}| = e$.

Here, the node vector is the cross product of Z direction of the ECI and angular momentum vector and it points toward the intersection point of the orbital plane and the equatorial, or X-Y, plane. This intersection point is also called the ascending node.

Using these vectors, the three-dimensional orientation of an orbit can be described. Firstly, the angle between the Z direction and the $\vec{h}$, or orbit normal, is called the inclination. Inclination angle, i, measures the tilt of the orbital plane with respect to equatorial plane. The angle from the X direction to the ascending node is called the Right Ascension of the Ascending Node (RAAN), Ω. Together with i, it defines the orientation of orbital plane in three-dimensional space. Finally, the angle between the node and eccentricity vectors is called the Argument of Perigee, ω, which describes the orientation of the orbit within the orbital plane. With these six parameters which are so called Keplerian elements an orbit can be defined in three-dimension with respect to inertial frame.

In addition to Keplerian elements, there are a few more parameters that can be useful for orbit design and analysis. Firstly, the mean anomaly, M, describes the angle that the spacecraft travels from the perigee with the rate of mean motion, $M = n(t - t_p)$ where t_p is the time at perigee passage. This parameter corresponds to true anomaly for circular orbits and can be used as a measure of time rather than an angular measure of the spacecraft's location. Secondly, it becomes difficult to define the argument of perigee for near circular orbits and therefore it is useful to introduce another parameter called the argument of latitude, $u = \omega + v$. Finally, Local Time of the Ascending Node (LTAN) is the local time the spacecraft crosses the node on

its ascending pass, when travelling from the Southern Hemisphere to the Northern Hemisphere. Usually, Earth Observation missions utilize the so-called Sun Synchronous orbit (SSO) where the angle between the orbital plane and Sun is fixed (with the use of perturbation effects of Earth's oblateness) and therefore the LTAN becomes ideally constant.

2.1.2.1   Transformation of Keplerian Elements to Cartesian State Vector

The Keplerian elements can be calculated for a given cartesian state vector, where we have $\vec{r}$ and $\vec{v}$, using the relations provided previously. However, it is also necessary to calculate the state vectors for a given orbital elements. For this, it is necessary to introduce a local frame called PQW which is shown in Figure 2.7
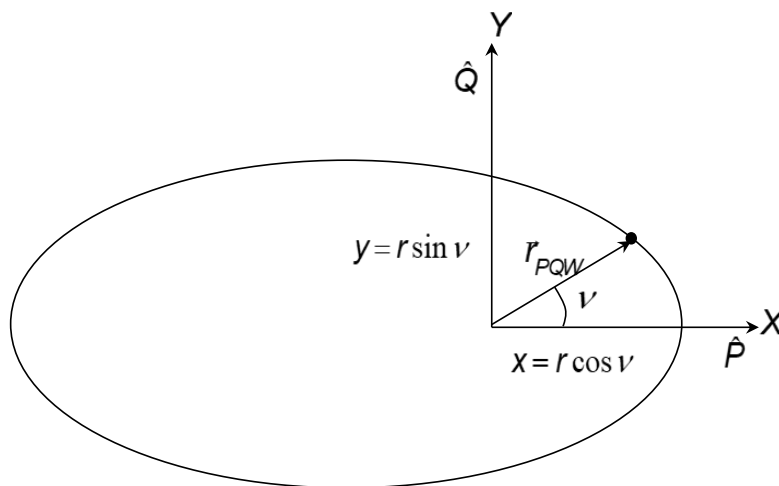
Figure 2.7. Representation of PQW frame

The PQW frame is defined as follows:

- Coordinate System: Cartesian
- Origin: Focal point of the ellipse
- Orientation of Axes: X axis points toward the apoapsis, Z axis points along the direction of the orbit normal vector and Y axis completes right-handed coordinate system.

The position vector r_{PQW} can be calculated with Eq. (18)

$$\vec{r}_{PQW} = r \cos v \ \vec{P} + r \sin v \ \vec{Q} = \begin{bmatrix} \dfrac{p \cos v}{1 + e \cos v} \\ \dfrac{p \sin v}{1 + e \cos v} \\ 0 \end{bmatrix} \tag{18}$$

Likewise, velocity vector v_{PQW} can be calculated with Eq. (19)

$$\vec{v}_{PQW} = \begin{bmatrix} \dot{r} \cos v \ - r\dot{v} \sin v \\ \dot{r} \sin v \ + r\dot{v} \cos v \\ 0 \end{bmatrix} = \begin{bmatrix} -\sqrt{\dfrac{\mu}{p}} \sin v \\ \sqrt{\dfrac{\mu}{p}} \ (e + \cos v) \\ 0 \end{bmatrix} \tag{19}$$

Finally, PQW vectors, which can be position or velocity, can be transformed to ECI coordinates using the transformation matrix given in Eq. (20)

$$\vec{r}_{ECI} \ (or \ \vec{v}_{ECI}) = \mathcal{R}_3(-\Omega) \ \mathcal{R}_1(-i) \ \mathcal{R}_3(-\omega) \ \vec{r}_{PQW} \ (or \ \vec{v}_{PQW}) \tag{20}$$

where $\mathcal{R}_1$ is a rotation matrix around X and $\mathcal{R}_3$ is a rotation matrix around Z.

2.1.3 Orbital Perturbations

The Keplerian orbital elements except true anomaly are constant where only the primary body and the orbiting spacecraft exist in the universe as point masses. This is also called two-body dynamics and defines the ideal orbital motion. The additional assumptions governing two-body dynamics are as follows:

- The primary body which is the source of main gravitational attraction is spherical and the mass distribution is uniform
- Only the gravitational forces act on the satellite

19

However, neither the primary body is spherical and the mass distribution is uniform nor only gravitational forces that act on the motion of the spacecraft. For instance, non-gravitational forces induced by atmospheric drag and radiation pressure may play a significant role for calculating highly accurate orbits. In addition, there are other bodies such as Moon and Sun which induce perturbative forces. In the following subchapters, these perturbative forces will be introduced. Detailed techniques for modeling of the orbital perturbations can be found in (Vallado, 2013) and (Montenbruck & Gill, Satellite Orbits: Models, Methods, and Applications, 2011) and the magnitudes of the major perturbation effects are shown in Figure 2.8.
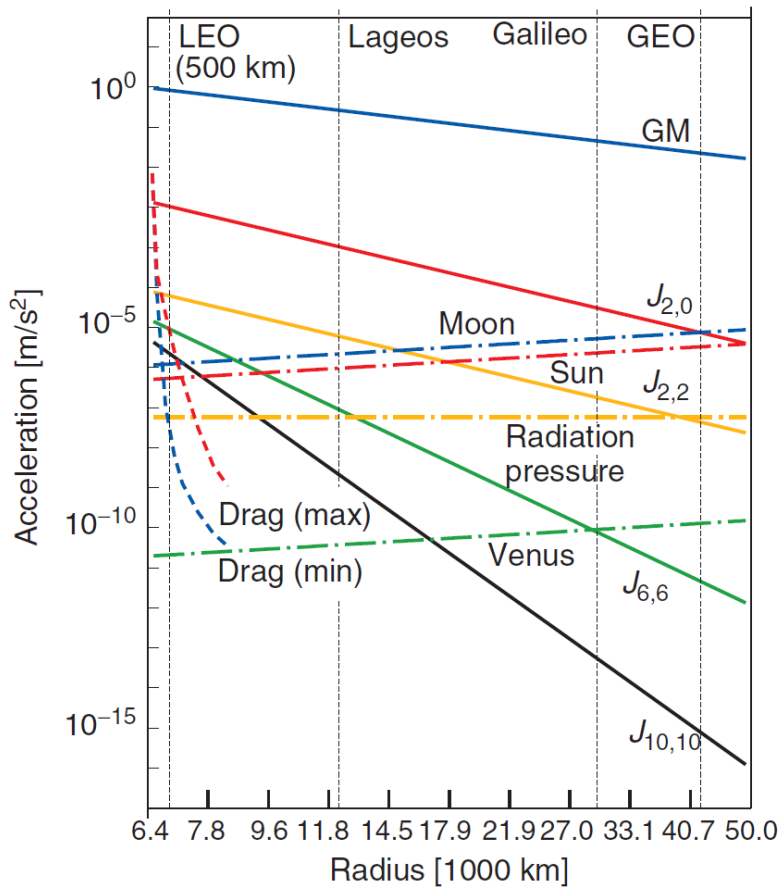
Figure 2.8. Comparison of the perturbing accelerations affecting satellites at various altitudes. Indicated are the effects of Earth's gravitation (central term GM and harmonic term $J_{n,n}$), the perturbation from point masses (Moon, Sun, Venus) as well as the influence of radiation pressure and drag. (Montenbruck, Orbital Mechanics, 2009)

20

By investigating this figure, it can be deduced that the relative effect of perturbations are highly dependent on orbital altitude. For instance, the major forces appear to be the central term of the Earth's gravitation (GM), J_2 term which will be introduced later and the luni-solar perturbations (due to Sun and Moon point masses). In addition, the atmospheric drag is effective for Low Earth Orbit (LEO).

2.1.3.1   Earth's Gravity

The Earth's radius at the poles is about 20 km smaller than at the equator due to its rotation. This oblateness has significant effects on the orbital motion. The non-spherical Earth and its non-homogeneous mass distribution can be taken into account with a generalized formulation of Earth's gravity. For this, an expansion of the gravitational potential in terms of spherical harmonics can be employed with respect to geocentric latitude, φ, and longitude, λ, at a distance r from the Earth's center. This can also be interpreted as adding or subtracting 'bands' of mass onto a perfectly spherical central body (Imre, 2006). The 'latitudinal bands' are called zonal harmonics and are symmetrical about the polar axis. Tesseral harmonics can be visualized as 'tiles' on the sphere. The 'longitudinal bands' are called sectorial harmonics. Zonal, tesseral and sectoral harmonics are illustrated in Figure 2.9.
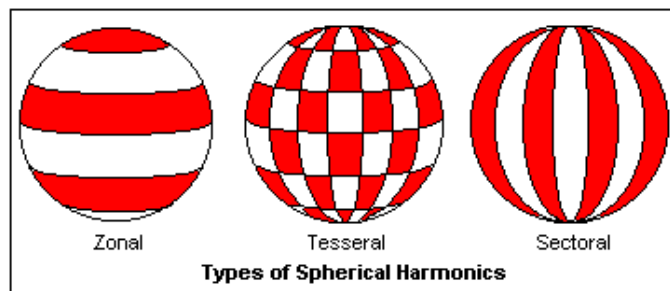
Figure 2.9. Zonal, tesseral and sectorial harmonics

The potential function describing the Earth's non-uniform gravity is provided by (Montenbruck & Gill, Satellite Orbits: Models, Methods, and Applications, 2011) and summarized by Eq. (21)

$$U = \frac{\mu}{r} \sum_{n=0}^{\infty} \sum_{m=0}^{n} \left(\frac{R_\oplus}{r}\right)^n P_{nm} \sin(\varphi) \left[C_{nm} \cos(m\lambda) + S_{nm} \sin(m\lambda)\right] \qquad (21)$$

Here, $R_\oplus$ is the Earth's equatorial radius and P_{nm} is for the associated Legendre polynomial of degree n and order m. The harmonic coefficients C_{nm} and S_{nm} of the gravitational field are determined by observations. For a given potential, U, the corresponding acceleration can be calculated from the gradient given in Eq. (22)

$$\ddot{r}_G = \nabla U = \left(\frac{\partial U}{\partial x}; \frac{\partial U}{\partial y}; \frac{\partial U}{\partial z}\right) \qquad (22)$$

For the main term $C_{0,0} = 1$, Newton's law of universal gravitation describing the attraction of a spherical body with isotropic mass distribution is obtained.

In addition, Earth's oblateness' effect is calculated considering the zonal coefficient $C_{2,0} = J_2 = -1.082 \cdot 10^{-3}$ leading to an acceleration given in Eq. (23)

$$\ddot{r}_{J2} = \begin{bmatrix} \ddot{x} \\ \ddot{y} \\ \ddot{z} \end{bmatrix} = -\frac{3}{2} J_2 \frac{R_\oplus{}^2}{r^5} \begin{bmatrix} x - 5x\dfrac{z^2}{r^2} \\ y - 5y\dfrac{z^2}{r^2} \\ 3z - 5\dfrac{z^3}{r^2} \end{bmatrix} \qquad (23)$$

This results in a net torque that rotates the orbital plane which is described by equations (24) and (25)

$$\Delta\dot{\Omega} = -\frac{3}{2} J_2 n \frac{R_\oplus{}^2}{a^2(1-e^2)^2} \cos(i) \qquad (24)$$

$$\Delta\dot{\omega} = \frac{3}{4} J_2 n \frac{R_\oplus{}^2}{a^2(1-e^2)^2} [4 - 5\sin^2(i)] \qquad (25)$$

By carefully selecting a, e and i, the rate $\Delta\dot{\Omega}$ can be equated to the apparent rotation rate of the Sun, i.e. 2π / $365\ days$, which results in the so-called Sun Synchronous Orbit as explained previously.

The perturbations caused by the Earth's gravity are computed in the ECEF and are transformed to ECI when integrated for orbit propagation.

2.1.3.2   Third Bodies

In addition to Earth, there are other bodies, such as Sun and Moon, that exert an acceleration on spacecraft which is caused by the attraction between two masses. Since these forces also effect the Earth's center of mass, only the difference between two acceleration functions becomes effective. This can be described by Eq. (26).

$$\ddot{r}_{3^{rd}\ Body} = \mu_S \frac{r_s - r}{|r_s - r|^3} - \mu_S \frac{r_s}{|r_s|^3} \tag{26}$$

Here, μ_S is the gravitational constant and r_S is the geocentric position of the attracting body. In this equation, the perturbing body is assumed to be a point mass as the distances are considerably large.

2.1.3.3   Solar Radiation Pressure

Apart from the gravitational perturbations, there is a non-gravitational force caused by the radiation pressure of the Sun. As the photons with energy E are absorbed on spacecraft surface an impulse is transferred with a magnitude $p = E/c$. From a mean distance of 1 AU (~149.6 Million km), the Solar flux, Φ, has an average value of 1371 W/m^2 and this pressure becomes $P_0 = \frac{\Phi}{c} = 4.57 \cdot 10^{-6} N/m^2$.

If the photons are not absorbed and completely reflected, the transferred impulse becomes twice as high. In this manner, the total perturbing acceleration resulting from Solar radiation pressure is described by Eq. (27).

$$\ddot{r}_{SRP} = -(1 + \varepsilon_R)\frac{A}{m} \cdot P_0 \, L \left(\frac{1AU}{r_{sun}}\right)^2 \cdot \frac{r_{sun}}{|r_{sun}|} \tag{27}$$

Where A is the Sun-facing cross-sectional area, m is the spacecraft mass and ε_R is the reflectivity which describes the relation between reflected and incidental sunlight and L is the illumination ratio. The term $(1 + \varepsilon_R)$ is referred as radiation pressure coefficient and can be written as $C_R = (1 + \varepsilon_R)$. As it can be deduced, the acceleration always acts in opposite direction of the spacecraft to Sun vector and it depends on the reflectivity and effective area of the surface. Finally, it is also important to consider how much the spacecraft is exposed to Solar light or namely the illumination ratio. For this a dual cone shadow model by (Ortiz Longo & Rickman, 1995) is utilized with light time delay compensation. It is umbra when $L = 0$, penumbra when $L < 1$ and total sunlight when $L = 1$.
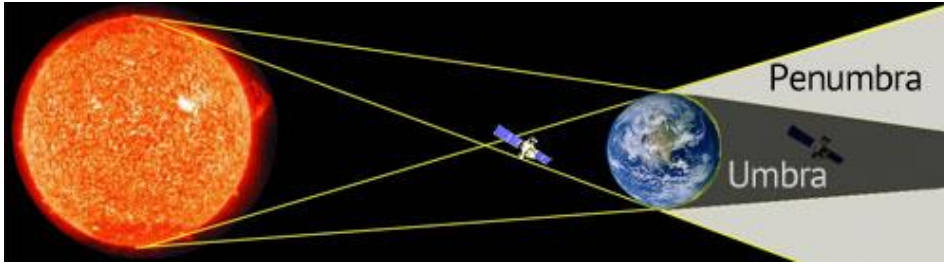
Figure 2.10. Representation of dual cone shadow model with penumbra and umbra

2.1.3.4   Atmospheric Drag

Another major non-gravitational force that perturbs an orbit with low altitudes is the atmospheric drag. The atmosphere is very thin at higher altitudes however it still causes energy losses and altitude decay. The acceleration caused by the atmospheric drag can be described by Eq. (28)

$$\ddot{r}_{Drag} = -\frac{1}{2}\rho C_D \frac{A}{m} \cdot v_{rel}^2 \frac{v_{rel}}{|v_{rel}|} \tag{28}$$

Here, ρ is the atmospheric density, C_D is the drag coefficient which represent the individual aerodynamic characteristic of a particular body, A is the cross-sectional area, m is the spacecraft mass and v_{rel} is the relative velocity with respect to atmosphere.

While calculating perturbations due to drag, determination of atmospheric density and drag coefficient plays an important role. Drag coefficient can be calculated through complex calculations that take into account the conditions of the upper atmosphere however it is often estimated or calibrated within orbit determination operations. For high fidelity drag calculations, an atmospheric model which incorporates chemical composition of atmosphere as well as solar and geomagnetic activity should be used (NOAA SWPC, 2022). Here, NRLMSISE-00 model is utilized (Picone, Hedin, & Drob, 2002) in which chemical composition of atmosphere, *F10.7* cm radio emissions (NOAA SWPC, 2022) as an indicator of solar activity and *Ap* (NOAA NESDIS, 2022) as an indicator of Geomagnetic magnetic activity are incorporated.

2.1.4 Propagation of Orbits

Orbit propagation or prediction mainly answers three questions:

- Where was the spacecraft?
- Where is it now?
- Where is it going to be?

In order to answer these questions with high accuracy and precision, proper force models as described previously should be incorporated in a proper mathematical integration. This can be achieved through analytical models or numerical methods and the techniques used in this thesis are explained in the following subchapters.

2.1.4.1   Analytical Orbit Models

With analytical models, the orbital path can be described by orbital elements as a function of time. In this manner, the spacecraft's position can be obtained in the past, present or future epochs without intermediate steps. For instance, the Keplerian orbit model (or two body) which is introduced previously describes the spacecraft motion in a central force field.

When the perturbations are applied, the temporal effects on orbital elements can be calculated through Gaussian variational equations which are introduced as follows:

$$\frac{da}{dt} = \frac{2}{n\sqrt{1-e^2}} \left[e \sin v \cdot a_R + \frac{p}{r} \cdot a_T \right] \tag{29}$$

$$\frac{de}{dt} = \frac{\sqrt{1-e^2}}{n\,a} \left[\sin v \cdot a_R + (\cos E + \cos v) \cdot a_T \right] \tag{30}$$

$$\frac{di}{dt} = \frac{1}{n\,a^2\,\sqrt{1-e^2}} \, r \cos u \cdot a_N \tag{31}$$

$$\frac{d\Omega}{dt} = \frac{1}{n\,a^2\,\sqrt{1-e^2}} \frac{r \sin u}{\sin i} \cdot a_N \tag{32}$$

$$\frac{d\omega}{dt} = \frac{\sqrt{1-e^2}}{n\,a\,e} \left[-\cos v \cdot a_R + \left(1 + \frac{r}{p}\right) \sin v \cdot a_T \right] - \cos i \cdot \frac{d\Omega}{dt} \tag{33}$$

$$\frac{d\mathrm{M}_0}{dt} = \frac{1}{n\,a^2\,e} \cdot \left[(p \cos v - 2\,e\,r) \cdot a_R - (p + r) \sin v \cdot a_T \right] \tag{34}$$

where a_R, a_T and a_N are the perturbation accelerations in RTN frame and E is called eccentric anomaly which is solved for $E - e \sin E = M$. Here, the perturbations can

be calculated along the orbit and represented as a periodic series expansion. Then, this can be integrated to achieve an analytical expression for orbital elements with respect to time. An important example of such analytical model is developed by (Kaula, 1966).

The perturbations may cause periodic and secular changes on the orbital elements over time. This is represented in the Figure 2.11.
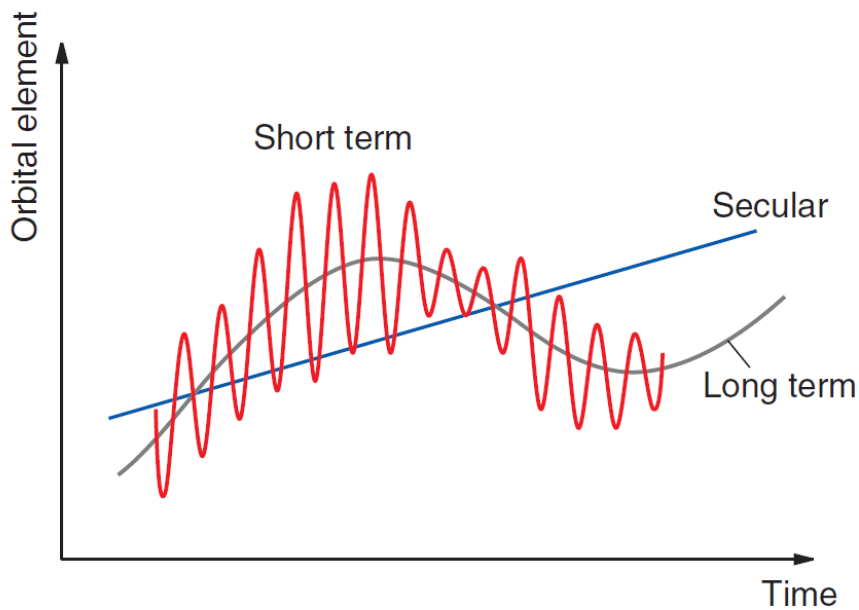
Figure 2.11. Change of orbital elements over time due to perturbations

Here, we can refer single orbit as short term and monthly and/or yearly variations as long term. The secular perturbations describe the long-term remaining changes after averaging for short or long terms.

Most widely used analytical model is the Simplified General Perturbations Model No. 4 (SGP4). The SGP4 makes use of specific "mean" orbital elements, which will be explained later, and several other parameters which are only valid for this model. These elements are represented in a two-line data format which is called Two-Line Elements (TLE). The meaning of TLE parameters is shown in Figure 2.12.

```
.........|.........|.........|.........|.........|.........|.........
1 25544U 98067A   06287.64456019  .00008182  00000-0  53355-4 0  8609
2 25544 051.6354 292.0281 0013277 096.0881 057.9543 15.76874518452008
.........|.........|.........|.........|.........|.........|.........
123456789012345678901234567890123456789012345678901234567890123456789
```

Row	Column	Description	Example	Meaning
1	1	Line number identification (= 1)	1	First line
	3–7	NORAD catalog number (Example 16609)	25554	ISS (Zarya Module)
	8	Security classification	U	Not classified
	10–17	International COSPAR satellite identification (yynnnaaa), consisting of the year (yy), launch number (nnn) and piece letter (aaa)	98067A	First catalog object of the 67th launch of the year 1998
	19–20	Epoch of the orbital element (year)	06	2006
	21–32	Epoch day and fraction of 24-hour day (UTC)	287.64456019	October 14, 15:28:10
	34–43	First time derivative of the mean anomaly (in [rev/d^2]) or ballistic coefficient B	.00008182	0.00008182
	45–52	Second time derivative of the mean anomaly (in [rev/d^3]) (Decimal between columns 45 and 46; exponent in columns 51–52)	00000-0	0.0
	54–61	Bstar/drag term B^* (in [$1/R_\oplus$]); (Decimal between columns 54 and 55; exponent in columns 60–61)	53355-4	$0.53355 \cdot 10^{-4}$
	63	Ephemeris type	0	SGP4 model
	65–68	Element number	860	860
	69	Check sum (modulo 10)	9	9
2	1	Line number identification (= 2)	2	Second line
	3–7	NORAD catalog number (example 16609)	25554	ISS (Zarya Module)
	9–16	*Inclination* (in [°])	051.6354	51.6354°
	18–25	Right ascension of ascending node (in [°])	292.0281	292.0281°
	27–33	Eccentricity with assumed leading decimal (between columns 26 and 27)	0013277	0.0013277
	35–42	Argument of the perigee (in [°])	096.0881	96.0881°
	44–51	Mean anomaly (in [°])	057.9543	057.9543°
	53–63	Mean motion (in [rev/d])	15.76874518	15.76874518°/d
	64–68	Revolution number at epoch	45200	45200
	69	Check sum (modulo 10)	8	8

Figure 2.12. Two Line Element (TLE) format and its description (Montenbruck, Orbital Mechanics, 2009)

SGP4 model is built upon gravitational perturbation model by (Brouwer, 1959) and an analytical model that describes atmospheric drag. Here, the atmospheric density, ρ, is described with respect to altitude, h, in Eq. (35).

$$\rho_{SGP4}(h) = 2.461 \cdot 10^{-8} \frac{kg}{m^3} \left(\frac{42\ km}{h - 78\ km} \right) \tag{35}$$

28

The currently used complete model is described by (Hoots, Roehrich, & Kelso, 1988) where secular and periodical perturbations are accounted for the gravitational field coefficients $J_2, J_{2,2}, J_3$ and J_4. SGP4 model is valid for the orbits with altitude below 6000 km. If the orbital period is greater than 225 min. then the model also considers the perturbations caused by Sun and Moon and the TLEs are generated accordingly. The output of SGP4 is a cartesian state vector in TEME.

The accuracy of the SGP4 is shown in Figure 2.13 for a 3-day fit for an LTAN 10:30 SSO at 680 km altitude.
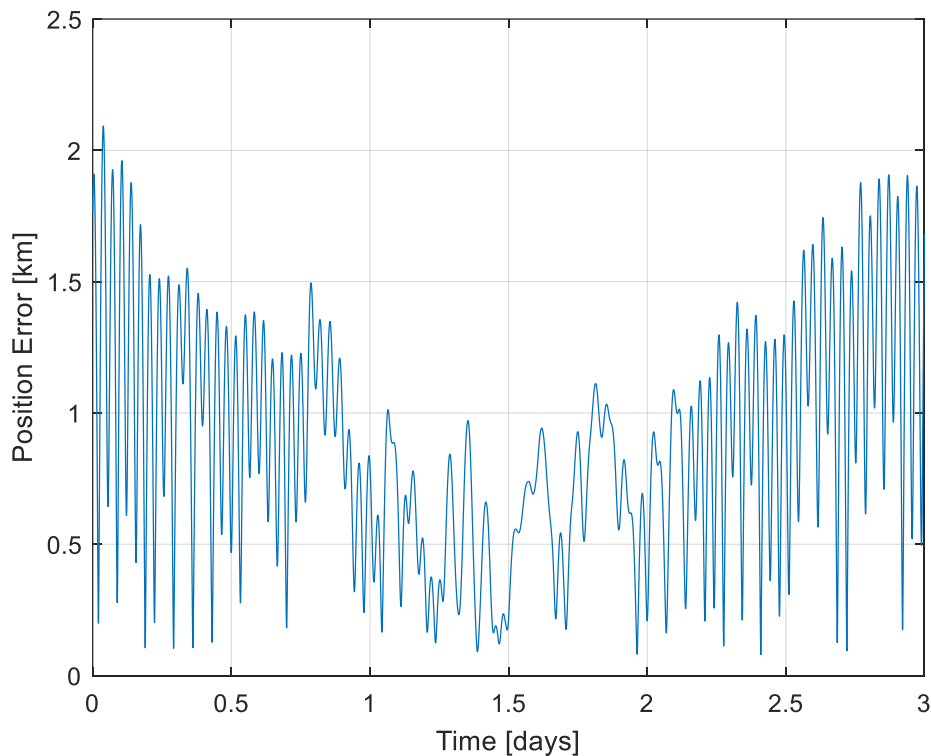
Figure 2.13. Position error of SGP4 model for a 3-day fit

As it can be seen, the errors stay within a bound between a hundred meters and 2 km fpr 3 days of propagation. The error grows in time quadratically and mainly occurs in the flight direction due to the inaccuracy of the drag calculations with poor atmospheric density prediction. If the time span is elongated to 7 days (instead of 3) then the maximum position error reaches up to 4.5 km. When the variance of

atmospheric density is relatively low, these errors decrease. Although the error of SGP4 limits calculations for a high precision absolute orbit analysis, it is still effective to analyze relative distances through differentiating TLEs of all spacecraft in a cluster. Here, common errors can be cancelled and the expected accuracy can be about 30-100 m. in radial and normal direction and better than 500 m. in transversal direction (Kirschner M., 2001). Use of TLEs for relative motion analysis is explained more in Chapter 2.2.4

2.1.4.2   Osculating and Mean Orbital Elements

Osculating orbital elements are a set of Kepler parameters that reproduce the spacecraft's exact position and velocity at a specific time instant. However, because of the orbital perturbations, it is not possible to match that exact position and velocity at another instant. Therefore, these elements can be referred as instantaneous orbital elements. On the other hand, the mean orbital elements are fit such that the obtained trajectory is relatively close to the observations of an orbiting body. A good analogy for osculating and mean elements can be provided in terms of linear regression to an arbitrary observation of a unitless parameter that is shown in Figure 2.14.
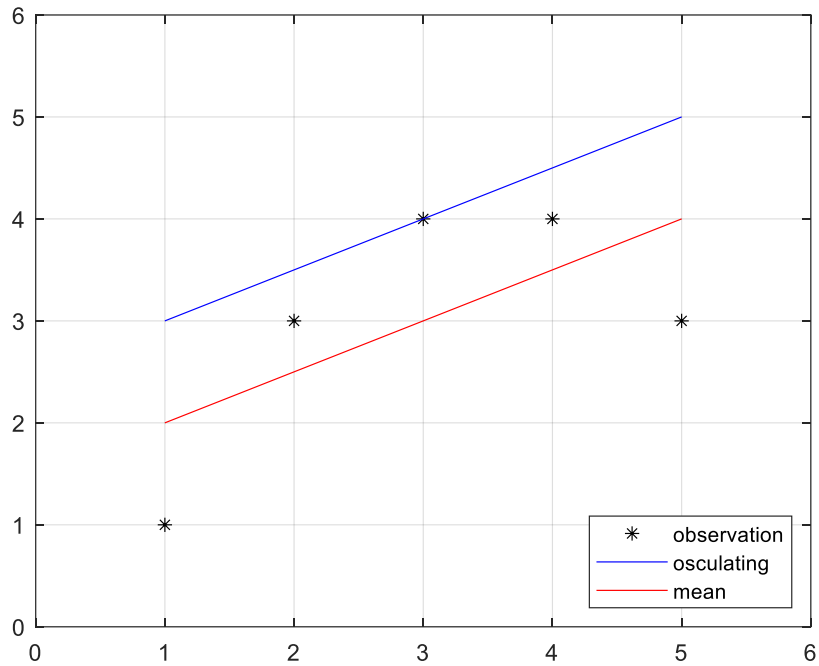
Figure 2.14. Osculating and mean elements with respect to an observation

Here, the osculating element matches exactly to a single observation however can predict another observation with a high error. On the other hand, mean element does not specifically match to an observation exactly however it follows the trend of observations and produces relatively less error for a given time interval. A sample evolution of osculating and mean orbital elements over a year provided by (Zhong & Gurfil, 2013) can be seen in Figure 2.15.
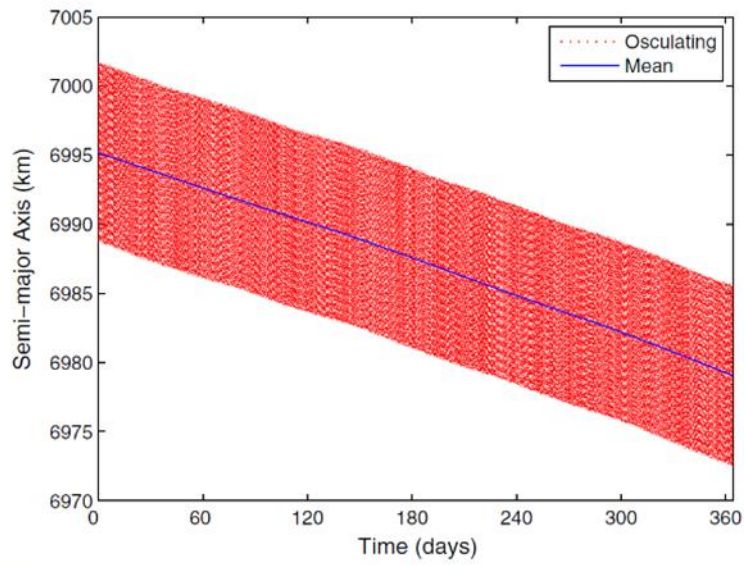
a) Semimajor axis
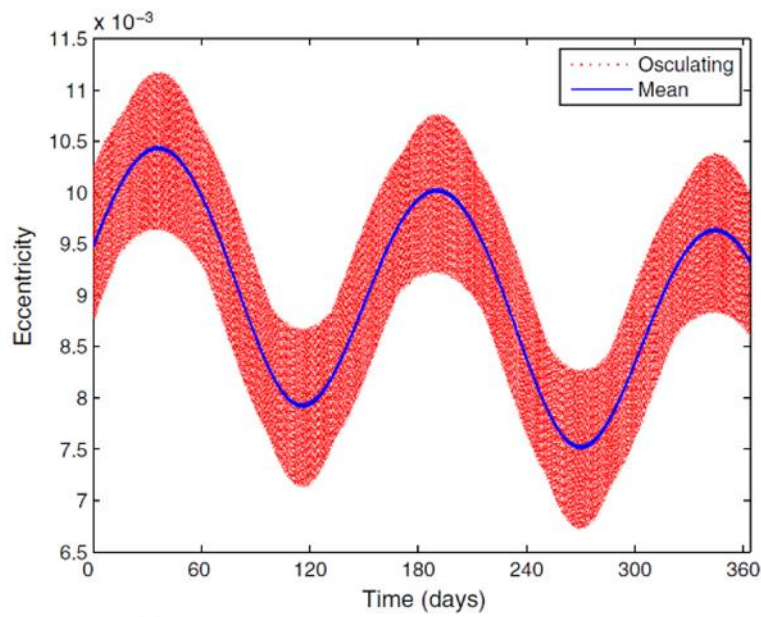
b) Eccentricity

Figure 2.15. Osculating and mean semimajor axis and eccentricity for a sample one-year simulation (Zhong & Gurfil, 2013)

As it can be seen from the figures, mean orbital elements can capture the long-term evolution while removing high frequency oscillations making it practical for planning corrections to compensate unwanted effects of orbital perturbations. For

32

example, correction for altitude decrease due to atmospheric drag can be evaluated by analyzing the mean values (blue line) for semimajor axis instead of responding to the fast variations of the osculating values (red line) which would result in unnecessary propellant consumption.

2.1.4.3 Numerical Propagation

Another way to compute the orbits of spacecraft is to numerically integrate acceleration vectors for an initial state vector. Compared to analytical methods, numerical integration provides a much higher accuracy depending on the integration method. However, a comparison between analytical and numerical methods is provided by (Gill, 2011) and shown in Table 2.1.

Table 2.1 Methods and their characterization for absolute orbit computation

Method	Type	Application	Strengths	Examples
Numerical	Numerical integration of EOM	Orbit determination	- Accuracy - Generality	- Runge - Kutta - Symplectic
Analytical	Perturbation theory	Mission planning	- Physical insight - Low computational effort	- SGP4 - Kaula

For numerical integration, the orbital motion is described by a differential equation in the form as follows:

$$x(t) = \begin{pmatrix} r(t) \\ v(t) \end{pmatrix}, \qquad \dot{x}(t) = \begin{pmatrix} v(t) \\ a(t) \end{pmatrix}, \tag{36}$$

$$\dot{r}(t) = v(t), \qquad \ddot{r}(t) = \dot{v}(t) = a(t)$$

Where r, v and a are the position, velocity and acceleration vectors respectively. One can integrate the derivatives of state vector from an initial condition to obtain position and velocity at multiple time instants until desired duration is achieved. Compared to analytical models which requires a closed-form solution of perturbation acceleration, numerical methods are less limited. Here, it is sufficient to calculate accelerations given in Eq. (37) at discrete time instants.

$$\ddot{r}(t) = a_{Gravity} + a_{Sun} + a_{Moon} + a_{Drag} + a_{SolRad} + a_{Thrust} + \cdots \qquad (37)$$

Another important point is the choice of a suitable integration method. This depends on the required accuracy, eccentricity and length of the orbital arc (or duration) to be calculated. A popular example for a single step method is the Runge-Kutta fourth-order method (RK4) with a set of equations given in Eq. (38) for a step size of h.

$$x(t+h) = x(t) + \frac{h}{6}(k_1 + 2k_2 + 2k_3 + k_4)$$

$$k_1 = f(t, x(t))$$

$$k_2 = f\left(t + \frac{h}{2}, x(t) + \frac{h}{2}k_1\right) \qquad (38)$$

$$k_3 = f\left(t + \frac{h}{2}, x(t) + \frac{h}{2}k_2\right)$$

$$k_4 = f(t + h, x(t) + hk_3)$$

Although it is relatively easy to implement Runge-Kutta methods and obtain high accuracy, it is not possible to conserve the energy which would adversely affect the accuracy in long term. This is shown Figure 2.16 where only Keplerian force field is considered to evaluate solely the numerical method.
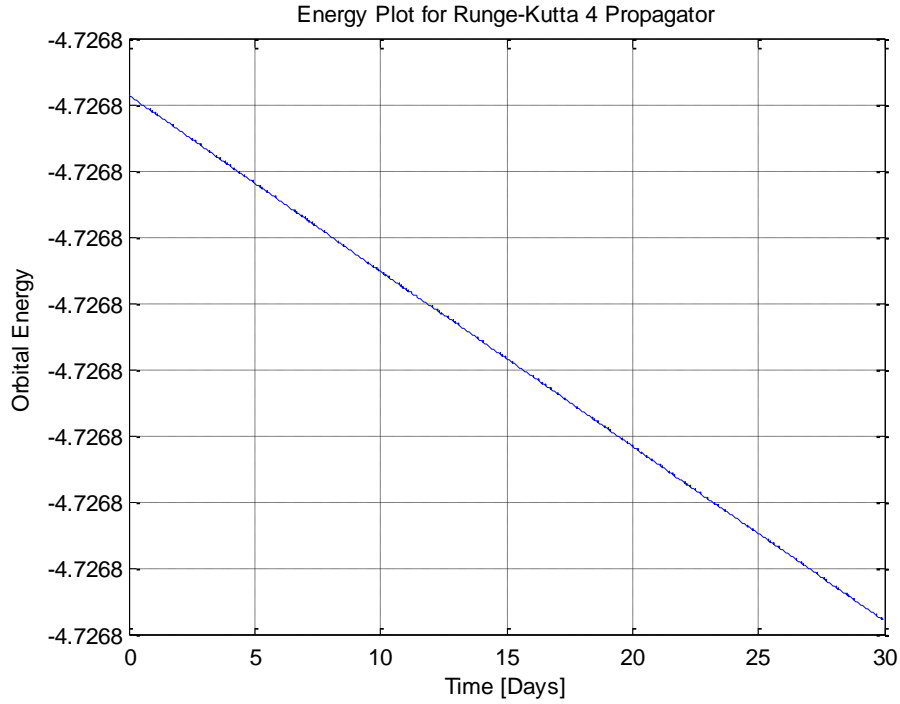
Figure 2.16. Energy plot of RK4 integrator for two body force field

To overcome energy losses, a symplectic integration methodology can be utilized (Mikkola, 1999). Symplectic methods conserves energy and momentum for higher order gravitational potential where Hamiltonian formulation is given in Eq. (39)

$$H(r,v) = K(r,v) + R(r) = \frac{1}{2}v^2 - \frac{\mu}{r} + R(r)$$

$$\dot{r} = \frac{\partial r}{\partial t} = \frac{\partial H}{\partial v}, \quad \dot{v} = \frac{\partial v}{\partial t} = -\frac{\partial H}{\partial r} \tag{39}$$

$$\dot{H} = \frac{\partial H}{\partial v}\frac{\partial v}{\partial t} + \frac{\partial H}{\partial r}\frac{\partial r}{\partial t} = \frac{\partial H}{\partial v}\left(-\frac{\partial H}{\partial r}\right) + \frac{\partial H}{\partial r}\frac{\partial H}{\partial v} = 0$$

Here splitting Hamiltonian enables us to compute Keplerian, $K(r,v)$, and higher order gravitational parts, $R(r)$, separately. In addition, we can introduce leap frog schemes described as follows:
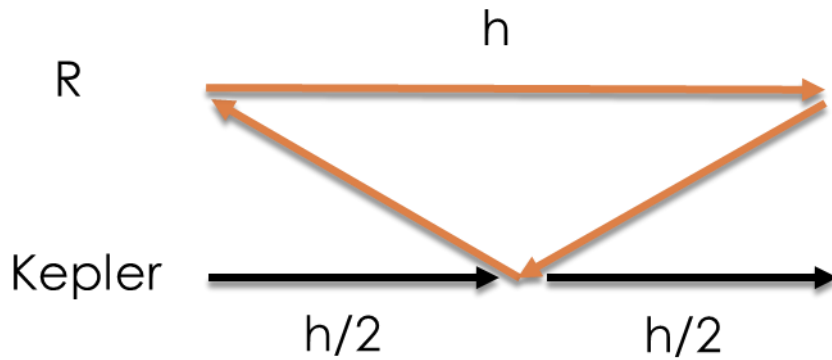
Figure 2.17. Leap frog representation

For leap frog scheme, R is independent of velocity and causes a jump in velocity with no change in position where

$$\Delta v = -h\frac{\partial R}{\partial r} \tag{40}$$

With symplectic integration, it is possible to incorporate analytical Kepler model into numerical integration and calculate Hamiltonians with different orders separately (Yoshida, 1990). Here, we can consider a composite symplectic integration scheme which is described in Figure 2.18.
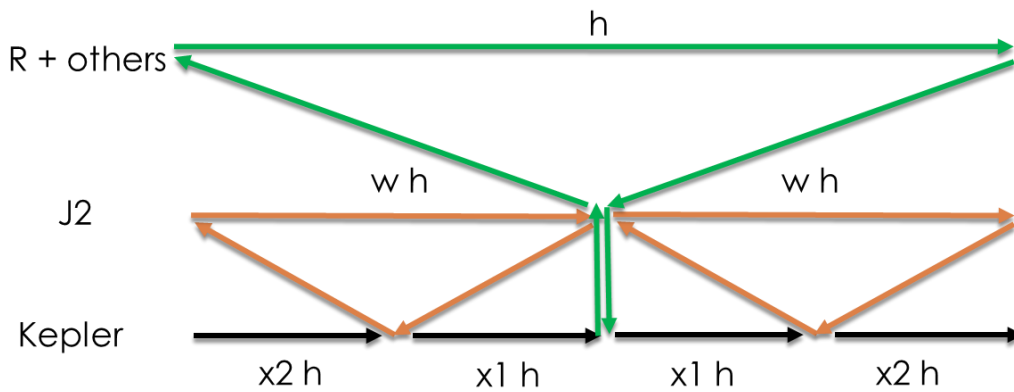
Figure 2.18. A composite symplectic integration scheme

With this integration scheme, different forces can be integrated with different time steps where $x1$, $x2$ and w are propagator specific ratios of a fixed time step h.

Considering different orders of perturbative accelerations shown in Figure 2.8, integrating different accelerations with different time steps can also reduce computational effort. Finally, the implemented integration scheme is shown in Figure 2.19.
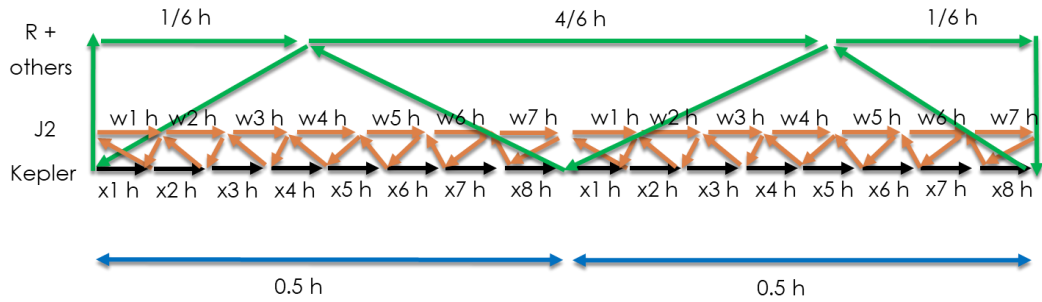
Figure 2.19. Implemented symplectic integration scheme

The energy plot for symplectic integration method for Keplerian motion is provided in Figure 2.20.
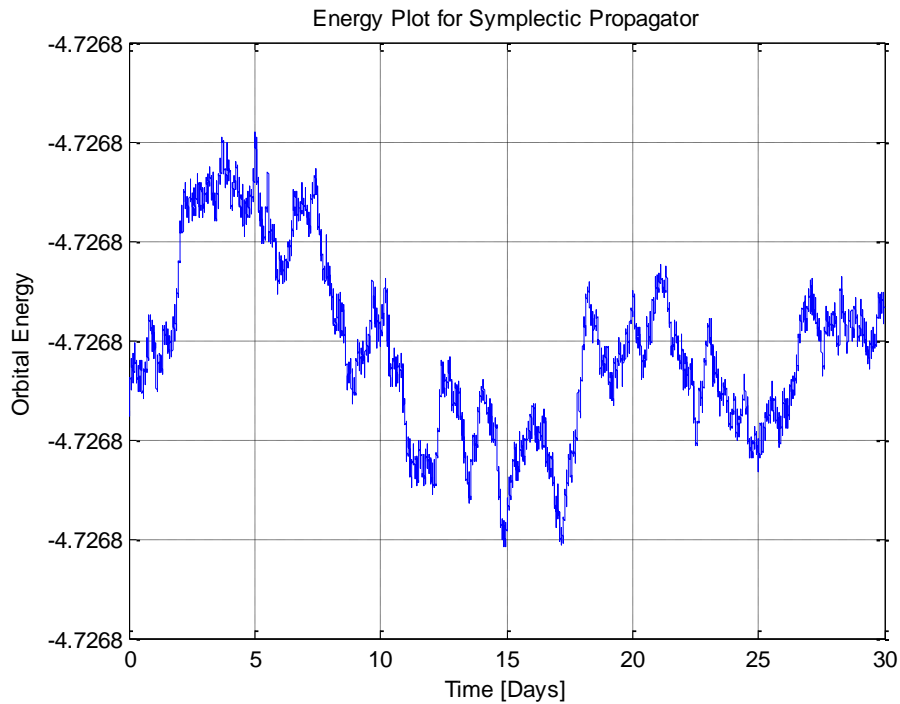
Figure 2.20. Energy plot of symplectic integrator for two body force field

As it can be seen from Figure 2.20, the energy is relatively constant when compared to RK4 integrator. Finally, the comparison of numerical integration methods for Keplerian motion is summarized in Table 2.2.

Table 2.2 Comparison of numerical methods

Method	Runge-Kutta	Symplectic
Energy Conversation	No	Yes
Different Time Steps for Different Forces	No	Yes
Analytic Model Incorporation	No	Yes
Error in Position after 30 days [m] (Compared to Analytical Solution)	10.4	10.4
Propagation Time [sec]	48	11

To demonstrate the accuracy of the developed orbit propagator, real flight data are used to propagate and compare 6 day separated reference states (initial and final) which are obtained by filtering GPS receiver outputs. The assumptions and result of state comparison is given in Table 2.3.

Table 2.3 Comparison of numerically propagated states and real flight data

Parameter	Value
Interval Between Reference States	6-12 August 2018, 5.98 days
Orbit	SSO (LTAN 10:30) at 660 km. altitude
Numerical Method	3rd Order Formulation for Symplectic Propagation with Analytical 2-Body, 6th Order J2 Integration and Leapfrog Scheme for Higher Order Terms

Force Models	Earth's Gravity with Degree: 20, Order: 20
	Luni-Solar Third Body
	Solar Radiation Pressure (Spherical Body, Conic Shadow Model)
	Atmospheric Drag (NRLMSISE-00 density model, space weather with F10.7: 70, F10.7A: 71.5, Ap: 5.4)
Difference Between Propagated and Reference States at Terminal	~430 m.

Considering that the atmospheric drag would be a major uncertainty for real life space flight in LEO, the resulting position error is within an acceptable range for validating the developed high precision orbit propagator. Instead of using space weather data and assuming a slightly different space weather activity (F10.7: 100, F10.7A: 100, Ap: 5.4) would have resulted in a position error of 1.3 km and assuming an increased activity (F10.7: 150, F10.7A: 150, Ap: 5.4) would have resulted in a position error of 9.8 km.

2.2 Representation and Propagation of Relative Orbit

For cluster flying, it is necessary to calculate and analyze relative spacecraft motion. Here, two fundamentally different approach can be applied: numerically integrated absolute orbits of spacecraft can be differenced to obtain relative trajectories or a dedicated analytical model can be used to describe the relative motion. In this manner, several representations of and modeling techniques for relative motion will be introduced in following subchapters.

2.2.1 Cartesian Representation and Hill-Clohessy-Wiltshire Equations

As described in Chapter 2.1, a high precision orbit propagator is developed based on cartesian state elements where relative state can also be represented in RTN frame as described in Chapter 2.1.1.3. Here, using the propagation of orbits of reference and other spacecraft, relative cartesian states in ECI can be simply obtained by subtracting the positions of a specific spacecraft from the reference ones as follows:

$$\Delta X_l = \begin{bmatrix} X_l - X_r \\ Y_l - Y_r \\ Z_l - Z_r \end{bmatrix} \tag{41}$$

Where l is an index for the specific spacecraft and r refers to reference. This relative position can be transformed from inertial frame to RTN or LVLH frame which is defined by the reference orbit. With this, these relative positions can be further decomposed into radial (R), along-track (T) and cross-track (N) components and the relative position vector for each spacecraft becomes $\Delta X_{l,RTN} = [\Delta R_l \quad \Delta T_l \quad \Delta N_l]$. Finally, the relative distance between any two spacecraft at a specific discrete time instant can be written as $\Delta X_{l,m,j} = [\Delta R_{l,m,j} \quad \Delta T_{l,m,j} \quad \Delta N_{l,m,j}]$ where $l \neq m$ are spacecraft indices, and j indicates a discrete time instant. In this manner, $\Delta X_{l,m,j}$ describes the relative distance between the spacecraft l and m at the time instant j.

The most common model of relative motion which utilizes the cartesian relative state representation is the Hill-Clohessy-Wiltshire (HCW) Equations. The model considers two spacecraft in an Earth-bound orbit where one is selected as reference (or chief) and the other referred as deputy. The assumptions for HCW can be summarized as follows:

- Pure Keplerian (two-body) motion
- Reference spacecraft is on a circular orbit
- Relative spacecraft separation is much smaller than the geocentric distance of the satellites

With these assumptions, the relative motion can be described by Eq. (42) (Hill, 1878), (Clohessy & Wiltshire, 1960).

$$\ddot{x} - 2n\dot{y} - 3n^2 x = 0$$
$$\ddot{y} + 2n\dot{x} = 0 \tag{42}$$
$$\ddot{z} + n^2 z = 0$$

where x, y and z are aligned with the radial, along-track and cross-track directions respectively. It can be also observed that HCW equations are coupled differential equations where out-of-plane motion (cross-track) is completely decoupled from the in-plane motion (radial and along-track).

The HCW equations can be integrated in closed form. With this, a state transition matrix (STM) can be found to calculate the relative state at time t after the initial epoch for a given initial condition $(x_0 \quad y_0 \quad z_0 \quad \dot{x}_0 \quad \dot{y}_0 \quad \dot{z}_0)$ as given in Eq. (43)

$$\begin{pmatrix} x(t) \\ y(t) \\ z(t) \\ \dot{x}(t) \\ \dot{y}(t) \\ \dot{z}(t) \end{pmatrix} = \begin{bmatrix} 1 & 0 & -\cos\tau & -\sin\tau/n & 0 & 0 \\ -\frac{3}{2}n(t-t_0) & 1 & 2\sin\tau & -2\cos\tau/n & 0 & 0 \\ 0 & 0 & 0 & 0 & \sin\tau/n & -\cos\tau/n \\ 0 & 0 & n\sin\tau & -\cos\tau & 0 & 0 \\ -\frac{3}{2}n & 0 & 2n\cos\tau & 2\sin\tau & 0 & 0 \\ 0 & 0 & 0 & 0 & \cos\tau & \sin\tau \end{bmatrix} \begin{pmatrix} 4x_0 + 2\dot{y}_0/n \\ y_0 - 2\dot{x}_0/n \\ 3x_0 + 2\dot{y}_0/n \\ -\dot{x}_0 \\ \dot{z}_0 \\ -nz_0 \end{pmatrix} \tag{43}$$

where $\tau = nt$. This solution indicates that the cross-track motion is that of a harmonic oscillator. Although most of the terms are periodic, there are secular terms in in-plane (radial and along-track) motion which correspond to the spacecraft drifting apart due to a difference in energies, hence a difference in rotation rates. The full closed form periodic solution would require $4x_0 + 2\dot{y}_0/n = y_0 - 2\dot{x}_0/n = 0$.

It is also possible to find initial conditions such that the spacecraft do not drift apart. If the spacecraft drift apart too much, the first order approximation would fail. In reality, perturbations such as drag would eventually cause such separation unless some corrective control is applied.

2.2.2   Relative Orbital Elements

While cartesian relative states can be used for evaluating relative distances, relative orbital elements, $\Delta\alpha_i = \alpha_i - \alpha_r$, are useful for relative motion design and control. In addition, relative orbital elements can provide an immediate insight in to the relative geometry which is difficult to extract when working with cartesian states.

Designing cluster flying configurations is basically equivalent to defining relative orbital elements for several spacecraft based on a reference orbit. Here, the reference orbit is specific for each type of mission and it is derived from several needs and constraints depending on the application. However, once it is fixed, relative orbits can be defined by introducing small differences to reference orbital elements as given in Eq. (44).

$$\alpha_i = \alpha_r + \Delta\alpha_i \tag{44}$$

where r indicates the reference orbit and i indicates the spacecraft number within the cluster. In this equation, relative orbital elements are defined as $\Delta\alpha = [\Delta a \quad \Delta e \quad \Delta i \quad \Delta\Omega \quad \Delta\omega \quad \Delta v]$. If the relative orbital elements are given in mean form, then these elements can be changed to mean elements. This will also provide orbital elements, or initial conditions, for each spacecraft which can be propagated through proper analytical models or numerical integrators with proper parameters and force models.

Relative mean orbital elements can be represented in both singular and quasi non-singular (qns) forms (Koenig, Guffanti, & D'Amico, 2016) as provided in Eq. (45) and Eq. (46) respectively

$$\Delta\alpha^s = \begin{bmatrix} \Delta a \\ \Delta e \\ \Delta i \\ \Delta\Omega \\ \Delta\omega \\ \Delta M \end{bmatrix} = \begin{bmatrix} a_d - a_c \\ e_d - e_c \\ i_d - i_c \\ \Omega_d - \Omega_c \\ \omega_d - \omega_c \\ M_d - M_c \end{bmatrix} \tag{45}$$

$$\Delta\alpha^{qns} = \begin{bmatrix} \Delta a \\ \Delta\lambda \\ \Delta e_x \\ \Delta e_y \\ \Delta i_x \\ \Delta i_y \end{bmatrix} = \begin{bmatrix} (a_d - a_c)/a_c \\ (M_d + \omega_d) - (M_c + \omega_c) + (\Omega_d - \Omega_c)\cos i_c \\ e_d \cos\omega_d - e_c \cos\omega_c \\ e_d \sin\omega_d - e_c \sin\omega_c \\ i_d - i_c \\ (\Omega_d - \Omega_c)\sin i_c \end{bmatrix} \quad (46)$$

where d is for deputy and c is for the chief, or reference, spacecraft orbits. The singular state is so named as it is not uniquely defined when either spacecraft is in a circular or equatorial orbit. Similarly, quasi non-singular state is not unique when the deputy is in an equatorial orbit.

2.2.3   Relative Motion State Transition Matrices with Perturbations

As it is described in Chapter 2.1.3, the perturbations play an important role for predicting orbital motion accurately. Similarly, it is also important to consider the effects of perturbations on relative motion. (Imre, 2006) discusses widely about the inclusion of perturbation effects on relative motion while comparing several geopotential terms and obtains an error of 0.3% of final separation distance after 5 days for J2 only relative motion. A similar numerical experiment is also developed to investigate the effect on a widely separated spacecraft where parameters and assumptions are summarized in Table 2.4.

Table 2.4 Experimental setup for numerically propagated relative motion with different force model configurations

Parameter	Value
Reference Orbit	SSO (LTDN 10:30) at 575 km. altitude
Force Models for Reference	Earth's Gravity with Degree: 21, Order: 21
	Luni-Solar Third Body
	Solar Radiation Pressure
	Atmospheric Drag
Force Models for Comparison	2 x 0 Earth's Gravity

Relative Orbital Elements	$\begin{bmatrix} \Delta a \\ \Delta e \\ \Delta i \\ \Delta \Omega \\ \Delta \omega \\ \Delta M \end{bmatrix} = \begin{bmatrix} 0° \\ 0 \\ 0.05° \\ 0.3° \\ 0° \\ 0.35° \end{bmatrix}$

With this configuration of reference orbit and relative orbital elements, the relative distances range from 40 km. to 90 km. In this manner, the relative distance error of J2 only model for 30 days propagation is provided in Figure 2.21.
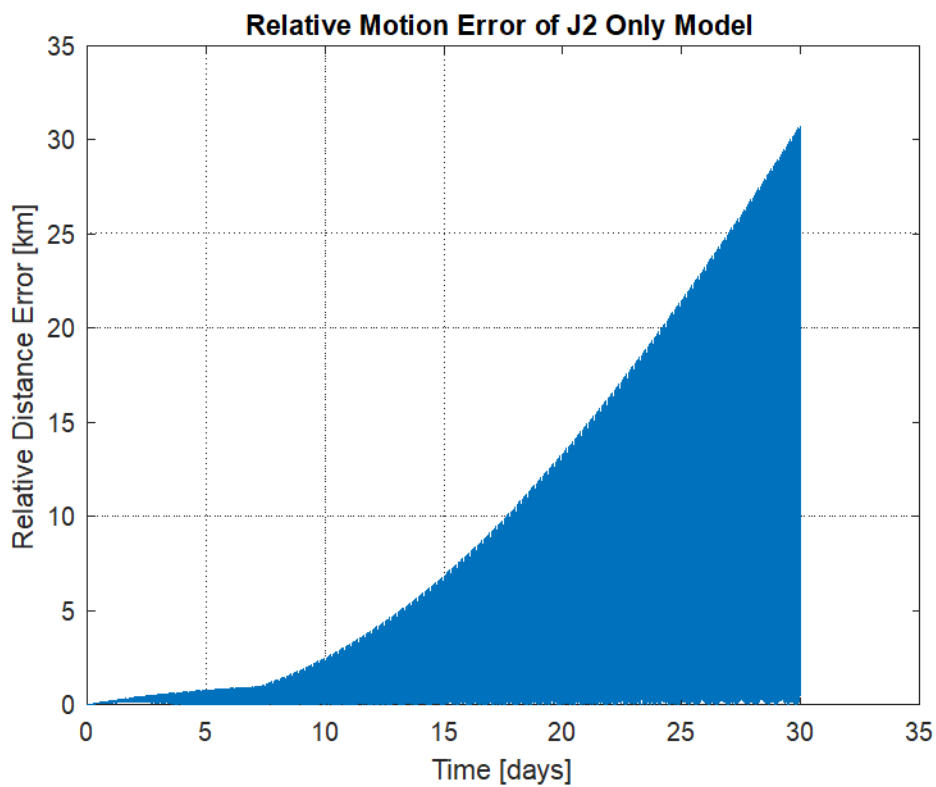
Figure 2.21. Relative motion error of J2 only model for 30 days propagation

As it can be seen from the Figure 2.21, the error grows rapidly after 1 week of propagation. In addition, the ratio of error with respect to relative distance can be seen in Figure 2.22.
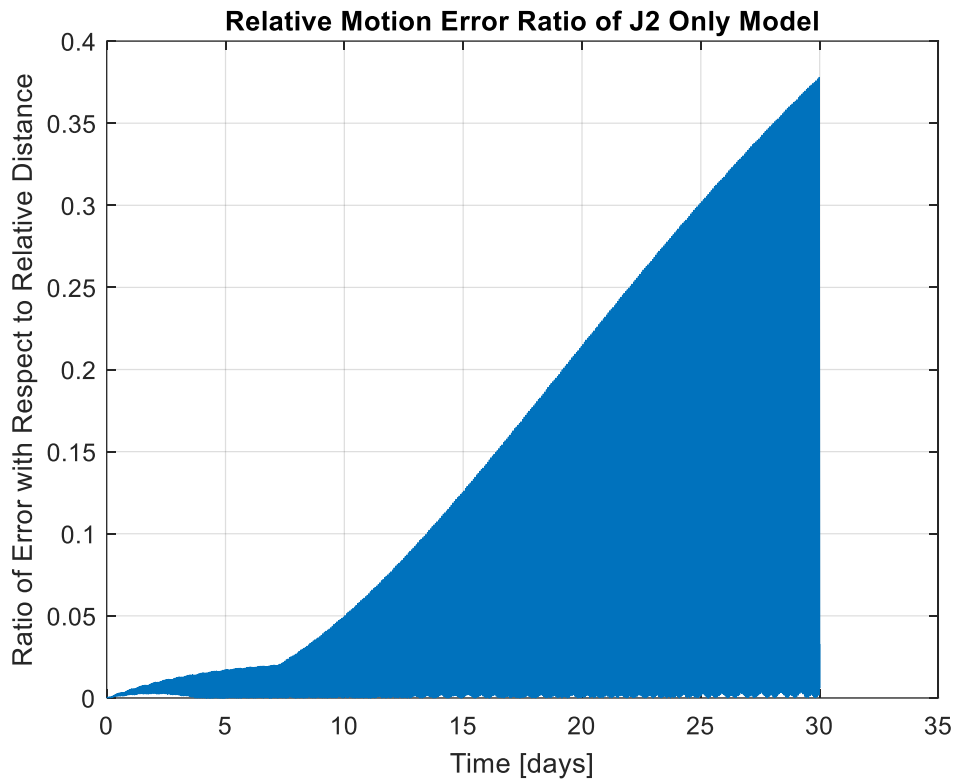
Figure 2.22. Relative motion error ratio of J2 only model for 30 days propagation

From Figure 2.22, the percentage of error with respect to relative distance can be deduced at around 2% for a 1-week propagation. As it can be deduced from above results, the incorporation of J2 in the relative dynamics models can handle relative motion of 1 week within an acceptable error margin for loosely controlled spacecraft clusters.

Fortunately, incorporation of J2 in relative motion models are widely available in the literature (Sullivan, Grimberg, & D'Amico, 2017). In this manner, the STM for relative motion of spacecraft formations incorporating J2 perturbation provided by (Koenig, Guffanti, & D'Amico, 2016) can be re-written for quasi-circular reference orbits as in Eq. (47).

$$\Phi(t_0, t_f)$$

$$= \begin{bmatrix} 1 & 0 & 0 & 0 & 0 & 0 \\ -\frac{7}{2}\kappa EP\tau - \frac{3}{2}n\tau & 1 & \kappa e_{x0}FGP\tau & \kappa e_{y0}FGP\tau & -\kappa FS\tau & 0 \\ \frac{7}{2}\kappa e_{yf}Q\tau & 0 & \cos\dot{\omega}\tau - 4\kappa e_{x0}e_{yf}GQ\tau & -\sin\dot{\omega}\tau - 4\kappa e_{y0}e_{yf}GQ\tau & 5\kappa e_{yf}S\tau & 0 \\ -\frac{7}{2}\kappa e_{xf}Q\tau & 0 & \sin\dot{\omega}\tau + 4\kappa e_{x0}e_{xf}GQ\tau & \cos\dot{\omega}\tau + 4\kappa e_{y0}e_{xf}GQ\tau & -5\kappa e_{xf}S\tau & 0 \\ 0 & 0 & 0 & 0 & 1 & 0 \\ \frac{7}{2}\kappa S\tau & 0 & -4\kappa e_{x0}GS\tau & -4\kappa e_{y0}GS\tau & 2\kappa T\tau & 1 \end{bmatrix} \quad (47)$$

where the parameters are defined as follows:

$$\tau = t_f - t_0, \qquad \eta = \sqrt{1 - e^2}, \qquad \kappa = \frac{3}{4}\frac{J_2 R_\oplus^2 \sqrt{\mu}}{a^{7/2}\eta^4},$$

$$E = 1 + \eta, \qquad F = 4 + 3\eta, \qquad G = \frac{1}{\eta^2}, \qquad P = 3\cos^2 i - 1, \qquad Q = 5\cos^2 i - 1, \quad (48)$$

$$S = \sin 2i, \qquad T = \sin^2 i, \qquad \dot{\omega} = \kappa Q, \qquad \omega_f = \omega_0 + \dot{\omega}\tau,$$

$$e_{x0} = e\cos\omega_0, \qquad e_{y0} = e\sin\omega_0, \qquad e_{xf} = e\cos\omega_f, \qquad e_{yf} = e\cos\omega_f,$$

The STM given in Eq. (47) is used with quasi-nonsingular relative orbital elements defined in Eq. (46). In addition to STM for relative orbital element states, the control input matrix is also given in Eq. (49) which is defined by (Koenig & D'Amico, 2019).

$$\Gamma(t_0) = \frac{1}{na} \begin{bmatrix} \frac{2}{\eta}e\sin M_0 & \frac{2}{\eta}(1 + e\cos M_0) & 0 \\ -\frac{2\eta^2}{(1 + e\cos M_0)} & 0 & 0 \\ \eta\sin u_0 & \eta\frac{(2 + e\cos M_0)\cos u_0 + e_{x0}}{(1 + e\cos M_0)} & \frac{\eta e_{y0}}{\tan i}\frac{\sin u_0}{(1 + e\cos M_0)} \\ -\eta\cos u_0 & \eta\frac{(2 + e\cos M_0)\sin u_0 + e_{y0}}{(1 + e\cos M_0)} & -\frac{\eta e_{x0}}{\tan i}\frac{\sin u_0}{(1 + e\cos M_0)} \\ 0 & 0 & \eta\frac{\cos u_0}{(1 + e\cos M_0)} \\ 0 & 0 & \eta\frac{\sin u_0}{(1 + e\cos M_0)} \end{bmatrix} \quad (49)$$

Given these relations, the final state at t_f can be obtained from a given initial condition and control inputs at t_0 through the Eq. (50).

$$\Delta\alpha_f^{qns} = \Phi(t_0, t_f)\Delta\alpha_0^{qns} + \Phi(t_0, t_f)\Gamma(t_0)[\delta V_R \quad \delta V_T \quad \delta V_N]^T \quad (50)$$

With this equation, it is possible to integrate delta velocities (ΔVs) as control inputs to obtain final relative states in the form of quasi-nonsingular orbital elements.

2.2.4   Relative Motion Prediction using Two Line Elements

As stated in Chapter 2.2.2, relative orbital elements are used for cluster flying design and control. In terms of orbit control, it is also wise to use mean orbital elements as discussed in Chapter 2.1.4.2. Here, it is possible to make use of relative TLEs and extract mean elements for cluster control as well as initial relative states for cluster flying design. When there are no tight relative control requirements, the relative TLEs can be useful in operational analysis as discussed by (Kirschner M., 2001). It is also discussed that the accuracy of differentiating states resulting from TLEs is about 30-100 m. in radial and cross-track and better than 500 m. in along-track direction.

In order to check the accuracy of relative TLEs, the scenario specified in Table 2.4 is used as reference and TLEs are fit for the two spacecraft with high fidelity orbit propagation. Finally, 30 days propagation is performed and the resulting relative distance errors are presented in Figure 2.23.
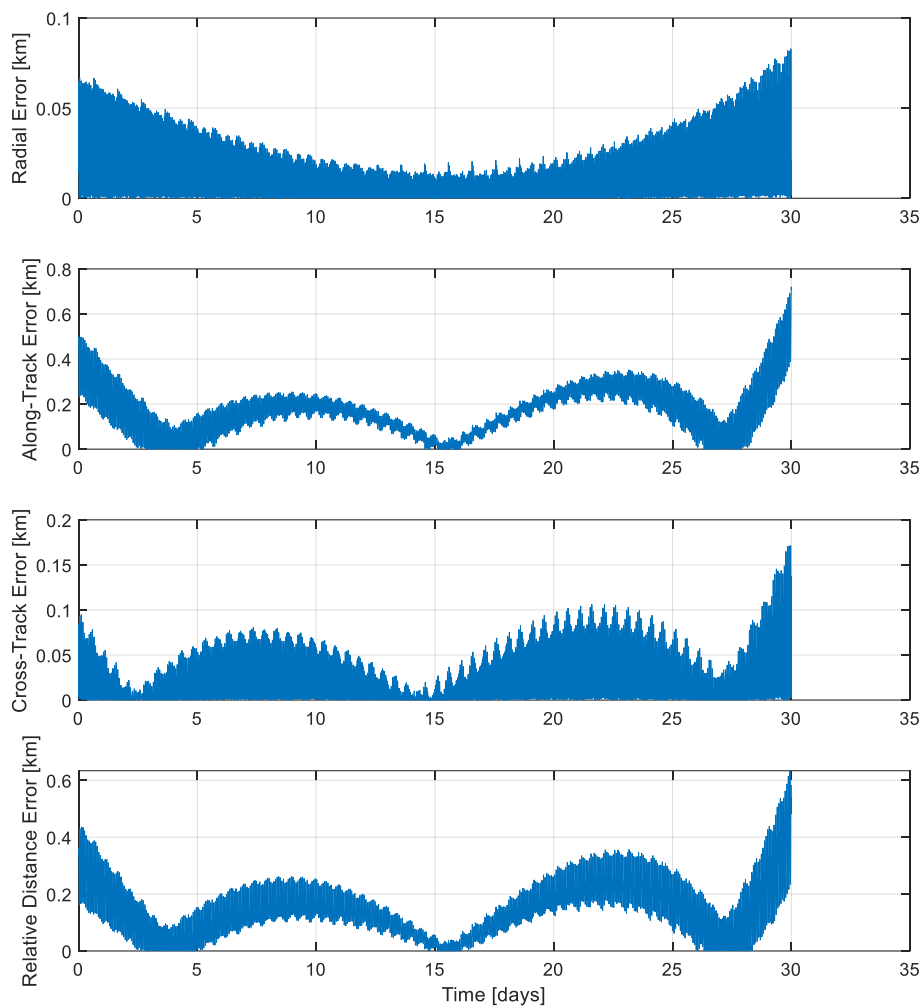
Figure 2.23. Relative motion error of relative TLEs for 30 days propagation

As it can be seen from these results, the errors are compatible with the ones presented by (Kirschner M., 2001). In addition, the ratio of relative distance error to the magnitude of relative distance is provided in Figure 2.24.
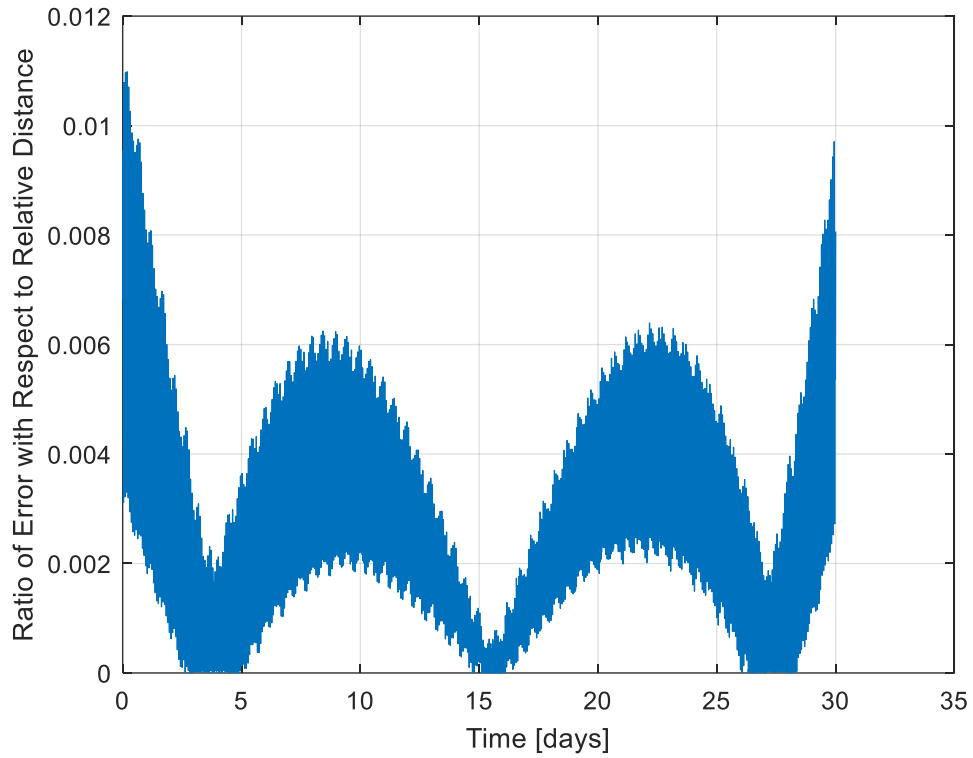
Figure 2.24. Relative motion error ratio of relative TLEs for 30 days propagation

It can be seen that the maximum error is below 1% and it should be noted that the TLEs in this case are fitted for a 30 days propagation. Therefore, a reduction in error can be possible for a TLE fit with shorter duration.

In the light of these discussions, relative TLEs can be used for cluster flying design and analysis as well as cluster control for reconfiguration purposes. Also, a safety distance can be set in the order of 100 m. in radial and cross-track directions.

CHAPTER 3

CLUSTER FLYING DESIGN, EVALUATION AND OPTIMIZATION

For the design, evaluation and optimization of cluster flying, a framework which incorporates several methodologies is developed. The schematic of this framework is given in Figure 3.1 to serve as a roadmap of the overall methodology.
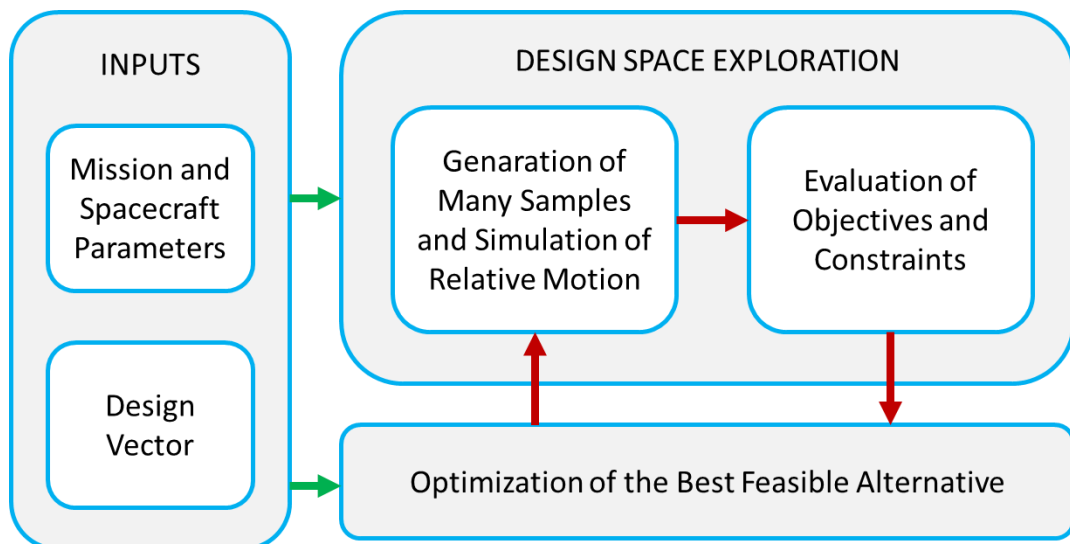
Figure 3.1. Cluster Flying Design and Evaluation Framework

The necessary components of this framework are; relative orbit design and propagation; uncertainty propagation and probability of collision calculation; cluster flying objective functions constraints and design variables, and finally, design space exploration and associated optimization. These are explained in the following subchapters respectively.

3.1 Relative Orbit Design and Propagation for Cluster Flying

As described in Chapter 2.2.2, relative orbits can be defined by introducing small differences in orbital elements of a reference orbit. Once relative orbits are defined, the relative initial conditions and relative distances can be obtained between spacecraft in the cluster as described in Chapter 2.2.1. In this manner, a flowchart is given in Figure 3.2 to provide an oversight of this process starting from reference orbit to determination and evaluation of resulting trajectories for cluster flying design.
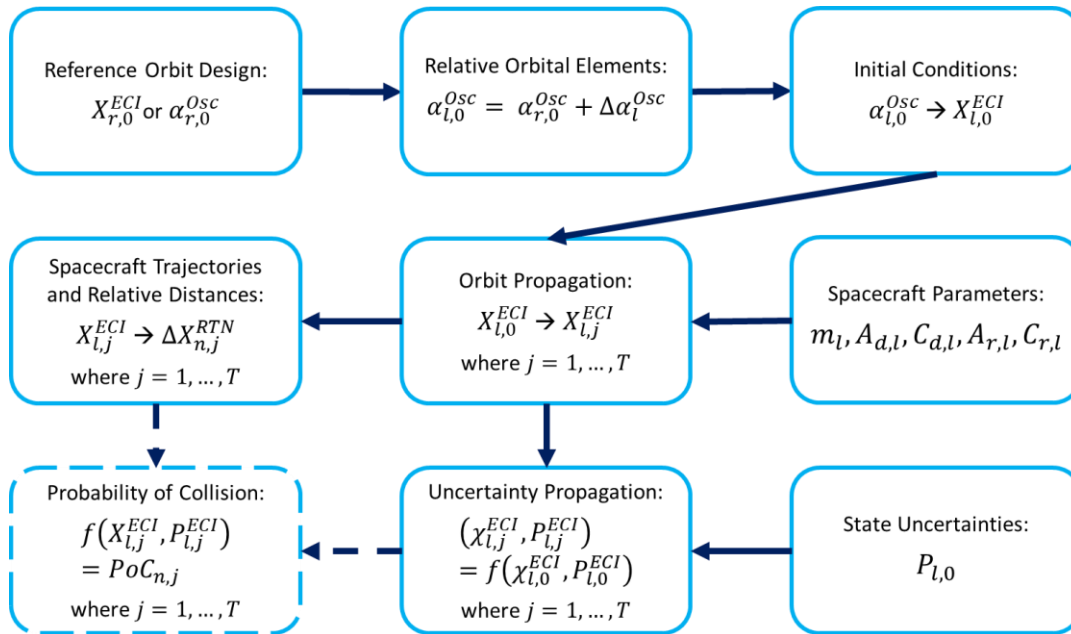
Figure 3.2. Numerical Propagation of Relative Motion and Determination of Relative Distances and Probabilities of Collision

In this approach, objective and constraint functions based on relative distances and probability of collision (PoC) can be evaluated with the relative position and covariance outputs which are generated through numerical orbit propagation for a given set of cluster flying variables, i.e. relative orbital elements (generated from the design vector) as well as spacecraft specific parameters mass m_l, drag area, $A_{d,l}$,

drag coefficient, $C_{d,l}$, Solar radiation pressure area, $A_{r,l}$, and Solar radiation pressure coefficient, $C_{r,l}$.

The first step in this process is to design a mission specific reference orbit. Once the reference orbit (denoted by r) is designed, the specific cartesian state vector, $X_{r,0}^{ECI}$ (initial condition), or osculating orbital elements, $\alpha_{r,0}^{Osc}$, in ECI are found. Then the relative orbital elements, $\Delta\alpha_l^{Osc}$, are introduced to find initial conditions, $X_{l,0}^{ECI}$, (state vectors in ECI) of all spacecraft (denoted by l) in the cluster. The transformations between the cartesian states and orbital elements are performed by following the definitions stated in Chapter 2.1.2.

The second step in the process is the high precision numerical propagation of initial conditions of spacecraft in the cluster to extract trajectories, $X_{l,j}^{ECI}$, of each spacecraft and relative distances, $\Delta X_{n,j}^{RTN}$, between the spacecraft. Here, $l = 1, \dots, N$ defines the spacecraft index within a N-spacecraft cluster, $j = 1, \dots, T$ defines the time instants until final condition at T and $n = 1, \dots, M$ defines the specific combination index between any two spacecraft. For instance, for a 5-spacecraft cluster where $N = 5$, the 2-combinations becomes $C_k^N = \frac{N!}{k!(N-k)!} = \frac{5!}{2!(5-2)!} = 10$. In this manner, relative distances between any 2 spacecraft (hence k is always 2) can be calculated with M combinations. In addition, spacecraft parameters such as mass, m, drag area, A_d, drag coefficient, C_d, solar radiation pressure area, A_r, solar radiation pressure coefficient, C_r, are also input to the propagation of spacecraft orbits. With this, it is possible to introduce differences in these parameters, for instance different mass and drag areas, in case of a heterogeneous distributed space system where physical parameters may differ.

In real life operations, the orbit information is always associated with some uncertainty. This uncertainty is expressed in 6 x 6 matrix of position and velocity covariance as well as cross covariance terms. In the final step, the initial state uncertainties expressed in covariance matrix, $P_{l,0}$, are propagated via unscented transform such that the instantaneous covariance information, $P_{l,j}$, are obtained for

whole trajectory. Then, this covariance information is used for instantaneous probability of collision, $PoC_{n,j}$, calculation for all combinations. With this, it becomes possible to assess safety with a quantitative parameter which incorporates state uncertainties. The propagation of uncertainties and calculation of PoC are explained in detail in Chapter 3.2.

In summary, this numerical approach provides opportunity to improve the fidelity of cluster flying design by incorporating high precision orbital dynamics, spacecraft parameters, navigation uncertainties as well as incorporating differences in spacecraft parameters and their effects on the dynamics of relative motion in case of a heterogeneous system. With this method, it is possible to do the most realistic design and operational analysis for spacecraft cluster flying. However, since this methodology depends on complicated numerical methods, the drawback becomes the high computational demand.

In order to define general boundaries of a cluster with less computational demand, a methodology which relies on SGP4 analytical model is also developed. Similar to the one provided in Figure 3.2, a flowchart is also given in Figure 3.3 to provide an oversight of this process starting from reference orbit to determination and evaluation of resulting trajectories for cluster flying design.
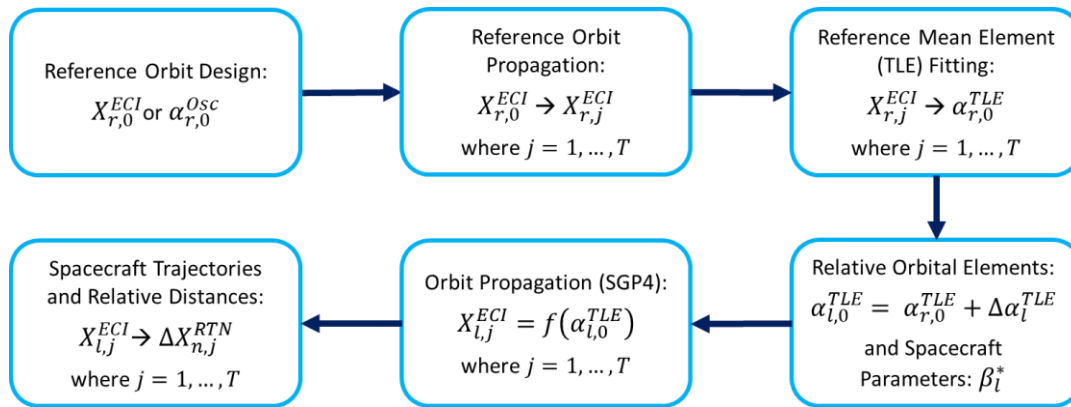
Figure 3.3. Analytical Propagation (SGP4) of Relative Motion and Determination of Relative Distances

The first step is similar to the numerical methodology where mission specific reference orbit with an initial condition, $X_{r,0}^{ECI}$, is determined initially. This initial condition is propagated with a high precision orbit propagator and the reference trajectory, $X_{r,j}^{ECI}$, is obtained for time interval $j = 1, \dots, T$. The reference trajectory is used to fit reference mean orbital elements (TLEs in SGP4 case), $\alpha_{r,0}^{TLE}$. Then the relative orbital elements, $\Delta\alpha_l^{TLE}$, are introduced to find mean orbital elements (TLEs), $\alpha_{l,0}^{TLE}$, of all spacecraft (denoted by l) in the cluster.

The second step in the process is the analytical propagation of mean orbital elements, $\alpha_{l,0}^{TLE}$, of spacecraft in the cluster to extract trajectories, $X_{l,j}^{ECI}$, of each spacecraft and relative distances, $\Delta X_{n,j}^{RTN}$, between the spacecraft for time interval $j = 1, \dots, T$ and combination index $n = 1, \dots, M$. Here, it should be noted that the SGP4 output is originally provided in TEME as described in Chapter 2.1.4.1. Therefore, this TEME state is converted to ECI by making use of precession, $\mathcal{P}(t)$, and nutation, $\mathcal{N}(t)$, matrices as well as Greenwich true sidereal angle. In addition, the physical differences of spacecraft in the cluster can be input by specifying different SGP4 drag parameters, β_l^*, in case of a heterogeneous distributed space system.

With this approach, objective and constraint functions based on relative distances can be evaluated with the relative position outputs which are generated through analytical orbit propagation (SGP4) for a given set of cluster flying variables, i.e. relative orbital elements (generated from the design vector). With this method, it is still possible to perform design and operational analyses for spacecraft cluster flying with no very high-fidelity requirement such as coarse mission analysis and maneuver planning. Since this methodology depends on analytical orbit propagation method, the computational demand is not high.

3.2 Uncertainty Propagation and Probability of Collision

In order to perform design and operational analysis for cluster flying as realistic as possible, consideration of navigation uncertainties become vital. In reality, an orbit

determination result, i.e., orbital elements or a state vector, almost always comes with covariance information. Therefore, when assessing the collision or evaporation (when spacecraft exceeds maximum relative distance constraints) risks, the state uncertainty should be also considered while propagating an orbit, or initial conditions. Here, (Ya-zhong & Zhen, 2017) suggests uncertainty propagation can be performed more accurately and efficiently by employing nonlinear uncertainty propagators. For this, a computationally efficient and moderately precise nonlinear uncertainty propagation method, unscented transform, is used which is developed by (Julier, Uhlmann, & Durant-Whyte, A New Method for the Nonlinear Transformation of Means and Covariances in Filters and Estimators, 2000) and (Julier & Uhlmann, Reduced Sigma Point Filters for the Propagation of Means and Covariances Through Nonlinear Transformations, 2002). Having the state uncertainty information for spacecraft, it is also possible to calculate the probability of collision. As stated previously in Chapter 3.1, PoC provides a quantitative assessment for safety considerations. In the following chapters 3.2.1 and 3.2.2 the unscented transform and calculation of PoC are explained.

3.2.1   Unscented Transform

The uncertainty propagation for a state vector with N states is performed by using unscented transform (UT) methodology. This is achieved by propagating 2N+1 particles (+1 is the mean and 2N particles are distributed around the mean for N states) which are also called sigma points derived from the state vector and, then, a new mean at the terminal instant is synthesized using the propagated particles. This process is illustrated by Figure 3.4 and described by Eq. (51) and (52). The efficiency of unscented transform process with its comparison to actual (Monte Carlo sampling) and linear covariance propagation is also represented in Figure 3.4.
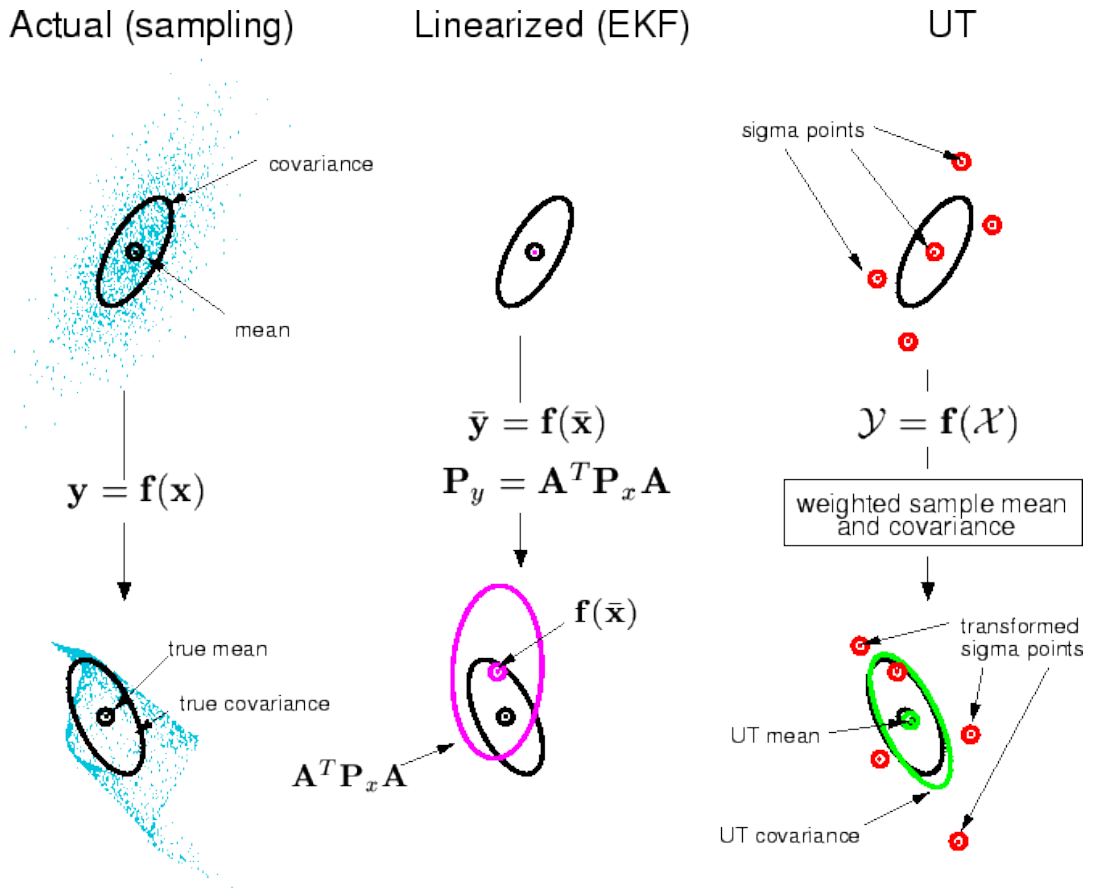
Figure 3.4. Representation and comparison of UT by (Wan & van der Merwe, 2001)

In the example in Figure 3.4, a two-dimensional system with 2 states (N=2) is considered. Here, UT captures the covariance closer to the real case with only 5 particles (2N+1 = 5) and provides a superior performance when compared to linear transform of the covariance in the case of extended Kalman filter. The basic formulation of the UT is provided in Eq. (51).

$$\mathcal{Y}_i = f(\mathcal{X}_i)$$

$$\bar{y} = \sum_{i=0}^{2N} W_i^{(m)} \mathcal{Y}_i \tag{51}$$

$$P_y = \sum_{i=0}^{2N} W_i^{(c)} \{\mathcal{Y}_i - \bar{y}\}\{\mathcal{Y}_i - \bar{y}\}^T$$

Here, $i = 0, \dots, 2N$ represents particles for N states, f represents the nonlinear system dynamics which propagates the initial particles $\mathcal{X}_i$ to obtain propagated particles, $\mathcal{Y}_i$. Then, $\bar{y}$ is the synthesized mean obtained by using the weights $\mathcal{W}_i^{(m)}$ defined for each particle. Similarly, final covariance, P_y, is synthesized by using the weights $W_i^{(c)}$ for each particle, and the deviation of the particles $\mathcal{Y}_i$ from the mean $\bar{y}$. Here many techniques such as the symmetric set and symmetric extended set are employed by (Julier & Uhlmann, Unscented Filtering and Nonlinear Estimation, 2004) for the selection of the sigma-points and the associated weights. The details of the UT formulation including generation of particles and calculation of weights for mean and covariance syntheses are provided in Eq. (52).

$$\mathcal{X}_0 = x$$
$$\mathcal{X}_i = x + \left(\sqrt{(N + \lambda)P_x}\right)_i, \qquad i = 1, \dots, N$$
$$\mathcal{X}_i = x - \left(\sqrt{(N + \lambda)P_x}\right)_i, \qquad i = N + 1, \dots, 2N$$
$$\mathcal{W}_0^{(m)} = \lambda / (N + \lambda) \tag{52}$$
$$\mathcal{W}_0^{(c)} = \lambda / (N + \lambda) + (1 - \alpha^2 + \beta)$$
$$\mathcal{W}_i^{(m)} = \mathcal{W}_i^{(c)} = 1 / [2(N + \lambda)]$$
$$\lambda = \alpha^2(N + \mathcal{K}) - N$$

The particle with $i = 0$, represents the mean and the covariance of the initial state, x, is represented by P_x. The coefficients are selected such that $\alpha = 1, \mathcal{K} = 0, \beta = 2$.

With this formulation, a simulation is performed to demonstrate the evolution of covariance and mean for orbital motion. In this simulation, covariance in RTN is set for position and velocity as $P_{pos,0}^{RTN} = diag[4^2 \quad 7.5^2 \quad 6^2]$ in meters^2 and $P_{vel,0}^{RTN} = diag[0.008^2 \quad 0.007^2 \quad 0.0045^2]$ in (meters/second)^2 respectively with representative values obtained from a realistic orbit determination process. For simulation of 1 day with step size of 240 seconds, the evolution of mean position error and standard deviation are provided in Figure 3.5 and in Figure 3.6 respectively.
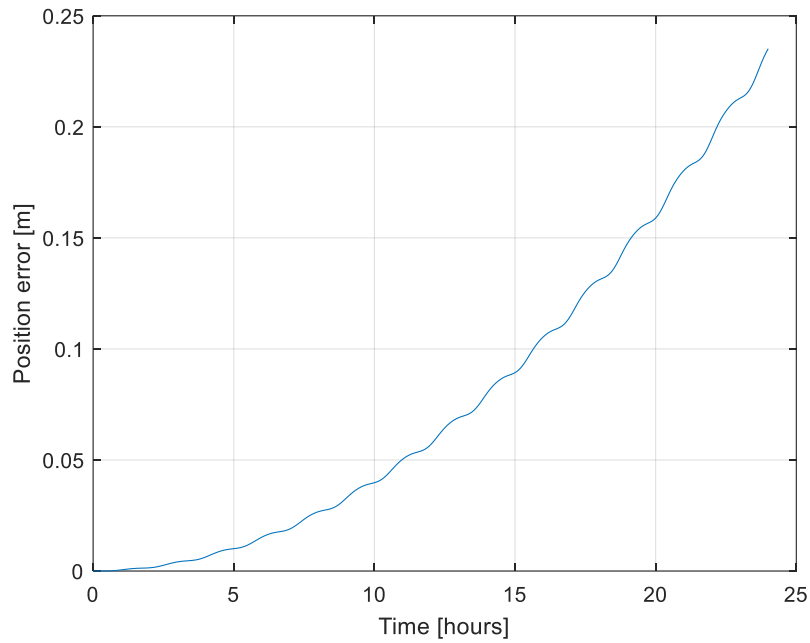
Figure 3.5. Evolution of mean position error due to covariance with UT
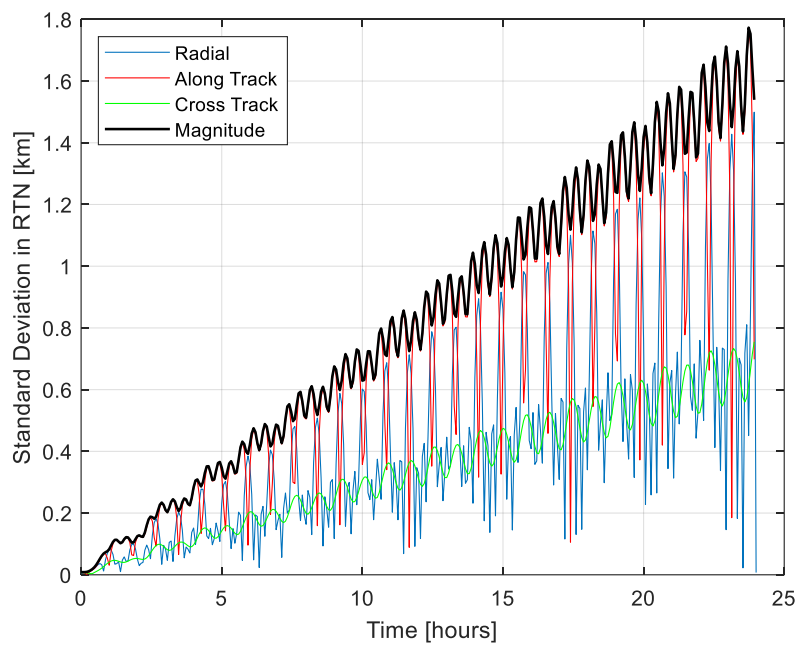
Figure 3.6. Evolution of position standard deviation with UT (black curve is the norm of position standard deviation; blue, red and green are the position standard deviation in radial (R), along-track (T) and cross-track (N) directions respectively)

As it can be seen from above plots, the magnitude of covariance grows linearly over time and the biggest uncertainty growth appears in the along-track direction. In addition, the error of position mean grows exponentially in a day, however, the magnitude of error is not significant with the given initial covariance information.

3.2.2   Probability of Collision (PoC)

PoC represents the likelihood that the range between two objects may become less than a radius R during a close approach of 2 spacecraft. Having the state uncertainty information for spacecraft, it is also possible to calculate the probability of collision. For this, the standard collision probability assessment scheme described in the following is based on the formulations by (Alfriend, et al., 1999) and (Akella & Alfriend, 2000). Here, the combined covariance of any 2 spacecraft is transformed into *conjunction plane* (also called B plane) which is perpendicular to the relative velocity vector, Δv. Then, the 2-dimensional integral of combined uncertainty, P_B, is calculated over the circular conjunction area, A_c, which is centered at the relative position vector, Δr, with a radius, R_c, calculated as the sum of the radii of 2 spacecraft. This is summarized in the Figure 3.7.
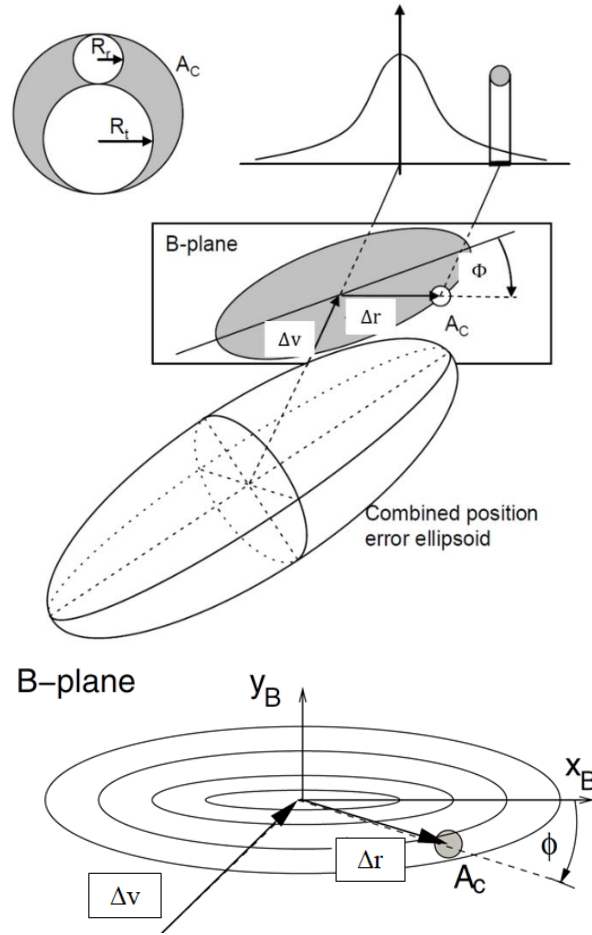
Figure 3.7. Representation of Conjunction Plane (B-plane perpendicular to $\Delta\vec{v}$), Combined and Projected Covariance, P_B, and Conjunction Area A_c. (Krag, et al., 2016)

Here, x_B and y_B represent the major and minor axes and ϕ represents the angular position of the conjunction area, A_c. Then the probability of collision, P_c, can be calculated through the integral given in Eq. (53) (Alfriend, et al., 1999).

$$P_c = \frac{1}{2\pi\sqrt{\|P_B\|}} \int_{-R_c}^{+R_c} \int_{-\sqrt{R_c^2 - x_B^2}}^{+\sqrt{R_c^2 - x_B^2}} exp\left(-\frac{1}{2}\Delta r_B{}^T P_B{}^{-1}\Delta r_B\right) \, dy_B \, dx_B \qquad (53)$$

In order to calculate this integral, (Foster & Estes, 1992) derived a model using polar coordinates in the conjunction plane and (Chan, 2003) developed an analytical

61

expression for the calculation of this integral. Also, (Patera, 2003) defines the integral which is particularly relevant for items such as defining the risk of a particular set of trajectories. Finally, (Alfano & Oltrogge, 2018) provides an overview of the types of PoC estimation techniques. In this paper, the calculation method of (Foster & Estes, 1992), described by Eq. (54), is adopted to reflect the conventional approach which satellite operators commonly practice.

$$P = \frac{1}{2 \cdot \pi \cdot \sigma u \cdot \sigma w} \cdot \int_{0}^{OBJ} \left[\int_{0}^{2 \cdot \pi} \exp\left[\frac{-1}{2} \cdot \left[\left(\frac{R_0 \cdot \sin(\phi) - r \cdot \sin(\theta)}{\sigma u} \right)^2 + \left(\frac{R_0 \cdot \cos(\phi) - r \cdot \cos(\theta)}{\sigma w} \right)^2 \right] \right] \cdot r \, d\theta \right] dr \tag{54}$$

Minor Axis, y_b Major Axis, x_b

In this equation, OBJ refers to combined object radius, R_c, R_0 refers to relative position vector, Δr and σ_u and σ_w are standard deviations of combined and projected covariance, P_B, projected at minor and major axes respectively. For validation and benchmark purposes, 2 real operational cases, provided by Combined Space Operations Center (CSpOC), are compared with the calculated (Eq. (54)) ones and presented in Table 3.1.

Table 3.1 Validation of PoC Calculations

Parameter	*Case 1*	*Case 2*
σx [m]	361.3	1859.8
σy [m]	45.6	62.6
Δr [m]	170	255
Φ [°]	33.4	149.8
Rc [m]	5.3	8.8
PoC, Foster	9.632×10^{-5}	4.053×10^{-5}
PoC, CSpOC	8.043×10^{-5}	4.307×10^{-5}

As it can be seen from these results, PoC can be calculated in the same order when compared to CSpOC's values. Since the full assumptions of CSpOC are not known (such as the value of combined object radius when it is not available), small differences in PoC values are acceptable as long as the order is same.

When the PoCs are considered as a risk measure for close approach events, the historical trend of practices at European Space Operations Center (ESOC) provided by (Funke, et al., 2018) is reproduced in Figure 3.8.

Threshold to trigger …	Threshold to trigger maneuver	Maneuver target	Period of use
Meeting: PoC > 10^{-4} Distance < 300 m.	PoC > 10^{-3} to 5×10^{-3} Distance < 300 m.	None	2003-2011
Tracking: PoC > 10^{-4} Distance < 300 m.	Distance based (no maneuver for low risks)	None	2006-2011
Meeting: After alert is received from CSpOC	Radial Distance < 3σ chaser + 3σ target + cross section radii	Radial Distance > 3σ chaser + 3σ target + cross section radii	2010
Meeting: PoC > 10^{-4}	PoC > 10^{-4}	PoC < 10^{-6}	2010-2013
Meeting: PoC > 10^{-4}	PoC > 10^{-4}	PoC < 10^{-6}	2013-2016
Meeting: Mission specific PoC threshold	Mission specific PoC threshold	Mission specific PoC threshold	Since 2016

Figure 3.8. Screening Methods and Associated Thresholds at ESOC (Funke, et al., 2018)

As it can be seen from above definitions at ESOC, the trigger threshold of collision avoidance maneuvers was set to for PoC above 10^{-4} until it has been specified to mission specific levels later. Therefore, the operators can consider the navigation information uncertainties and confidence in operational practice when it comes to setting alarm and maneuvering thresholds.

3.3 Cluster Flying Constraints, Objectives and Design Variables

There are several constraints and objectives in the case of a mission with multiple spacecraft. Mission and platform characteristics, which may vary for different spacecraft, play an important role while realizing orbital dynamics operations. In this manner, it is important to consider realistic parameters, objectives and constraints stemming from several operational scenarios and limitations for cluster flying design problem. Some of the aspects, requirements and parameters for cluster flying are summarized in Table 3.2.

Table 3.2 Comparison of Cluster Flying Aspects and Associated Requirements

Aspect	Requirement	Parameter	Action
Safety	Collision Avoidance	Distance	Increase
Station Keeping	Orbit Maintenance	Distance to Reference Orbit	Decrease
Inter-spacecraft Communication Availability	Visibility Maintenance, Evaporation Avoidance	Line of Sight, Distance	Maintain Line of Sight, Decrease Distance
Propellant Consumption	Naturally Stable or Feasible Orbits	Maneuver	Decrease
Reconfigurability	Cooperative Maneuvering	Maneuver	Increase

From Table 3.2, it may be observed that there are conflicting aspects such as safety and inter-spacecraft communications. For safety, it is wise to increase relative distances, however, short ranges are better for communication performance. In addition, the relative distance shall not exceed a maximum range which can be called

as evaporation of cluster. Similarly, station keeping and safety are also conflicting in terms of relative distance. For station keeping, the spacecraft shall be kept as close as possible to the mission specific reference orbit therefore it may cause cluster to shrink and reduce relative distances. Also, it is wise to reduce propellant consumption however reconfigurability is important for cluster flying and therefore these two are conflicting objectives.

In order to design a cluster which maximizes safety, station keeping and inter-spacecraft communications relative distance-based objectives and constraints can be defined. In addition, probability of collision is also a good measure for safety as described in Chapter 3.2.2. However, it is necessary to analyze the geometry of relative orbits and covariance for both cases.

As described in Chapter 2.2.1, a full harmonic closed form solution is possible, however, the cartesian formulation does not provide an insight into the geometrical aspects of relative motion. Here, a formulation of linearized relative motion based on relative orbital elements with relative eccentricity and inclination vectors is provided by (Montenbruck, Kirschner, D'Amico, & Bettadpur, 2006) and (D'Amico & Montenbruck, 2006). This formulation which is a general closed form solution of HCW equations by using the mean argument of latitude, u, as an independent variable is given in Eq. (55).

$$\Delta R = \Delta a - a\delta e \cos(u - \varphi)$$

$$\Delta T = a\Delta l - \frac{3}{2}\Delta a(u - u_0) + 2a\delta e \sin(u - \varphi) \qquad (55)$$

$$\Delta N = a\delta i \sin(u - \theta)$$

where $\Delta l = \Delta u + \Delta\Omega \sin i$ is the relative mean longitude, $\varphi = \text{atan}(\Delta e_y/\Delta e_x)$ and $\theta = \text{atan}(\Delta i_y/\Delta i_x)$ are relative perigee and argument of latitude respectively. Here, δe or δi are the magnitudes of the eccentricity and inclination vectors which are also defined in Eq. (46). With this formulation, it is not only possible to interpret geometrical implications of but also have a powerful tool for cluster flying design. In the case of close relative orbits assuming $\Delta a = \Delta l = 0$, the Eq. (55) becomes

$$\Delta R = -a\delta e \cos(u - \varphi)$$
$$\Delta T = 2a\delta e \sin(u - \varphi) \tag{56}$$
$$\Delta N = a\delta i \sin(u - \theta)$$

From Eq. (56), it can be deduced that the relative motion within the plane (or in-plane) become an ellipse with semimajor axis $2a\delta e$ in along-track and semi-minor axis $a\delta e$ in radial directions for close relative orbits where $\Delta a = \Delta l = 0$. In addition, the gradual increase of along-track separation is also canceled by selecting $\Delta a = 0$. Similarly, out of plane motion can be described by $a\delta e$ in radial and $a\delta i$ in cross-track directions. These geometries are presented in the Figure 3.9.
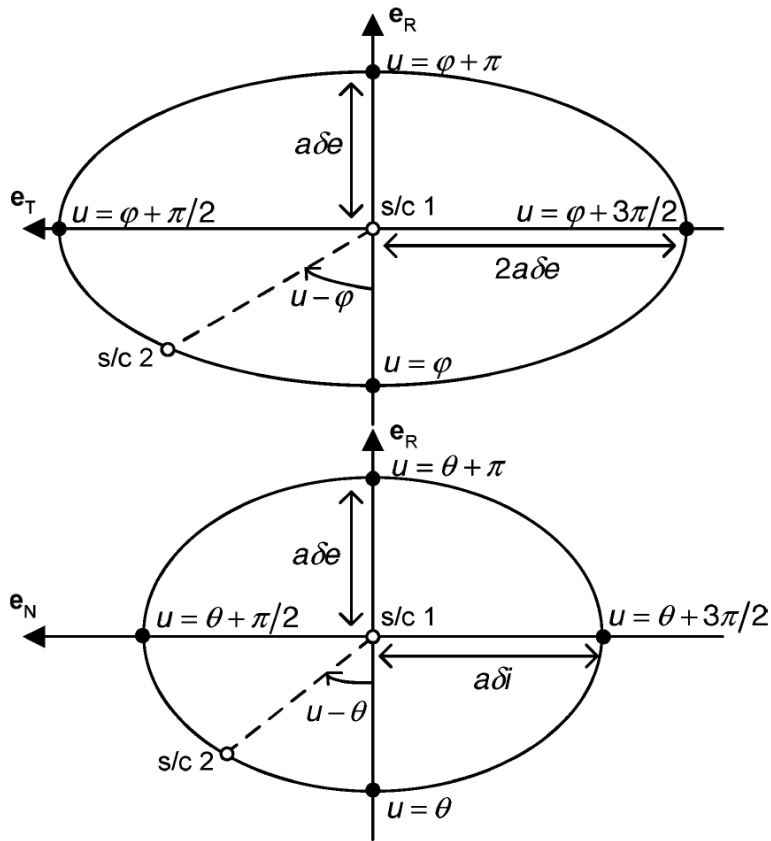
Figure 3.9. In-plane (Radial and Along-track) and out of plane (Radial and Cross-track) relative motion based on relative eccentricity and inclination vectors (D'Amico & Montenbruck, 2006).

66

From the Eq. (56) and Figure 3.9, it can be interpreted that it is possible to investigate in-plane and out of plane motion separately and understand geometrical applications such as possible minimum and maximum distances by using relative eccentricity and inclination vectors as design parameters. For instance, a minimum distance can be ensured by parallel separation of relative eccentricity and inclination vectors through specifying $\varphi = \theta$. This condition would ensure a minimum distance in ΔR when $u = \varphi + k\pi$ where $k = 0,1,2 \dots$ and $\Delta T = 0$. Similarly, it is possible to ensure a distance in ΔN when $u = \varphi + \frac{k}{2}\pi$ and the separation in radial direction disappears, $\Delta R = 0$. In this manner, it is especially important to ensure a minimum distance in out of plane described by radial and cross-track directions (or RN plane) since the uncertainties in along-track direction are much higher as described in Chapter 3.2.1 and shown in Figure 3.6. To sum up, the relative maximum and minimum distances $\Delta R, \Delta T$ and ΔN can be related with $\Delta e_{x,y}$ and $\Delta i_{x,y}$ vectors between the spacecraft as described in Eq. (57).

$$\begin{bmatrix} \Delta R \\ \Delta T \\ \Delta N \end{bmatrix}_{min,max} = f\big(a, \Delta e_{x,y}, \Delta i_{x,y}\big) \tag{57}$$

Here, minimum distance relation for radial and cross-track directions is derived by (Eckstein, Rajasingh, & Blumer, 1989) and given in Eq. (58).

$$\Delta RN_{min}$$
$$= \frac{\sqrt{2}a|\Delta e||\Delta i|\cos(\theta - \varphi)}{\left\{|\Delta e|^2 + |\Delta i|^2 + \sqrt{|\Delta e|^4 + |\Delta i|^4 - 2|\Delta e|^2|\Delta i|^2 \cos 2(\theta - \varphi)}\right\}^{1/2}} \tag{58}$$

By using Eq. (55), (56) and (58) operational constraints on station-keeping, safety and inter-spacecraft communications can be introduced by defining bounds on minimum and maximum relative distances between the spacecraft based on realistic parameters, objectives and constraints stemming from several operational scenarios and limitations. For instance, a minimum distance constraint can be defined to ensure the safety through collision avoidance and a bound on maximum distance can be defined to ensure inter-spacecraft link availability through evaporation (or maximum

range violation) for the cluster. Station-keeping can be also ensured if the minimum and maximum distance constraints are defined such that the deviations from the reference orbit are within the acceptable limits. The constraints derived from these considerations are summarized in Eq. (59).

$$
\begin{aligned}
\text{Eq. (58)}: \Delta RN_{min} &= f\left(a, \Delta e_{x,y}, \Delta i_{x,y}\right) \geq d_{min} \\
\Delta R_{n,j}^2 + \Delta N_{n,j}^2 &\geq d_{min}{}^2 \\
\Delta R_{n,j}^2 + \Delta T_{n,j}^2 + \Delta N_{n,j}^2 &\leq d_{max}{}^2
\end{aligned}
\tag{59}
$$

With these constraints, it is possible to ensure a minimum distance, d_{min}, in radial – cross-track (RN) plane and a maximum range, d_{max}, in 3 dimensions. With the first relation of Eq. (59), initial $\Delta e_{x,y}$ and $\Delta i_{x,y}$ vectors are designed to ensure $\Delta RN_{min} \geq d_{min}$ and the second relation is for trajectory. Here, the reason for introducing minimum distance constraint only on the RN plane is to ensure a safe distance between any spacecraft without relying on the distance in along-track direction for which the navigation uncertainties are the highest when compared to other directions as described previously. This condition may be visualized from Figure 3.10.
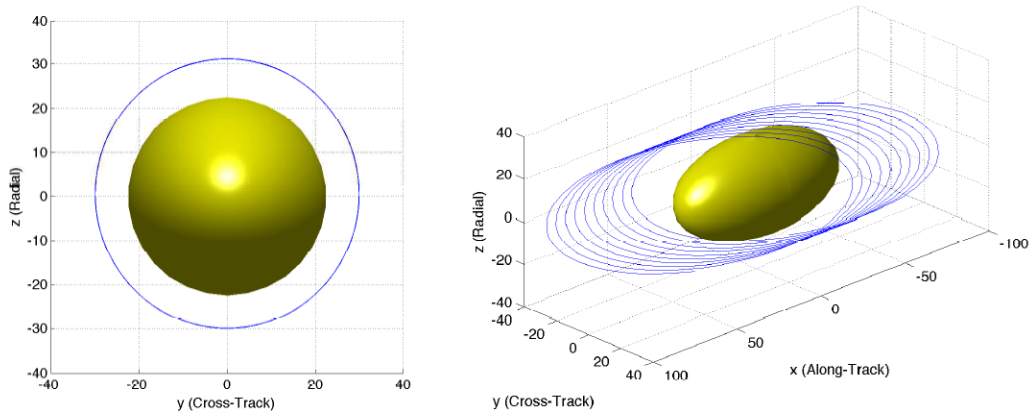
Figure 3.10. Out of plane (Radial and Cross-track, Left) and three dimensional (right) representations of relative motion with uncertainty of chief orbit where a minimum distance is ensured in RN plane. (Mueller, Griesemer, & Thomas, 2013)

If $\Delta l \neq 0$ then the minimum and maximum distance constraints may also be written in 3 dimensions as described in Eq. (60).

$$d_{min}^2 \leq \Delta R_{n,j}^2 + \Delta T_{n,j}^2 + \Delta N_{n,j}^2 \leq d_{max}^2 \qquad (60)$$

When specifying boundaries on relative distances, the requirements scaling introduced by (Gill, 2011) for relative motion guidance, control and navigation can be considered. These scaling laws are summarized in Table 3.3. Based on this table, minimum distance or separation constraint can be specified as 100 m. by assuming a relative navigation accuracy of cm. levels (Persson, D'Amico, & Harr, 2010).

Table 3.3 Scaling Laws for Guidance, Navigation and Control Parameters for Formation Flying (Gill, 2011).

Parameter	Variable/Relation	Sample Scenario
Spacecraft Separation Requirement	d_l	100 m.
Control Window Size	$d_{cw} = 0.1\, d_l$	10 m.
Control Accuracy Requirement	$d_c = 0.1\, d_{cw}$	1 m.
Relative Navigation Accuracy Requirement	$d_n = 0.1\, d_c$	0.1 m.

Finally, constraints on design variables, ρ_l, for each spacecraft, l can be also defined as provided in Eq. (61).

$$\rho_{min} \leq \rho_l \leq \rho_{max} \qquad (61)$$

Using Eq. (59), Eq. (60) and Eq. (61), a design space based on the relative orbit elements and relative distance constraints can be generated.

Depending on the mission specific cases and requirements of the cluster flying, different objective functions can be defined based on relative distances or parameters such as probability of collision to maximize the station keeping and/or safety. For the station-keeping, an objective function which would minimize the relative distances to the reference orbit can be defined as described in Eq. (62).

$$\sum_{l=1}^{N} \sum_{j=1}^{T} \left(\Delta R_{l,j}^2 + \Delta T_{l,j}^2 + \Delta N_{l,j}^2 \right) \tag{62}$$

This objective function, Eq. (62), will imply that any deviation, or distance, of each spacecraft, l, at each discrete time instant, j, from the reference orbit would increase the cost. Therefore, the total cost would become the sum of the deviations of all spacecraft, $l = 1, 2, \ldots, N$, over the simulated time interval which is discretized as $j = 1, 2, \ldots, T$.

Similarly, the objective function which would maximize the safety can be written with the probability of collision as described in Eq. (63).

$$\sum_{n=1}^{M} \sum_{j=1}^{T} PoC_{n,j} \tag{63}$$

This objective function, Eq. (63), will imply that the probability of collision between any two spacecraft, with combination index $n = 1, 2, \ldots, M$ at each time instant, j, would increase the cost. Therefore, the total cost would become the sum of the probabilities of collision between any two spacecraft over the simulated time interval $j = 1, 2, \ldots, T$.

After specifying the objective functions, design variables which would be a selected set of relative orbital elements and their minimum and maximum bounds can be also defined. Initially, design variables can be specified as $\rho = [\Delta e \quad \Delta i \quad \Delta \Omega \quad \Delta \omega]$. With these variables relative orbit configurations can be formed in terms of relative eccentricity and relative inclination vectors which are defined by Δe, $\Delta \omega$ and Δi, $\Delta \Omega$ respectively. Regardless of whether the reference orbit is circular or not, design vectors can be generated with minimum and maximum bounds depending on the mission characteristics. However, it is important to define these boundaries such that the sensitivity of the objective function would be in the same order for different ranges of design variables.

To illustrate this procedure, a near circular Sun-synchronous reference orbit at 685 km (mean) altitude and 10:30 Local Time Descending Node (LTDN) with orbital

elements $e = 0.0022, i = 98.124°, \Omega = 86.717°, \omega = 176.409°$ is considered as a reference example. Here, the maximum separations between a circular reference orbit and derived relative orbits can be quantified as described by reduced form of the Eq. (56) given in Eq. (64).

$$
\begin{aligned}
\Delta R_{max} &\cong a\delta e \\
\Delta T_{max} &\cong 2a\delta e \\
\Delta N_{max} &\cong a\delta i
\end{aligned}
\tag{64}
$$

where δe and δi are the magnitudes of the eccentricity and inclination vectors. Here, it should be noted that, the contribution of relative orbital elements to the maximum distances shall be in the same order. In this manner, the minimum and maximum bounds on the design vector, $\rho_l = [\Delta e_l \quad \Delta i_l \quad \Delta\Omega_l \quad \Delta\omega_l]^T$, are specified as follows:

$$
\begin{aligned}
-0.000525 &\leq \Delta e_l \leq 0.000525 \\
-0.075° &\leq \Delta i_l \leq 0.075° \\
-0.075° &\leq \Delta\Omega_l \leq 0.075° \\
-0.03° &\leq \Delta\omega_l \leq 0.03°
\end{aligned}
\tag{65}
$$

With this design space, the order of the maximum distances would be less than 50 km. when vector magnitudes are calculated for RTN directions. In order to check the relative effectiveness, or sensitivity, of the design variables, a random set of 1000 samples within the design space is generated initially. Then the (scaled) objective function values for Eq. (62) are calculated for 5 spacecraft each having 4 relative orbital elements as design variables. The result of the sensitivity analysis for the sampled design space is shown in the Figure 3.11.
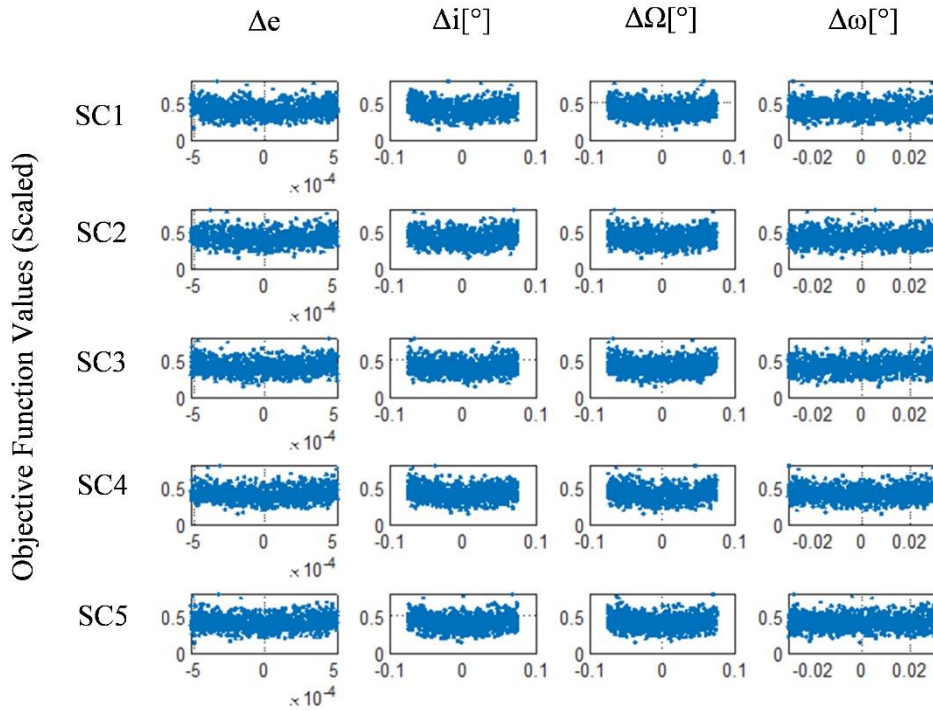
Figure 3.11. Relative Effectiveness of the Design Variables for 5 Spacecraft over a Design Space of 1000 Samples. Each row indicates the specific spacecraft, while the column indicates relative orbital element, Δe, Δi, $\Delta\Omega$ and $\Delta\omega$ respectively.

In Figure 3.11, rows represent each spacecraft and columns represent the relative orbital elements for the specific spacecraft. For a specific row, i.e. spacecraft, each subplot shows the objective function values for a specific relative orbital element in the order of Δe, Δi, $\Delta\Omega$ and $\Delta\omega$. From these figures, it can be seen that the changes in each design variables, or the relative orbital elements, have comparable effects on the scaled objective function. In this example, cross-track elements Δi and $\Delta\Omega$ have wider bounds, therefore, the sensitivity for these elements are relatively higher. However, since the orbit is near circular, sensitivity to design variable $\Delta\omega$ is relatively lower. It should be noted that these sensitivities are valid for a specific objective function, design variables and the bounds on design variables. If the minimum and maximum bounds on $\Delta\omega$ were larger then the sensitivity to the changes in this design variable would have been higher.

72

3.4 Design Space Exploration and Optimization

Since the objectives and constraints are highly nonlinear and the problem is non-convex, a design space exploration based technique is developed to solve the cluster flying design problem. Here, the design space is defined by the boundaries on the design variables as described in Chapter 3.3. Then, a design space exploration is performed within this design space through generating a population of many samples (in the order of thousands) and evaluating the objective and constraint functions for each sample. The samples which are satisfying the constraints, i.e., feasible solutions, are filtered and the one providing the lowest cost value is selected as the initial condition. Finally, this filtered and selected initial condition is further optimized. The steps of the process are summarized in Figure 3.12.
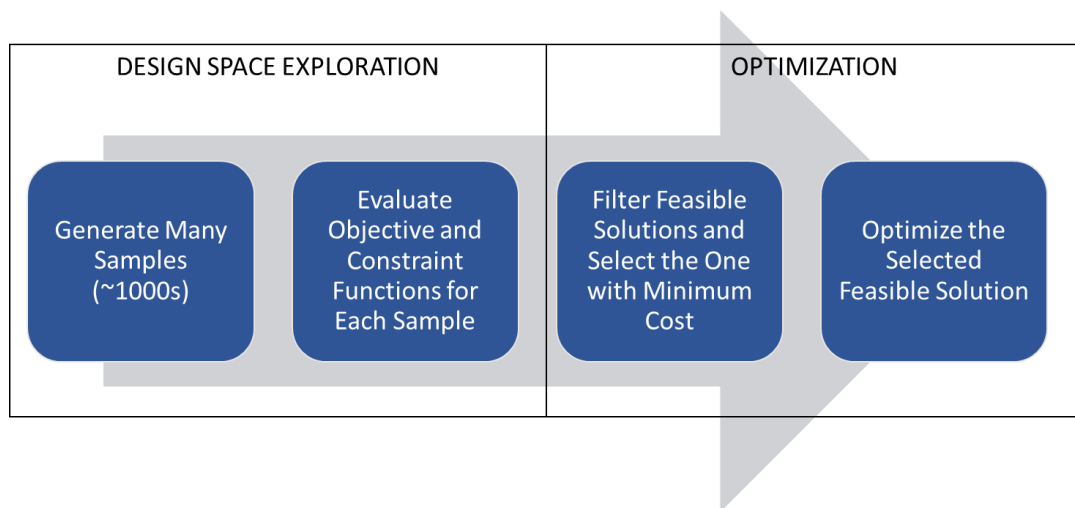
Figure 3.12. Optimization Algorithm Flowchart.

3.4.1 Sampling of Design Space

In the first step of the optimization process, i.e. generation of many samples from design variables, selecting the right sampling method is very important in terms of finding feasible solutions. In addition, the sampling method is related to the quality of the results and length of simulation time. In order to represent the design space

well enough and detect the regions where feasible solutions are located, several methodologies can be utilized. Amongst them, Monte Carlo sampling is the most common methodology. When Monte Carlo sampling is utilized, the computer generates a random number between 0 and 1 for each sample using a uniform distribution. Then, this number is assigned to a value using cumulative distribution function (CDF) which is specific for the problem. This process is illustrated in the Figure 3.13.
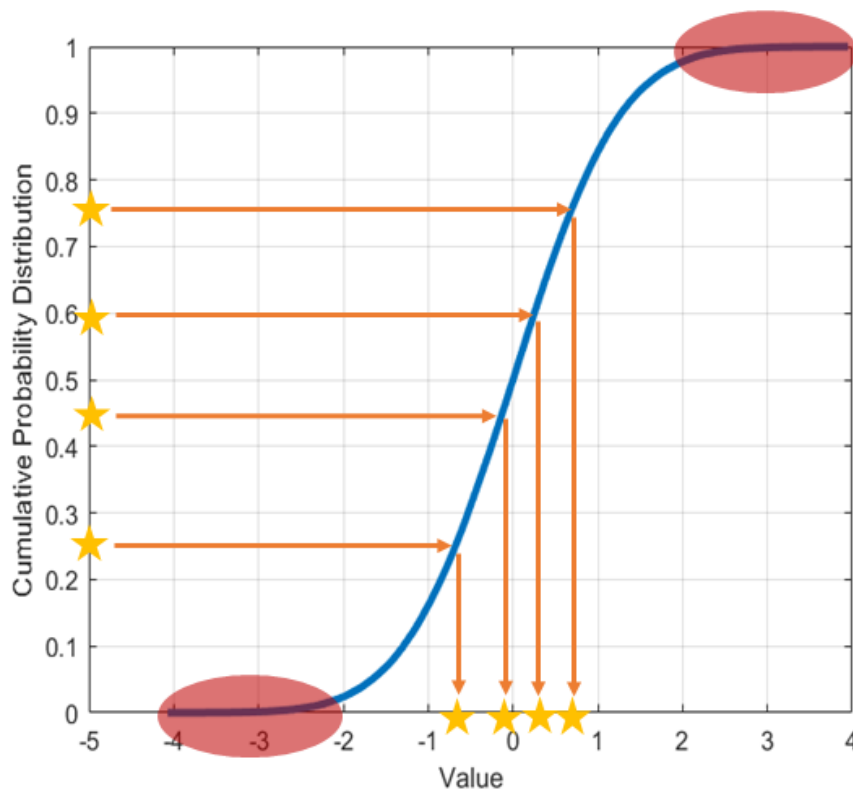
Figure 3.13. Monte Carlo Implementation in Computers.

From the Figure 3.13, it can be deduced that entirely random four numbers (on y-axis) are assigned to a specific value (in x-axis), which would be the sample, using the cumulative probability distribution. Since the chance of having any number from 0 to 1 on y-axis is same for all samples, any sample is generated in a totally random manner and it may fall anywhere within the range of input distribution. Also, new sample points are generated without taking into account the previously generated

74

sample points. However, the more likely outcomes are in the range where the cumulative curve is the steepest. If there are not enough samples, this would cause that the values in the outer ranges (red regions) of the distribution are not represented in the samples and therefore they are not evaluated in the simulations. In order to overcome this problem, very large number of samples is needed to have a good representation of probability distribution. However, as the whole process is fully random (memoryless), it is not possible to recreate a same or similar population from one simulation to another.

In order to explore the design space with reasonable sample number and overcome the difficulties of Monte Carlo methodology, Latin Hypercube Sampling (LHS) method which is developed by (Mckay, Beckman, & Conover, 1979) and implemented by (Iman, Davenport, & Zeigler, 1980) and (Iman, Helton J., & Campbell, 1981) is utilized. The basic idea of this method is to make sampling point distribution close to probability density function (PDF) by stratification of the input probability distribution. Stratification divides the cumulative probability distribution into equal intervals and then only one sample is randomly taken from each interval or "stratification". This process is schematically shown in Figure 3.14.
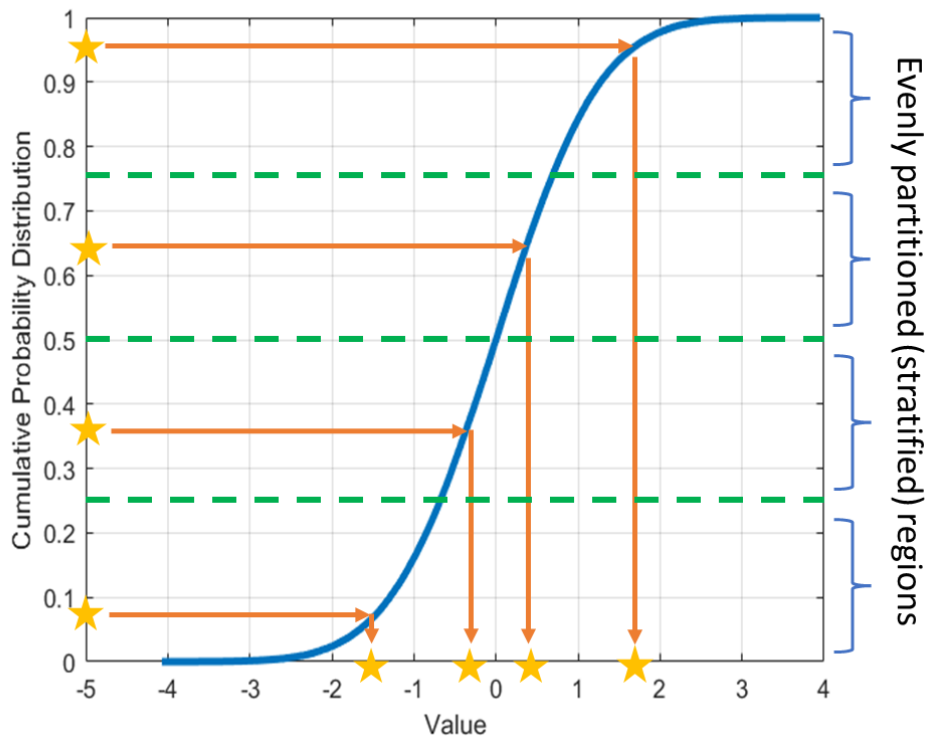
Figure 3.14. Latin Hypercube Sampling Implementation.

As it can be seen from Figure 3.14, there is only sample per stratification for LHS and the samples are more widely distributed (between -2 and 2) when compared to Monte Carlo approach (between -1 and 1) shown in Figure 3.13.

In terms of more than one dimensional space, a square grid containing sample positions is a Latin Square if and only if there is only one sample in each row and column. In this manner, a Latin Hypercube is the generalization of this concept to multi-dimensional space, where each sample is the only one in each axis-aligned hyperplane containing it. For two dimensions, a comparison is provided in Figure 3.15 for LHS and Monte Carlo sampling methodologies.
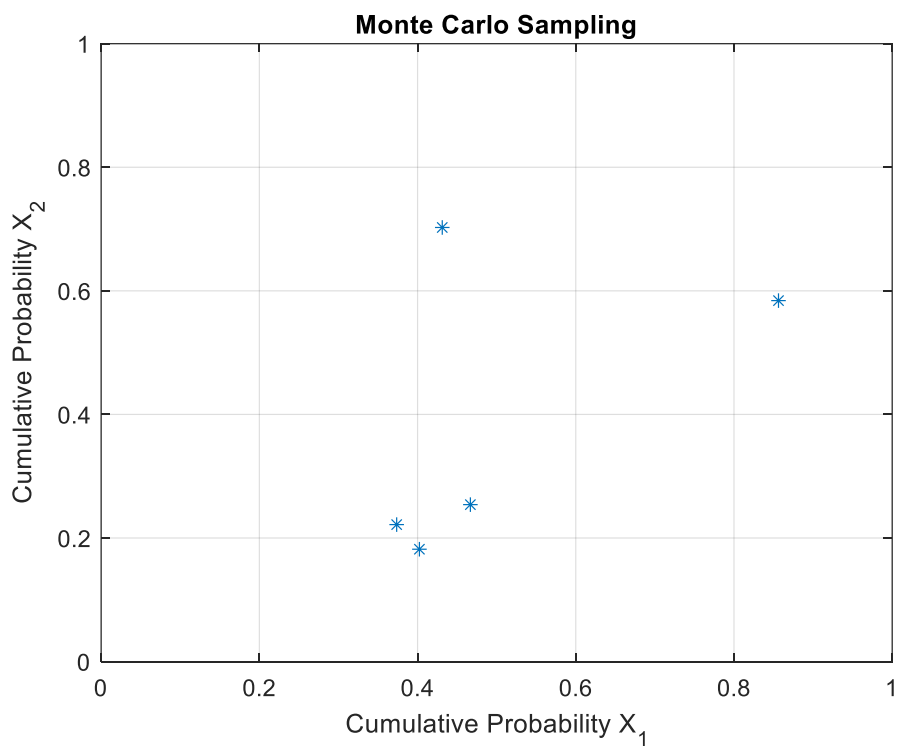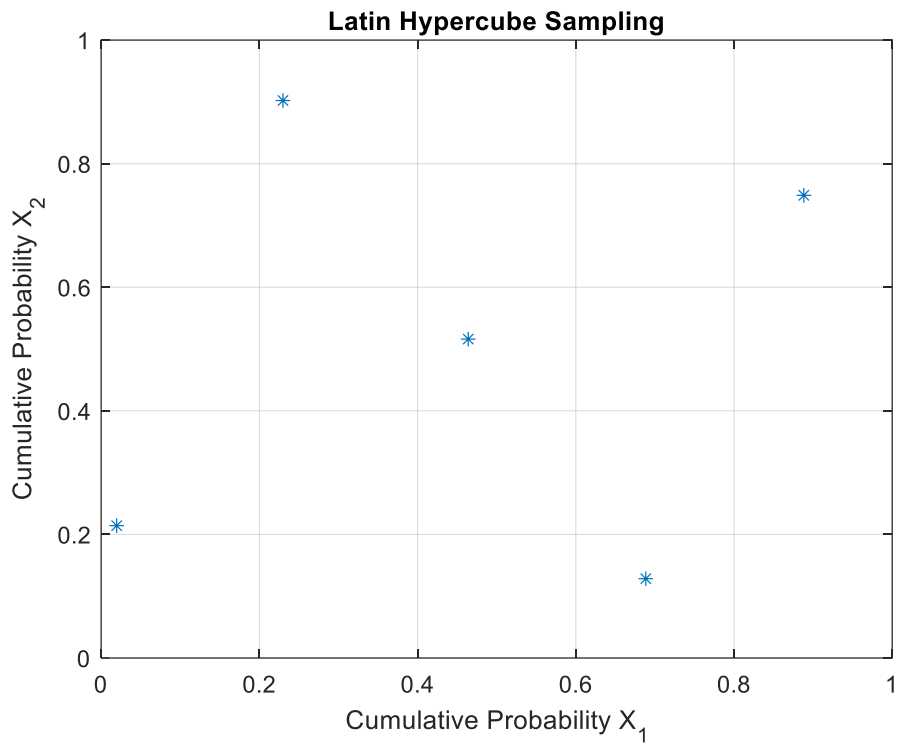
Figure 3.15. LHS and Monte Carlo Sampling Example for Two-Dimensional Space.

As it can be seen from Figure 3.15, there is at least one sample for each grid for the LHS and therefore LHS is more effective in sampling the whole design space when compared to Monte Carlo methodology for same number of samples. In this manner, with the use of LHS, design space can be well represented and explored with a smaller number of runs when compared to a Monte Carlo simulation (Xin, 2015). Similarly, LHS samples can be generated for higher-dimensional space and because of its effectiveness, LHS methodology is preferred for sampling the design space of cluster flying problem.

3.4.2 Finding the Right Sample Size and Optimization

Another key point for design space exploration and optimization is to select the right sample size which would affect the number of feasible solutions over the design space. To find the right number of sample size, several runs can be run and the ratio of feasible solutions for each of the runs divided by the sample size, i.e. # of solutions / sample size, can be checked. Convergence of this ratio indicates that the right sample size is obtained. To illustrate, 15 simulations are run for same problem with 10 spacecraft with 4 design variables (Δe, Δi, $\Delta \Omega$ and $\Delta \omega$) (40 design variables in total) and for each population with sample sizes 250, 500, 750, 1000, 1500, 2000, 2500, 3000, 3500, 4000 and 4500. Then the average number of feasible solutions for each of the runs is divided by the sample size and the result is plotted against sample size in Figure 3.16.
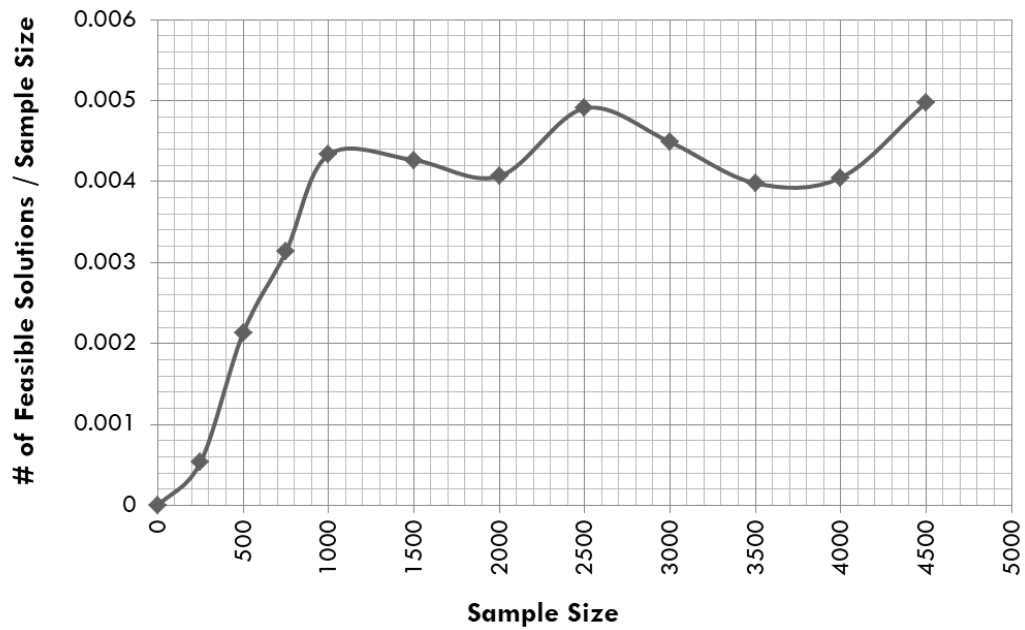
Figure 3.16. Number of Feasible Solutions over Sample Size with respect to Sample Size.

It can be seen in the Figure 3.16 that average number of feasible solutions over sample size converges after 1000 samples for 10 spacecraft configuration which comes with 40 design variables. In this manner, it can be concluded for this example that 25 samples per design variable can be generated using LHS method to find feasible solutions.

After running the simulations for the generated population of 1000 samples, the objective and constraint functions are evaluated and feasible solutions are identified. A sample result and identified feasible solutions are shown in the Figure 3.17.
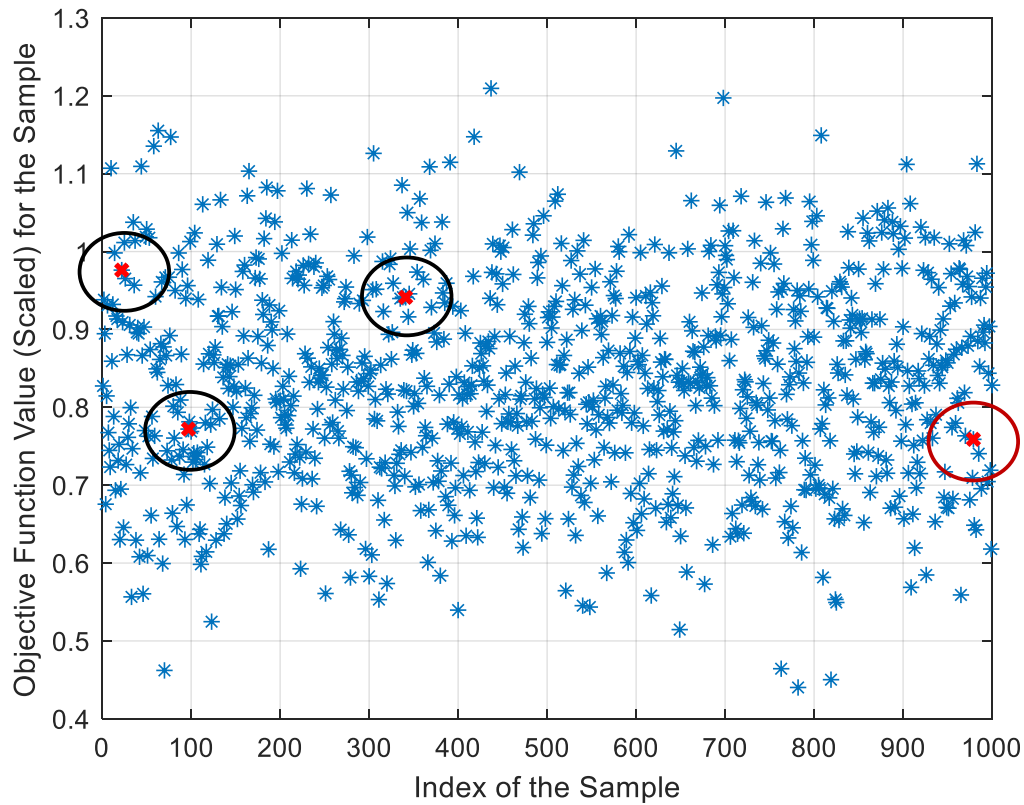
Figure 3.17. Feasible Solutions (red points) from 1000 Samples in the 1st Iteration of Design Space Exploration.

In the Figure 3.17, it can be seen that 4 feasible solutions (circled) are identified. Based on the objective function values of feasible solutions, the design point (red circle) is selected such that the objective function has the minimum value. Then another design space exploration is performed with a population of 1000 samples around the selected design point for further optimization. Here, the new design space is generated such that the design variables vary within the ±20% range of the optimized design point. Similarly, the simulations are run again for the new population and then feasible solutions are filtered. A result for the second iteration of design space exploration is shown in Figure 3.18.
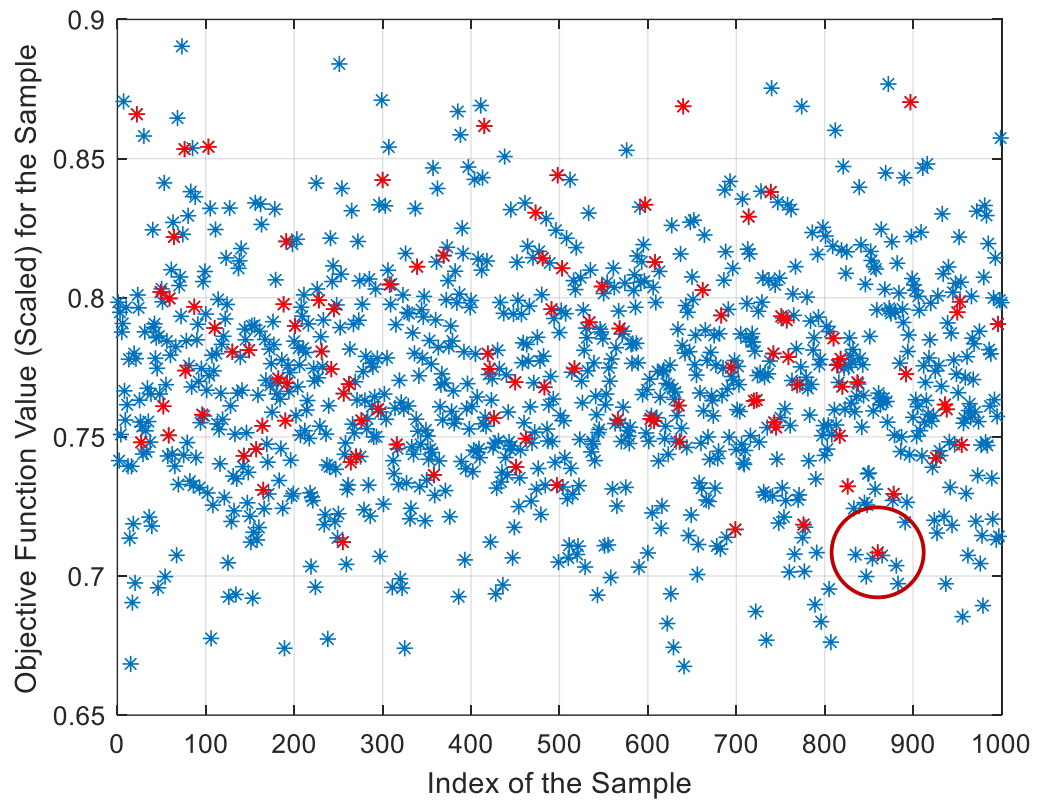
Figure 3.18. Feasible Solutions (red points) from 1000 Samples in the 2nd Iteration of Design Space Exploration.

As it can be seen in the Figure 3.18, there are many feasible solutions (~100s) this time. Here, the sample with minimum objective function value (circled) from the second iteration of the design space exploration can be selected as the final design point. The optimization can be stopped when this final design point improves the objective function value when compared to previous iteration.

CHAPTER 4

CLUSTER FLYING MAXIMIZING STATION KEEPING OBJECTIVE

In this chapter, cluster flying design methodology explained in Chapter 3 is applied for passively safe long-term multi-spacecraft cluster flying design maximizing station-keeping objective. In this approach, design variables are selected as relative mean orbital elements for each spacecraft. These relative orbital elements which are derived from a reference TLE are propagated through SGP4 propagator with no uncertainty as described in Figure 3.3. In addition, the objective function is specified as defined by Eq. (62) and constraints are specified as defined by Eq. (59) and Eq. (61). In addition to these objectives and constraints, the problem can be formulated as a multi-objective optimization problem considering the validity duration and spacecraft number in the cluster. As it can be predicted that increasing the number of spacecraft would increase the necessary distances and therefore the total cost of the objective function. In addition, long duration and more spacecraft configurations would yield less solutions than the cases with short duration and less spacecraft. In order to demonstrate such situations and the effectiveness of the methodology, a problem whose assumptions and parameters are summarized in Table 4.1 is set.

Table 4.1 Cluster Flying Design Formulation with Station-Keeping Objective

Parameter	*Specification*
Objective Function	$Minimize \displaystyle\sum_{l=1}^{N} \sum_{j=1}^{T} \frac{\left(\Delta R_{l,j}^2 + \Delta T_{l,j}^2 + \Delta N_{l,j}^2\right)}{d_{max}^2}$
Constraint Function(s)	Eq. (59)
Bounds on Design Variables	Eq. (65)
Propagator	Analytical (SGP4)

Inputs and Assumptions	Reference Orbit	SSO, LTDN 10:30 at 685 km altitude
	Spacecraft Number	3, 4, 6, 8 and 10
	d_{min} in RN Plane	0.1 km
	d_{max} in RTN Plane	50 km
	Δa Difference	0 km
	Physical Differences	Defined by $\Delta\beta_l^* = 0$
	Duration, T_{max}	1, 3, 5, 7 and 10 days
	Step Size	10 sec
	Sample Number	2000

In this problem, the objective function given in Eq. (62) is scaled with the d_{max}. As for the mission parameters, a Sun-Synchronous LTDN 10:30 orbit at 685 km is specified. Also, spacecraft numbers are varied from 3 to 10 and simulation duration is varied from 1 to 10 days. The physical differences through drag parameters, $\Delta\beta_l^*$, are not introduced at this stage in order to demonstrate the effect of only spacecraft number and validity duration. While minimum and maximum distance constraints are set as 0.1 km and 50 km respectively, the semimajor axis difference, Δa, is set to 0 in order to cancel the gradual increase of along-track separation. Finally, sample number is chosen as 2000 to have a good representation of design space and generate several solutions for comparison. Some sample results of an optimized solution for 5-spacecraft cluster and 5 day-duration are shown in Figure 4.1 and Figure 4.2.
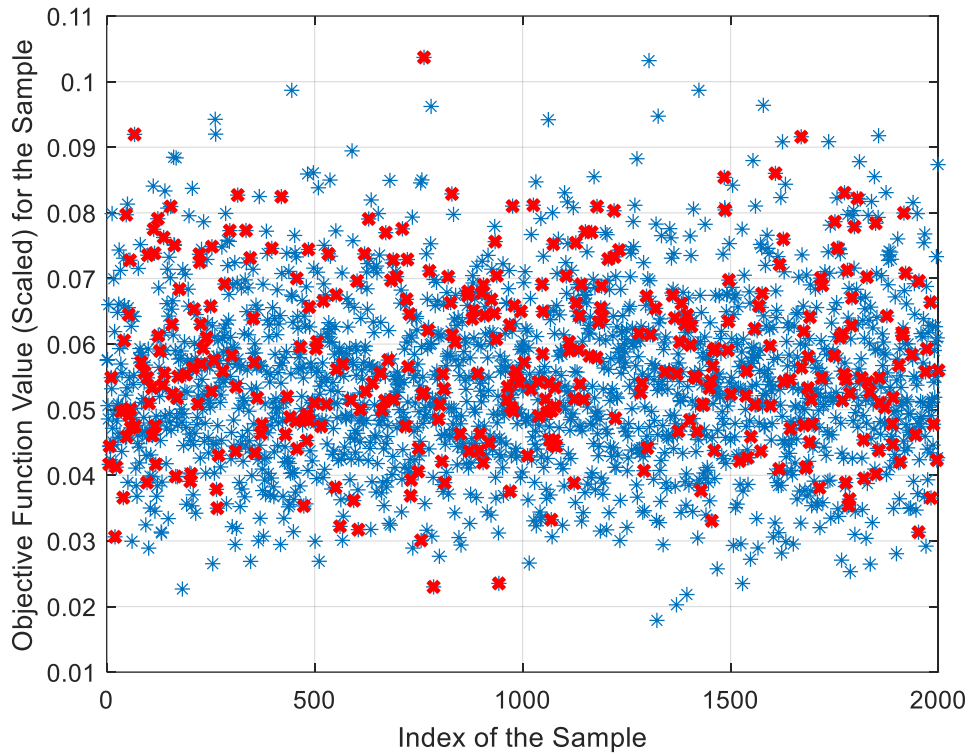
Figure 4.1. Feasible Solutions (red points) from 2000 Samples for 5-Spacecraft Cluster and 5 Day-Duration.

Figure 4.1, it can be seen that plenty of feasible solutions (red points) are found. Here, there are 356 feasible solutions which is 18% of 2000 samples. Based on the objective function values of feasible solutions, the design point is selected such that the objective function has the minimum value of 0.023. The resulting relative distances for $C_2^5 = 10$ combinations are shown in Figure 4.2. In the figure, each discrete time interval, for example 0 to 1, 1 to 2, etc. until 9 to 10, corresponds to 5-day simulation result for each combination of Spacecraft 1 and 2, Spacecraft 1 and 3, etc. until 10th combination of Spacecraft 4 and 5.
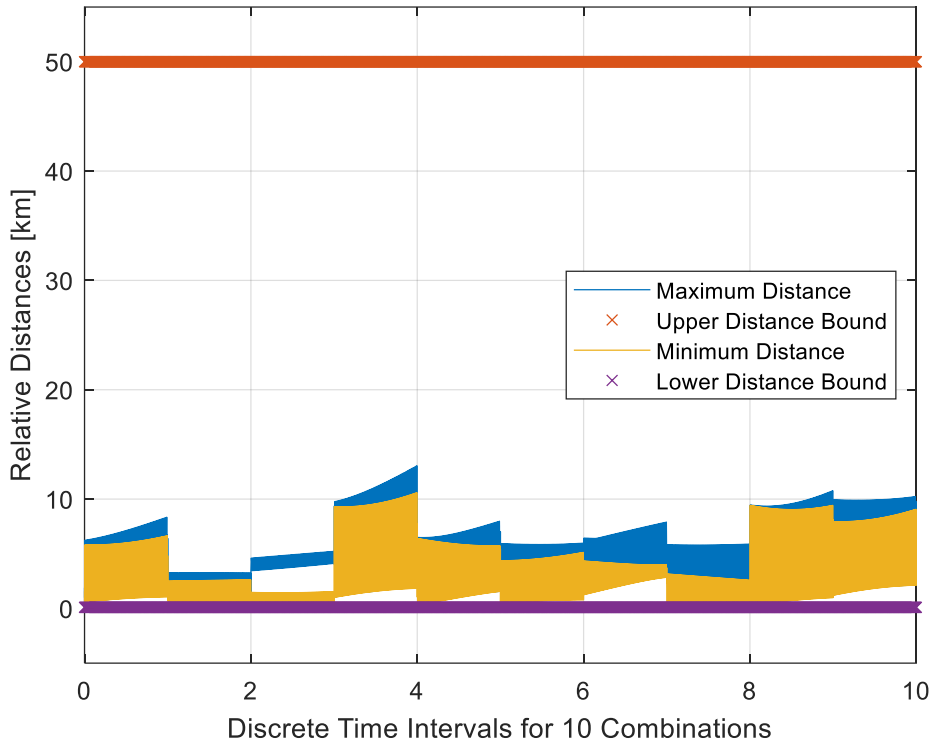
Figure 4.2. Cluster Flying 5 Day-Result for 5 Spacecraft with Station-Keeping Objective.

From Figure 4.2, it may be concluded that the 5-spacecraft cluster flying design does not violate the minimum and maximum distance constraints of 0.1 km and 50 km respectively over 5-day period. The minimum distance in RN occurs as 112.7 m. and maximum distance occurs as 13.1 km. in the cluster. In addition to relative distance plots, the relative motion of spacecraft in Radial, Along-Track and Cross-Track (RTN) are shown in Figure 4.3, Figure 4.4, Figure 4.5 and Figure 4.6. In the plots, '*' sign marks the initial condition, T_0, and 'o' sign marks the final condition, T_f.
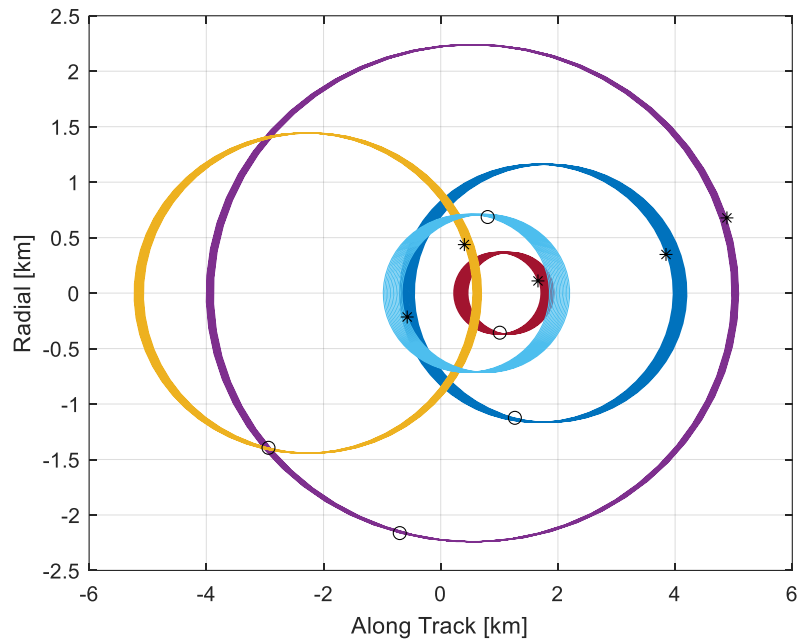
Figure 4.3. Along-Track - Radial Distances of 5 Day-Result for 5 Spacecraft Cluster with Station-Keeping Objective.

The Along-Track – Radial plot for 5-spacecraft cluster shows that there is a radial separation between the spacecraft when along-track distance disappears. As the biggest uncertainty occurs in along-track direction, this provides an inherent safety for the cluster. Although the plot shows 5-day trajectories, there are regions where the red, blue, dark blue or yellow relative orbits may still intersect when along-track separation begins diminishing. In this case, it can be seen in Figure 4.4 that there is always a distance in cross-track between these relative orbits. In this way, a separation either in radial or cross rack direction is always ensured within the cluster.
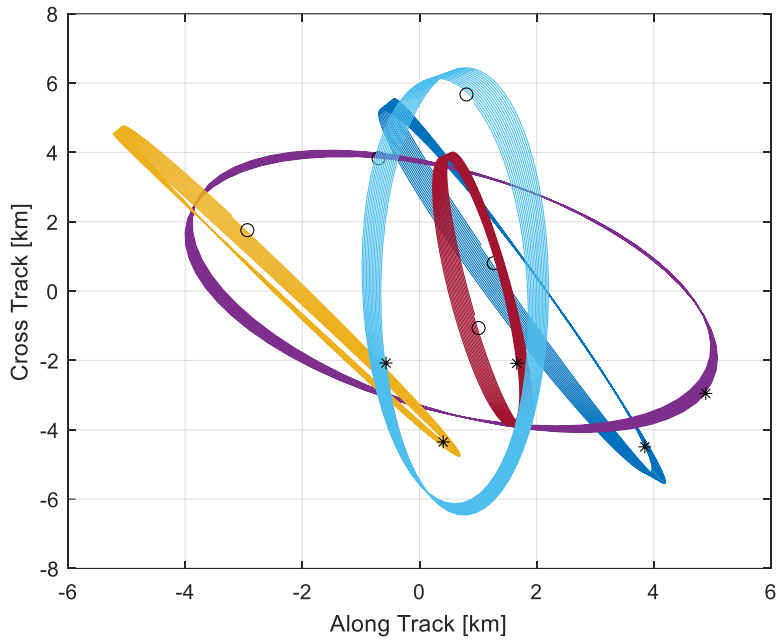
Figure 4.4. Along-Track – Cross-Track Distances of 5 Day-Result for 5 Spacecraft Cluster with Station-Keeping Objective.
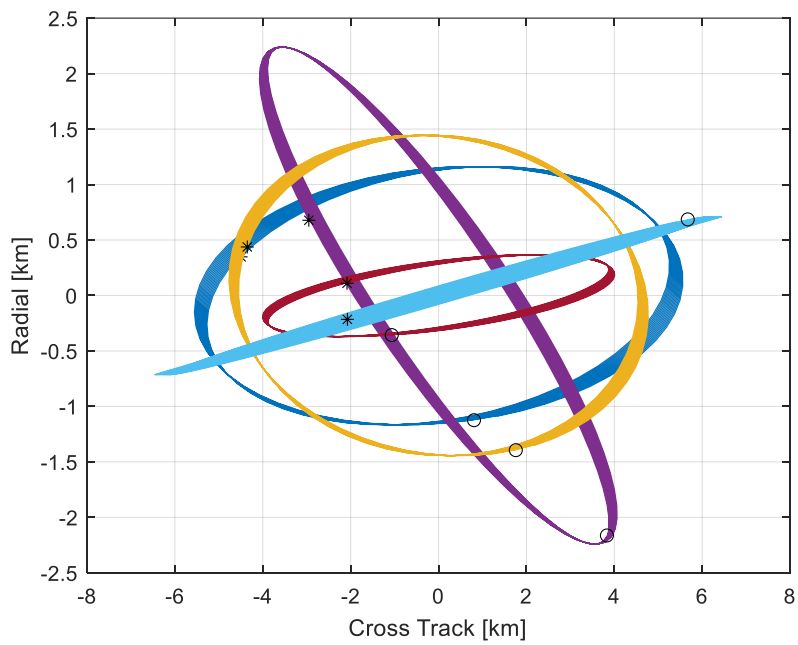
Figure 4.5. Cross-Track - Radial Distances of 5 Day-Result for 5 Spacecraft Cluster with Station-Keeping Objective.
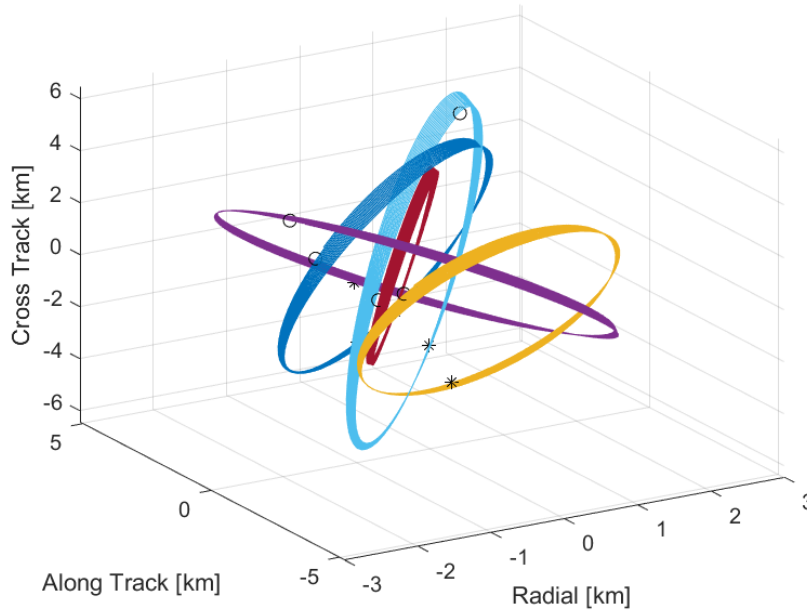
Figure 4.6. Radial – Along-Track – Cross-Track Distances of 5 Day-Result for 5 Spacecraft Cluster with Station-Keeping Objective.

Finally, the boundaries are realized within a 5 x 10 x 12 km^3 volume for 5-spacecraft 5-day duration cluster. In this case, theoretical maximum distance would be around 16 km. where realized maximum distance of 13.1 km. between spacecraft is reasonable. In order to see the effects of increased number of spacecraft and duration, the results of another optimized solution for 10-spacecraft cluster and 10 day-duration are shown in Figure 4.7 and Figure 4.8. In this case, 4000 samples are used since there was no feasible solution found for 2000 samples.
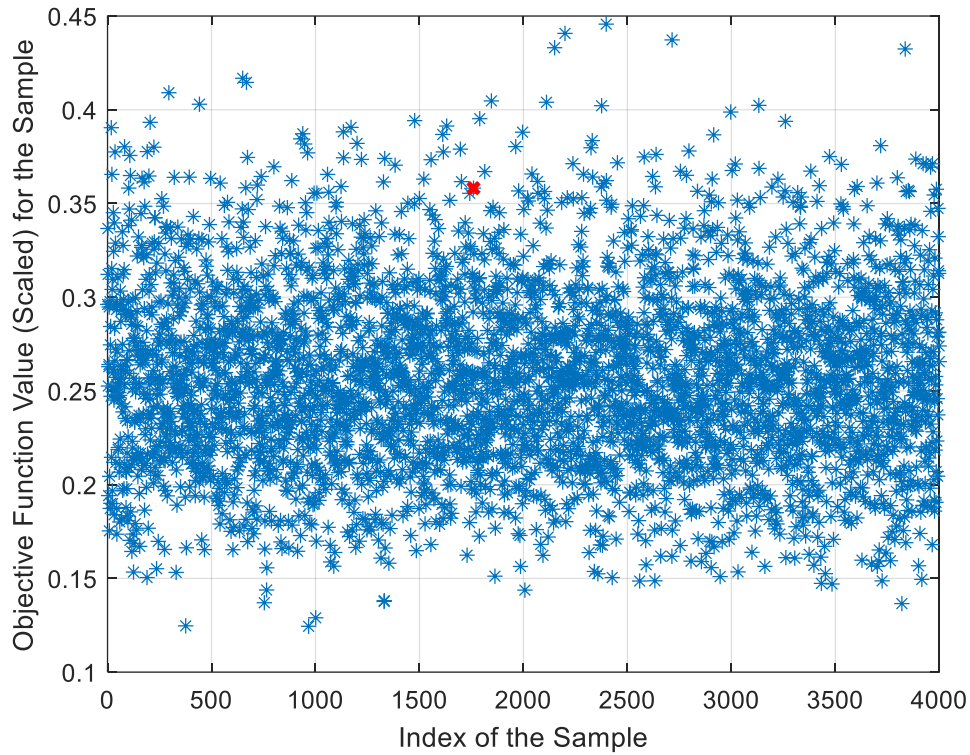
Figure 4.7. Feasible Solutions (red points) from 4000 Samples for 10-Spacecraft Cluster and 10 Day-Duration.

From Figure 4.7, it can be seen that only one solution (red point) is found which is 0.025% of 4000 samples. For this design point, the objective function has the value of 0.358. The resulting relative distances for $C_2^{10} = 45$ combinations are shown in Figure 4.8. In the figure, each discrete time interval, for example 0 to 1, 1 to 2, etc. until 44 to 45 corresponds to 10-day simulation result for each combination of Spacecraft 1 and 2, Spacecraft 1 and 3, etc. until 45th combination of Spacecraft 9 and 10.
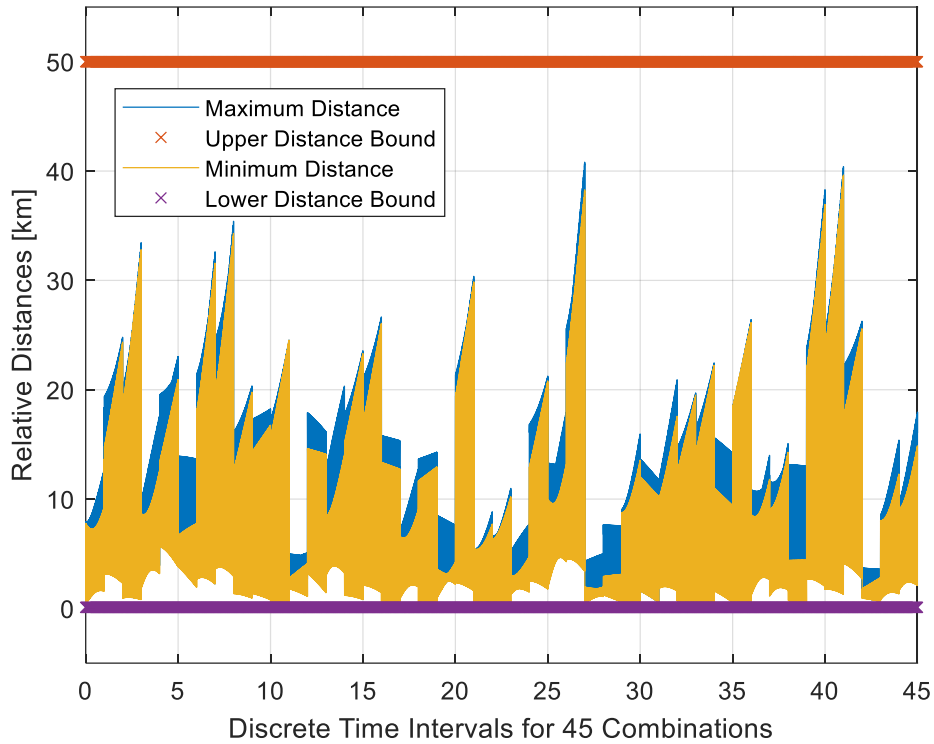
Figure 4.8. Cluster Flying 10 Day-Result for 10 Spacecraft with Station-Keeping Objective.

From Figure 4.8, it can be concluded that the 10-spacecraft cluster flying design does not violate the minimum and maximum distance constraints of 0.1 km and 50 km respectively over 10-day period. The minimum distance in RN occurs as 101 m. and maximum distance occurs as 40.8 km. in the cluster. In addition to relative distances, the relative motion of spacecraft in Radial, Along-Track and Cross-Track (RTN) are shown in Figure 4.9, Figure 4.10, Figure 4.11 and Figure 4.12. In the plots, '*' sign marks the initial condition, T_0, and 'o' sign marks the final condition, T_f.

Figure 4.9. Along-Track - Radial Distances of 10 Day-Result for 10 Spacecraft Cluster with Station-Keeping Objective.
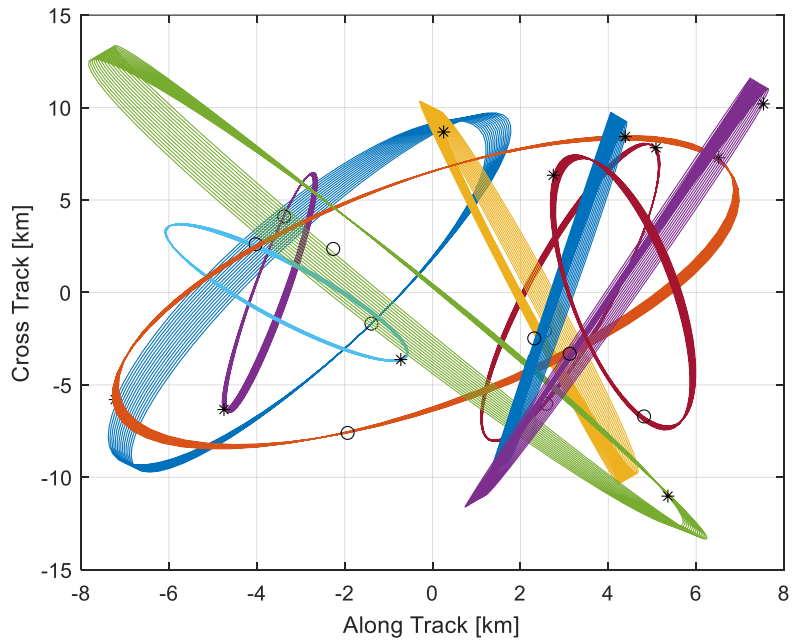
Figure 4.10. Along-Track – Cross-Track Distances of 10 Day-Result for 10 Spacecraft Cluster with Station-Keeping Objective.
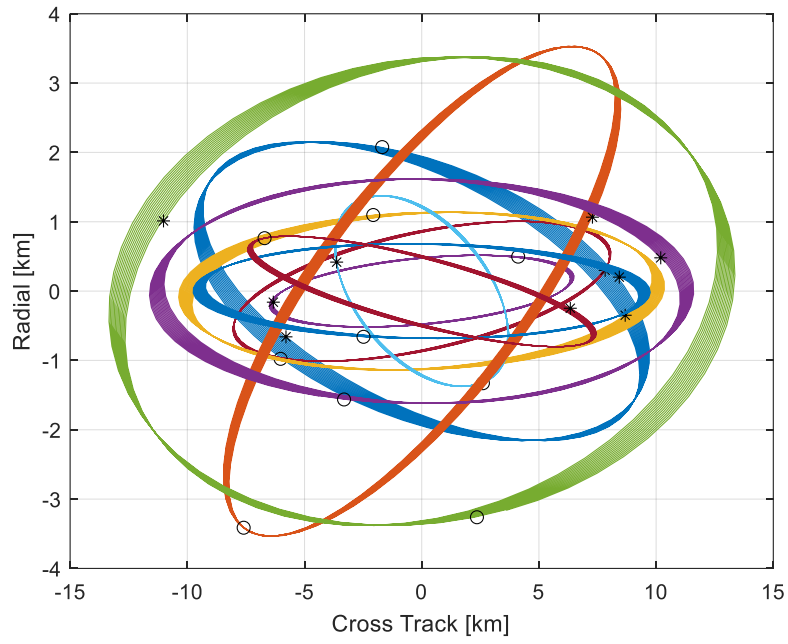
Figure 4.11. Cross-Track - Radial Distances of 10 Day-Result for 10 Spacecraft Cluster with Station-Keeping Objective.
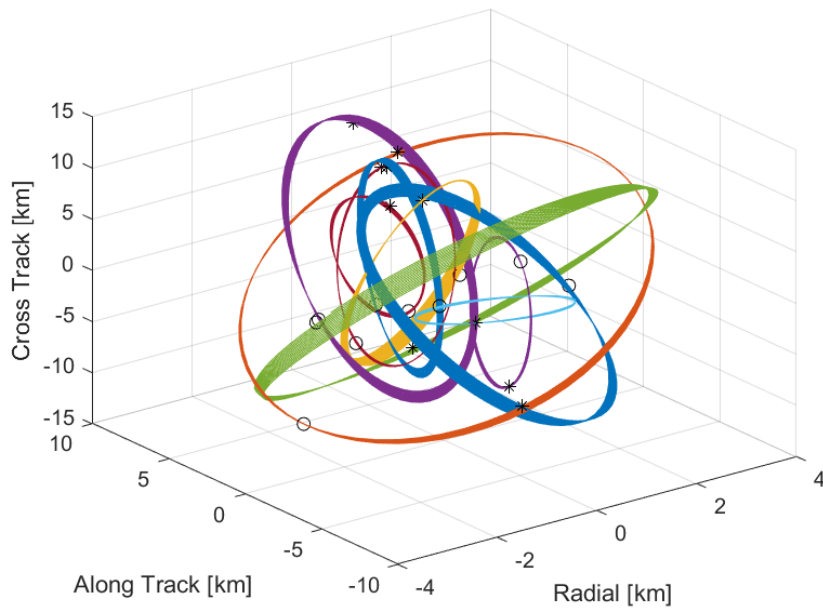
Figure 4.12. Radial – Along-Track – Cross-Track Distances of 10 Day-Result for 10 Spacecraft Cluster with Station-Keeping Objective.

Similar to the previous example of 5 spacecraft cluster, a separation either in radial or cross rack direction is always ensured when along-track distance diminishes within the cluster providing an inherent safety. From Figure 4.9 and Figure 4.10, it can be also deduced that specific orientations of eccentricity and inclination vectors result in two 5-spacecraft groups within 10-spacecraft cluster separated by an along-track offset. Although the gradual separation of along-track is canceled via $\Delta a = 0$, an increase in maximum distances is still observed in Figure 4.8. In this case, a control for along-track separation may be necessary to maintain the cluster.

To understand how difficult is to obtain a solution, percentage of solutions with respect to problem variables such as number of spacecraft, N, and duration, T_{max}, are plotted in Figure 4.13 and Figure 4.14 for the problem defined in Table 4.1. Here, as the objectives for the number of solutions as well as spacecraft number and duration are to be maximized, all values for these variables are plotted as positive.
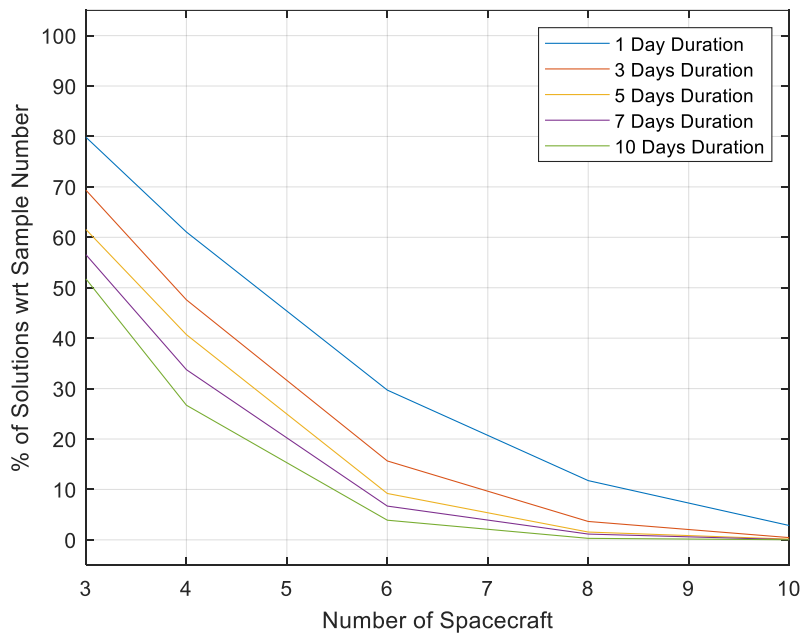
Figure 4.13. Spacecraft Number, N vs. Percentage of Number of Solutions for fixed Duration, T_{max}.
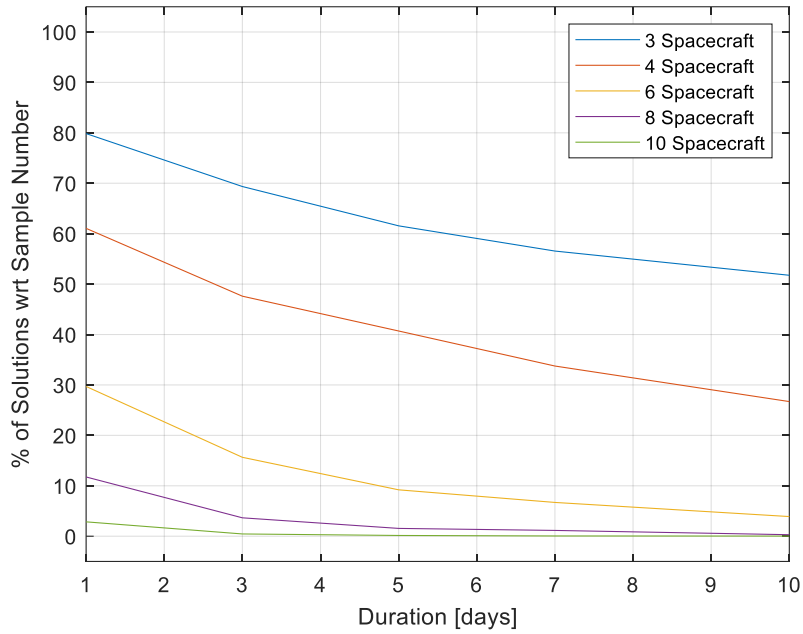
Figure 4.14. Duration, T_{max} vs. Percentage of Number of Solutions for fixed Spacecraft Number, N.

As it can be seen from the Figure 4.13 and Figure 4.14 that there is exponentially decrease in number of solutions if the cluster flying duration and the number of spacecraft in the cluster are increased. It is also seen that it is more likely to find solutions and optimize for clusters with 3 to 6 spacecraft.

To demonstrate the multi-objective behavior of the problem, several results are also obtained for the objective function value with respect to problem variables of spacecraft number, N, and duration, T_{max}. The results are plotted in Figure 4.15 and Figure 4.16. In this case, as the objective functions are minimized, the spacecraft number and duration are plotted as negative values.
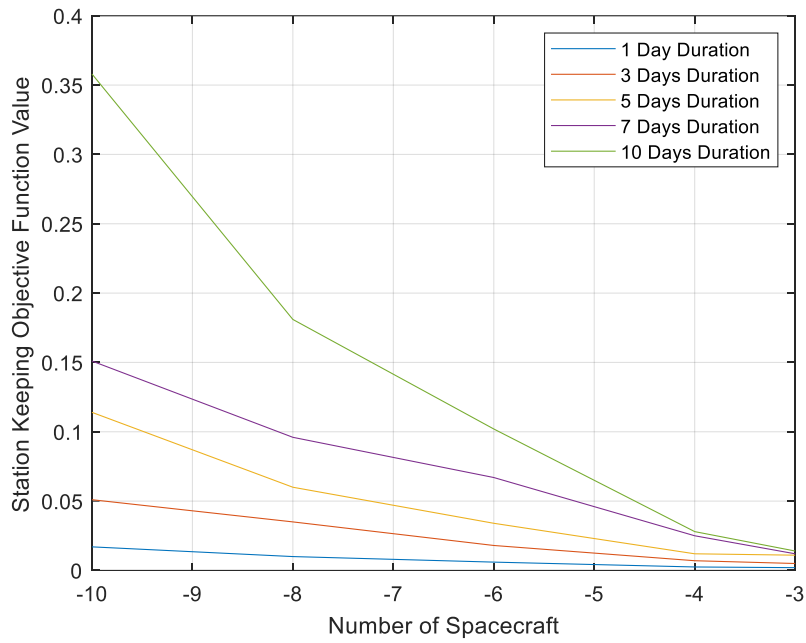
Figure 4.15. Spacecraft Number, N vs. Objective Function Value for fixed Duration, T_{max}.
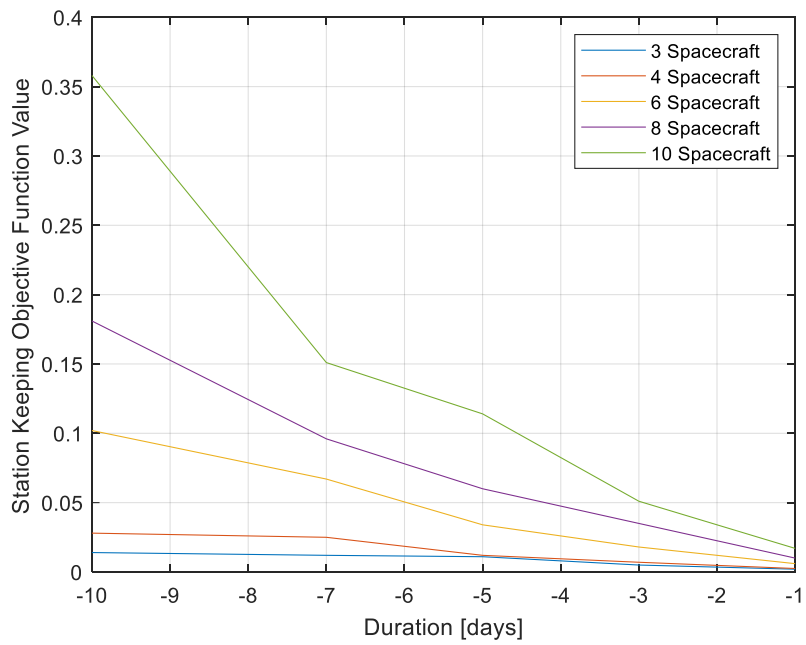
Figure 4.16. Duration, T_{max} vs. Objective Function Value for fixed Spacecraft Number, N.

From Figure 4.15 and Figure 4.16, it can be seen that increasing cluster keeping duration requirement and number of spacecraft in the cluster increases the objective function value. This is due to the fact that the clusters' volume needs to be increased for more spacecraft and longer duration. It is also seen that pareto front curves can be obtained for conflicting objectives against number of spacecraft or duration.

As mentioned previously, one of the main motivations for the developed cluster flying design methodology is to analyze the time validity of clusters. For identifying time bounds, the cluster can be propagated further and minimum distances can be checked. Here, a sample problem of 5 spacecraft cluster is designed for 15 days and propagated for 20 days. From 16 feasible solutions which is 0.8% of 2000 samples, the design point is selected such that the objective function has the minimum value of 0.239. Resulting relative distances plot is shown in Figure 4.17.
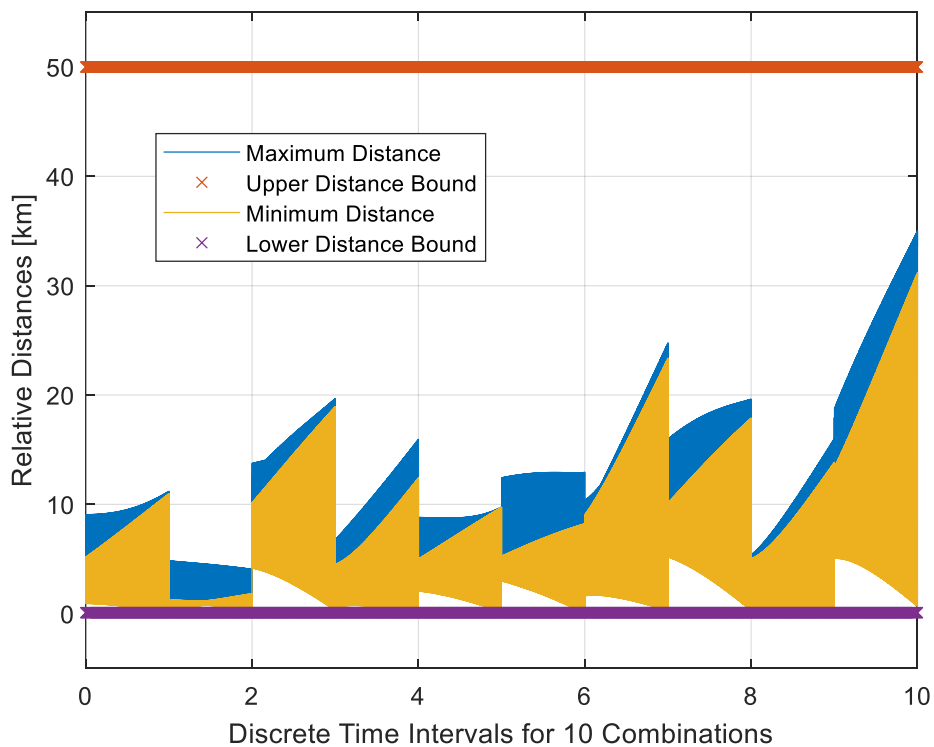
Figure 4.17. 20 Day Propagation Result for 15-day 5 Spacecraft Cluster Flying with Station-Keeping Objective.

When compared to results in Figure 4.1 and Figure 4.2, there is a dramatic decrease in solution number (18% to 0.8%) and the cluster expands where boundaries are realized within a 7.1 x 20 x 16 km^3 volume. Here, minimum distance in RN becomes 76 m. after 19.8 days propagation where the distance in RTN is 543 m. Also, minimum distance in RTN occurs as 253 m. where the distance in RN is 119 m. The maximum distance is around 35 km. From these results, it can be deduced that in some instances, 5 spacecraft clusters may be flown for up to 20 days without violating constraints for the problem in Table 4.1. Similarly, based on reference orbit and constraint definitions, several configurations and their validities can be found.

Finally, it is also possible to incorporate physical differences for simulating heterogeneous system by introducing differences in drag parameters $\Delta\beta_l^*$. In this case, the problem defined in Table 4.1 is re-written in Table 4.2.

Table 4.2 Cluster Flying Design Formulation for Heterogeneous Systems

Parameter	*Specification*	
Objective Function	$Minimize \sum_{l=1}^{N} \sum_{j=1}^{T} \dfrac{\left(\Delta R_{l,j}^2 + \Delta T_{l,j}^2 + \Delta N_{l,j}^2\right)}{d_{max}^2}$	
Constraint Function(s)	Eq. (59)	
Bounds on Design Variables	Eq. (65)	
Propagator	Analytical (SGP4)	
Inputs and Assumptions	Reference Orbit	SSO, LTDN 10:30 at 685 km altitude
	Spacecraft Number	5
	d_{min} in RN Plane	0.1 km
	d_{max} in RTN Plane	50 km
	Physical Differences (Defined by $\Delta\beta_l^*$)	$-0.5 \times \beta_{ref}^* < \Delta\beta_l^* < 0.5 \times \beta_{ref}^*$
	Simulation Duration	20 days
	Step Size	10 sec

In this problem, physical differences are introduced through drag parameters $\Delta\beta_l^*$ and the duration is specified as 20 days as a continuation of the previous problem of 5-spacecraft 20-day homogeneous cluster. The results of the feasible solutions for 5-spacecraft heterogeneous cluster and 20 day-duration are shown in Figure 4.18 and Figure 4.19.
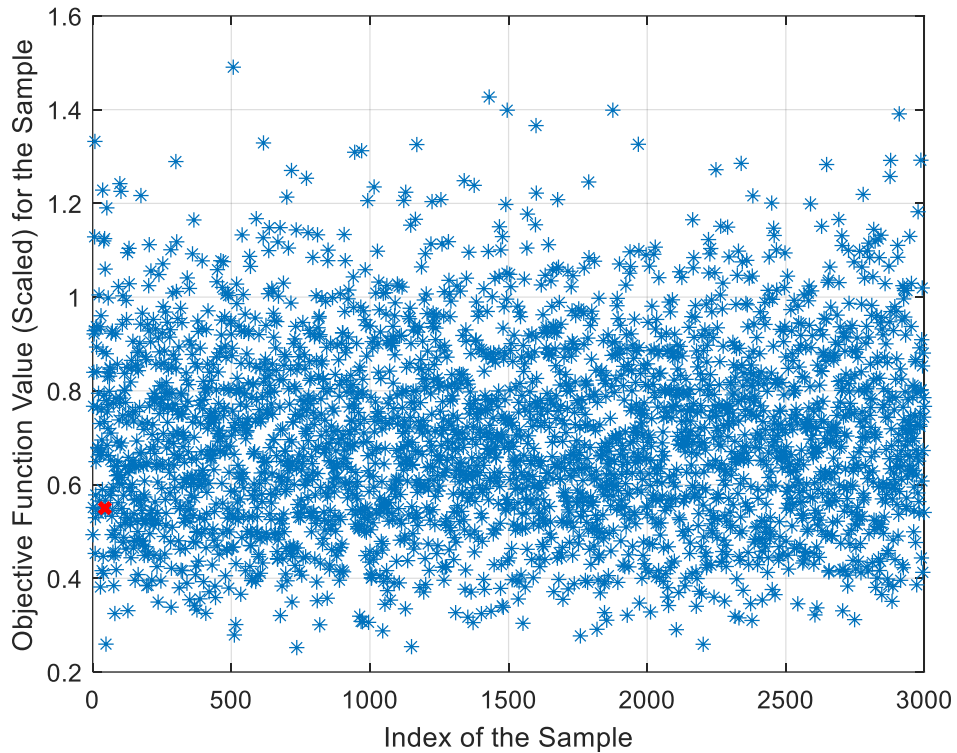
Figure 4.18. Feasible Solutions (red points) from 3000 Samples for 5-Spacecraft Heterogeneous Cluster and 20 Day-Duration.

In Figure 4.18, it can be seen that only 1 solution (red point), which is 0.03% of 3000 samples, is found. When compared to the case in Figure 4.17, there is dramatic decrease in solution number (0.8% to 0.03%) and the objective function value is doubled from 0.239 to 0.550. The resulting relative distances for $C_2^5 = 10$ combinations are shown in Figure 4.19. In the figure, each discrete time interval, for example 0 to 1, 1 to 2, etc. until 9 to 10, corresponds to 30-day simulation result for each combination.
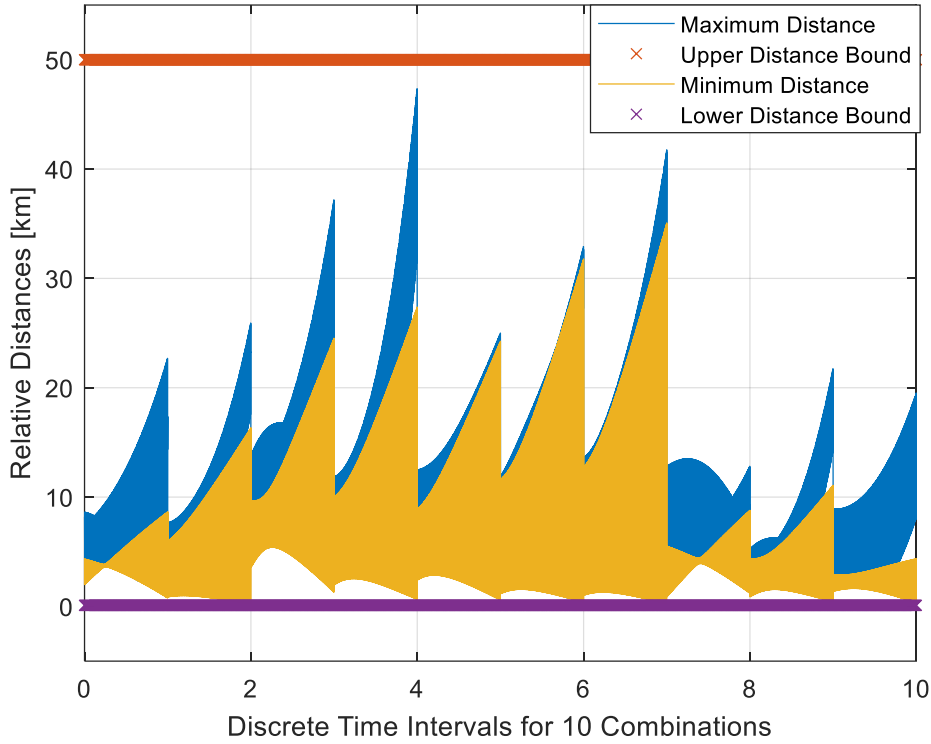
Figure 4.19. Cluster Flying 20 Day-Result for 5 Spacecraft Heterogeneous System with Station-Keeping Objective.

From Figure 4.19, it can be concluded that the 5-spacecraft cluster flying design for heterogeneous system does not violate the minimum and maximum distance constraints of 0.1 km and 50 km respectively over 20-day period. The minimum distance in RN occurs as 211.2 m. and maximum distance occurs as 47.3 km. in the cluster. In addition, the minimum distance in RTN occurs as 797.3 m. where the distance in RN is 792.7 m. In this way, it can be guaranteed that there is always a separation in RN when along-track distances are the lowest. Also, there is an exponential increase in along-track separation between the spacecraft due to differential drag effects caused by $\Delta \beta_i^*$. In order to maintain the cluster flying, along-track separation due to differential drag needs to be compensated.

In addition to relative distance plots, the relative motion of spacecraft in Radial, Along-Track and Cross-Track (RTN) are shown in Figure 4.20, Figure 4.21, Figure

4.22 and Figure 4.23. In the plots, '*' sign marks the initial condition, T_0, and 'o' sign marks the final condition, T_f.
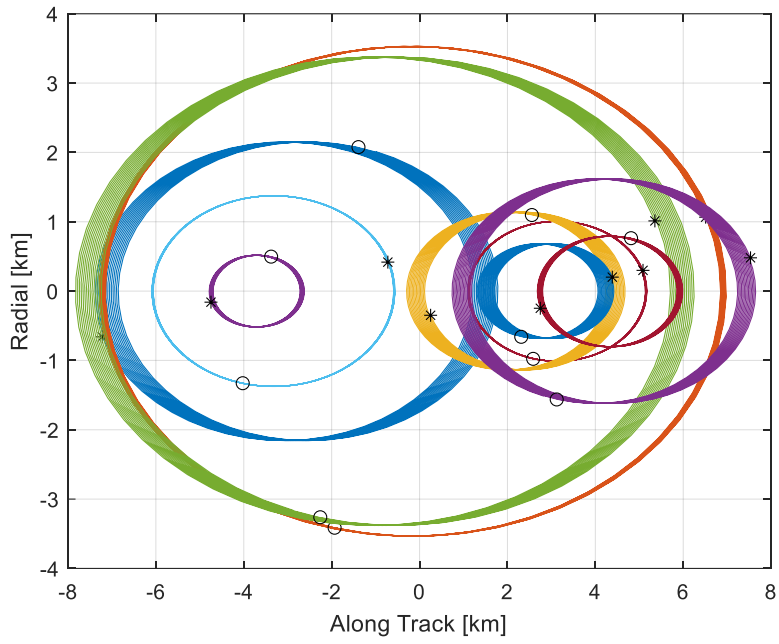

Figure 4.20. Along-Track - Radial Distances of 5 Day-Result for 5 Spacecraft Heterogeneous Cluster with Station-Keeping Objective.

The Along-Track – Radial plot for 5-spacecraft heterogeneous cluster shows that there is a radial separation between the spacecraft when along-track distance disappears. As the biggest uncertainty occurs in along-track direction, this provides an inherent safety for the cluster. Although the plot shows 20-day trajectories, there are regions where some relative orbits can intersect in along-track direction. In this case, it can be seen in Figure 4.21 and Figure 4.22 that there is always a distance in cross-track direction between these relative orbits when radial distance diminish or radial distance when cross-track distance diminish. In this way, a separation either in radial or cross rack direction is always ensured within the cluster.

Figure 4.21. Along-Track – Cross-Track Distances of 5 Day-Result for 5 Spacecraft Heterogeneous Cluster with Station-Keeping Objective.
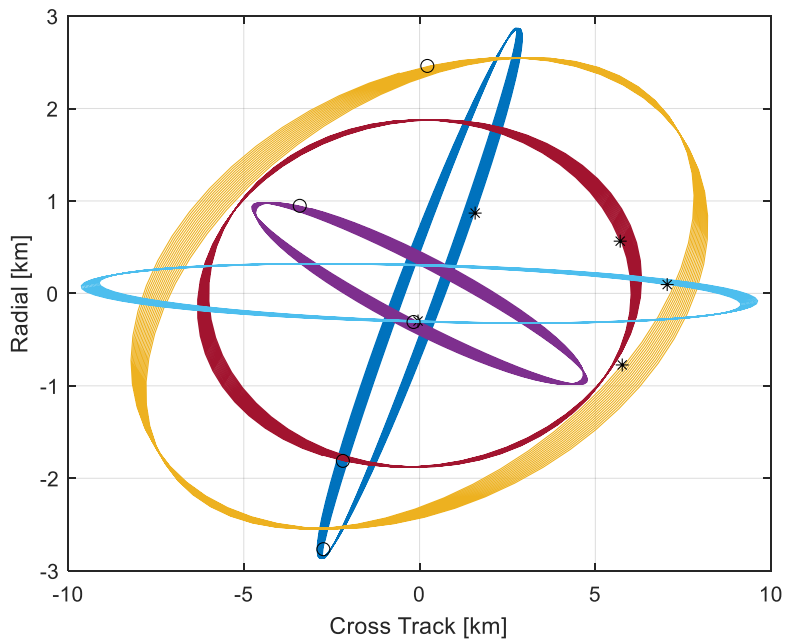
Figure 4.22. Cross-Track - Radial Distances of 5 Day-Result for 5 Spacecraft Heterogeneous Cluster with Station-Keeping Objective.
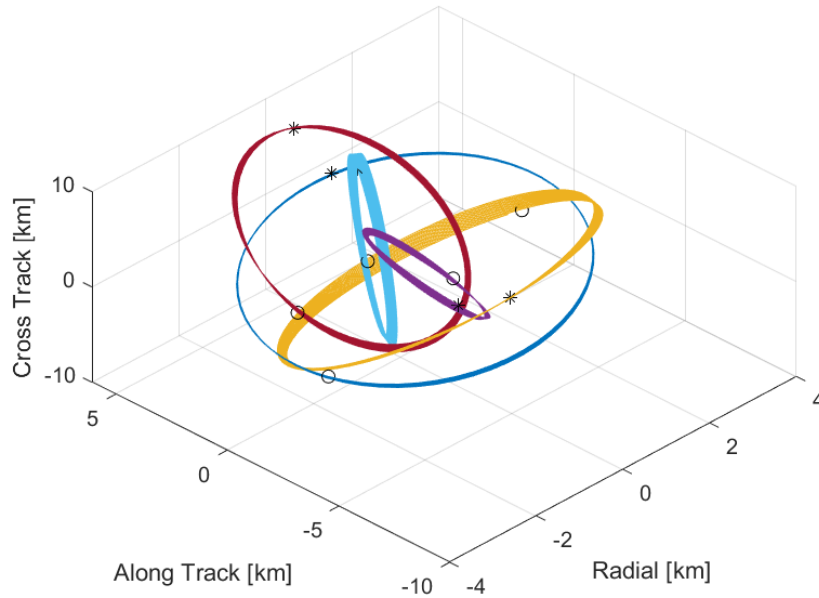
Figure 4.23. Radial – Along-Track – Cross-Track Distances of 5 Day-Result for 5 Spacecraft Heterogeneous Cluster with Station-Keeping Objective.

Finally, the boundaries are realized within a 6 x 14 x 20 km^3 volume for 5-spacecraft 20-day duration heterogeneous cluster. Finally, when solutions for 5-spacecraft cluster with various duration and homogeneity are compared, it is observed that the percentage of feasible solutions dramatically decrease from short duration to long duration and from homogeneous system to heterogeneous system. Also, the objective function value for station-keeping increases from short duration to long duration as well as from homogeneous system to heterogeneous system.

For LEO missions, as it is the case studied in this chapter, the requirement for a long-term cluster configuration would be to minimize the differential drag since this would lead to a fast along-track separation between the spacecraft. In the heterogeneous system case, the differential drag is inevitable in the existence of different drag parameters. However, the cluster configurations found with the developed methodology provide the right initial conditions that adjust the drift over

a specific time interval in the existence of relative drag. With this, it is also possible to determine the time validity of a given heterogeneous cluster configuration with different number of spacecraft, distance bounds and spacecraft parameters.

With the methodology whose performance is discussed in this chapter can be used to define general boundaries of a homogeneous and heterogeneous clusters and their time validity (until control actions are necessary) with relatively moderate fidelity. This method requires low computational demand therefore becomes ideal for a general mission design, analysis and/or assessment of spacecraft clusters. It takes less than 5 minutes to find an optimal solution for a 2-day duration 10-spacecraft configuration.

CHAPTER 5

CLUSTER FLYING MAXIMIZING SAFETY OBJECTIVE

In this chapter, cluster flying design methodology explained in Chapter 3 is applied for passively safe long-term multi-spacecraft cluster flying design maximizing safety objective. In this approach, design variables are selected as relative osculating orbital elements for each spacecraft. These relative orbital elements which are derived from a reference state vector are propagated through high precision orbit propagator with uncertainty as described in Figure 3.2. In addition, the objective function is specified as defined by Eq. (63) and constraints are specified as defined by Eq. (59) and Eq. (61). In order to demonstrate the effectiveness of the methodology, a problem whose assumptions and parameters are summarized in Table 5.1 is set.

Table 5.1 Cluster Flying Design Formulation with Safety Objective

Parameter	*Specification*	
Objective Function	Minimize Eq. (63)	
Constraint Function(s)	Eq. (59)	
Bounds on Design Variables	Eq. (65)	
Propagator	Numerical with uncertainty propagation	
Inputs and Assumptions	Reference Orbit	SSO, LTDN 10:30 at 685 km altitude
	Spacecraft Number	5
	d_{min} in RN Plane	0.1 km
	d_{max} in RTN Plane	50 km
	Δa Difference	0 km

Physical Differences	Defined by $m_l, A_{d,l}, C_{d,l}, A_{r,l}, C_{r,l}$ ($-0.5 \times \beta_{ref} < \Delta\beta_l < 0.5 \times \beta_{ref}$)
Radius of Conjunction Area, R_c	20 m
Initial Position Covariance (3σ) in RTN (m²)	$P_{RTN,R0} = diag[3.6^2, 22^2, 2^2]$
Initial Velocity Covariance (3σ) in RTN (m/sec)	$P_{RTN,V0} = diag[0.02^2, 0.004^2, 0.003^2]$
Covariance Update	Every 12 Hours
Duration, T_{max}	3 days
Step Size	10 sec

This scenario reflects the assumptions for a ground based operational analysis with a 12-hour communication outage. This represents the perspective of an analysis engineer to forecast and identify any collision risks over the next 12 hours. Therefore, the initial covariance is updated every 12 hours to represent a realistic scenario of receiving the most recent orbit determination solution with this period for a LEO mission. In this manner, initial covariance values are assumed such that a GNSS receiver with moderate accuracy, for instance a small satellite GNSS receiver, is utilized.

For this scenario, the feasible design solution for 5 spacecraft is simulated for 3 days and the distances between any two spacecraft during each time instant for 10 combinations is shown in the Figure 5.1. In the figure, each discrete time interval, for example 0 to 1, 1 to 2, etc. until 9 to 10 corresponds to 3-day simulation result for each combination of Spacecraft 1 and 2, Spacecraft 1 and 3, etc. until 10th combination of Spacecraft 4 and 5.
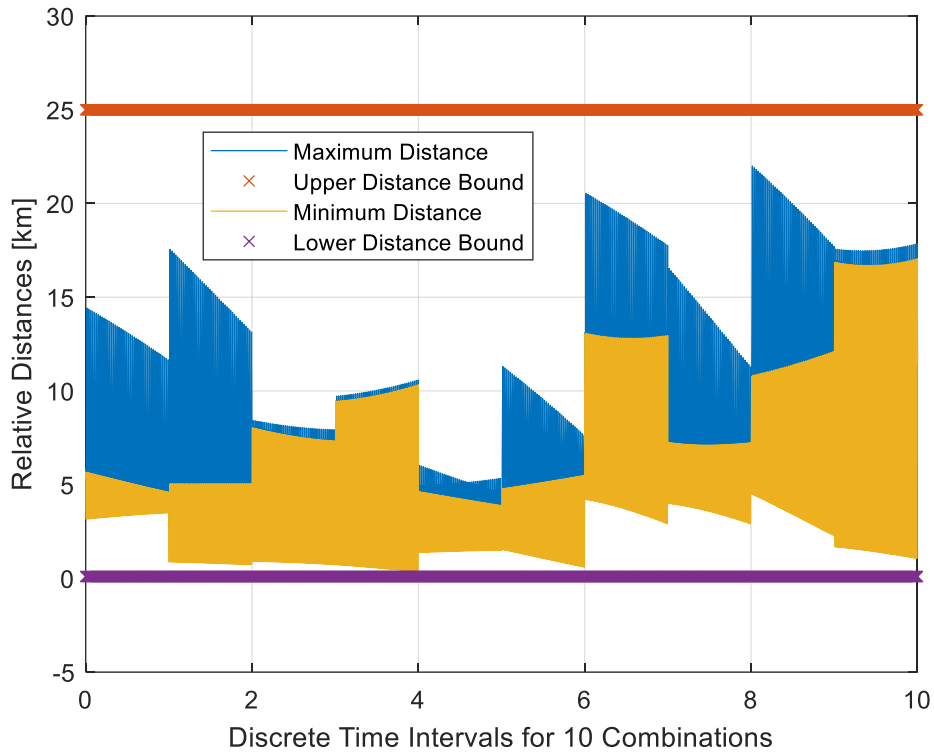
Figure 5.1. Cluster Flying 3 Day-Result for 5 Spacecraft Heterogeneous System with Safety Objective.

From the Figure 5.1, it can be concluded that the 5 spacecraft design does not violate the minimum and maximum distance constraints of 0.1 km and 25 km respectively over 3 day period. The minimum distance in RN occurs as 353.5 m. and maximum distance occurs as 22 km. in the cluster. In addition, the minimum distance in RTN occurs as 418.4 m. where the distance in RN is 364.1 m. In this way, it can be guaranteed that there is always a separation in RN when along-track distances are the lowest.

In addition to relative distance plots, the relative motion of spacecraft in Radial, Along-Track and Cross-Track (RTN) are shown in Figure 5.2, Figure 5.3, Figure 5.4 and Figure 5.5. In the plots, '*' sign marks the initial condition, T_0, and 'o' sign marks the final condition, T_f.
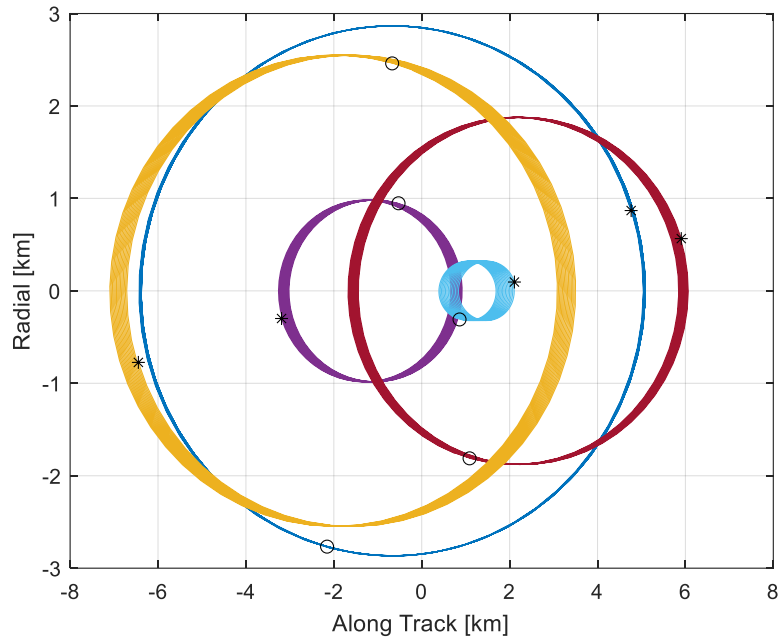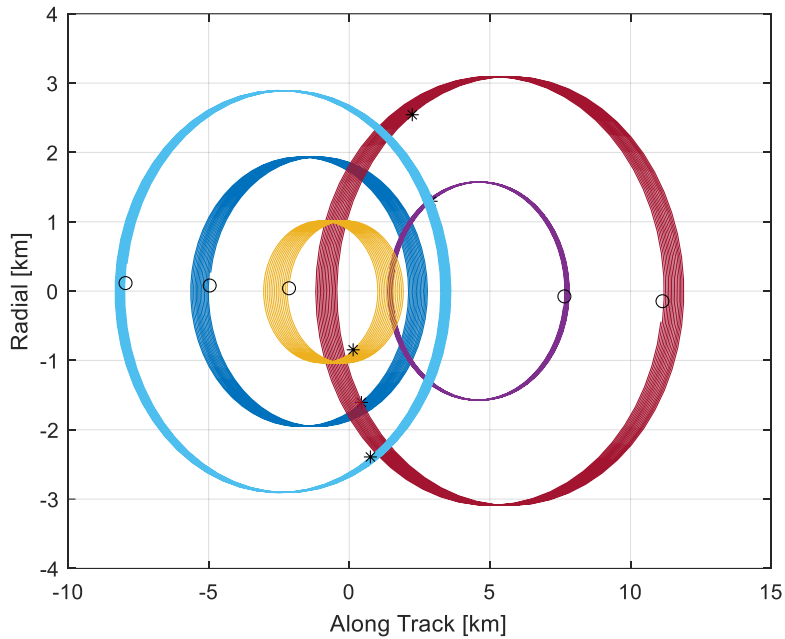
Figure 5.2. Along-Track - Radial Distances of 3 Day-Result for 5 Spacecraft Heterogeneous Cluster with Safety Objective.

The Along-Track – Radial plot for 5-spacecraft heterogeneous cluster shows that there is a radial separation between the spacecraft when along-track distance disappears. As the biggest uncertainty occurs in along-track direction, this provides an inherent safety for the cluster. Although the plot shows 3-day trajectories, there are regions where some relative orbits can intersect in along-track direction. In this case, it can be seen in Figure 5.3 and Figure 5.4 that there is always a distance in cross-track direction between these relative orbits when radial distance diminish or radial distance when cross-track distance diminish. In this way, a separation either in radial or cross rack direction is always ensured within the cluster.

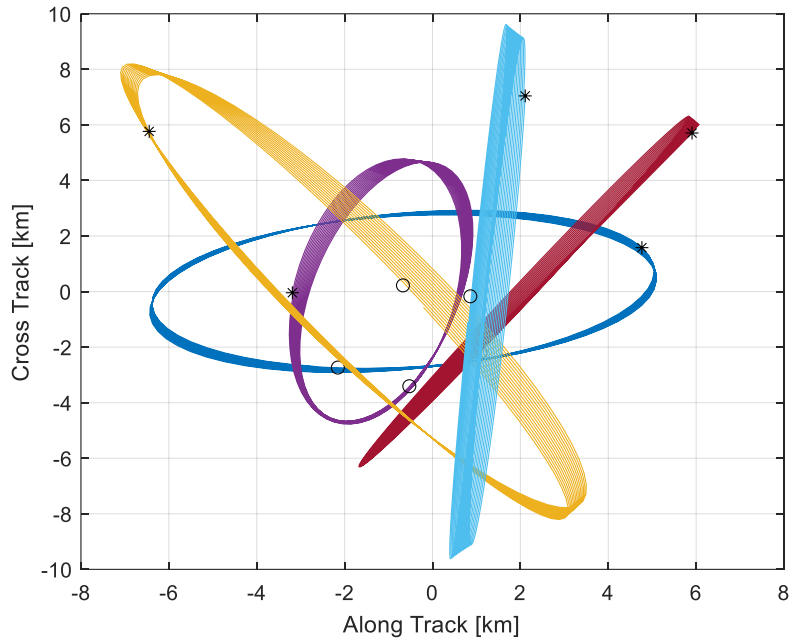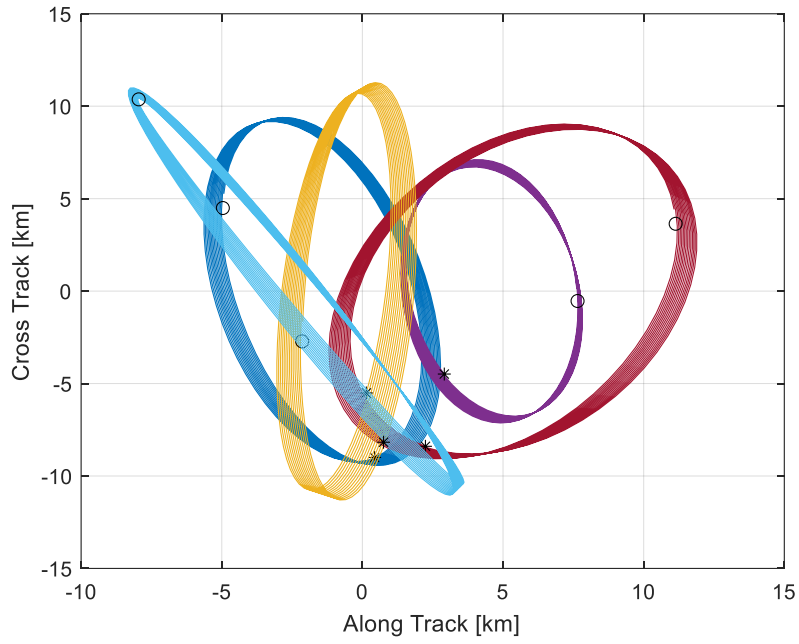Figure 5.3. Along-Track – Cross-Track Distances of 3 Day-Result for 5 Spacecraft Heterogeneous Cluster with Safety Objective.
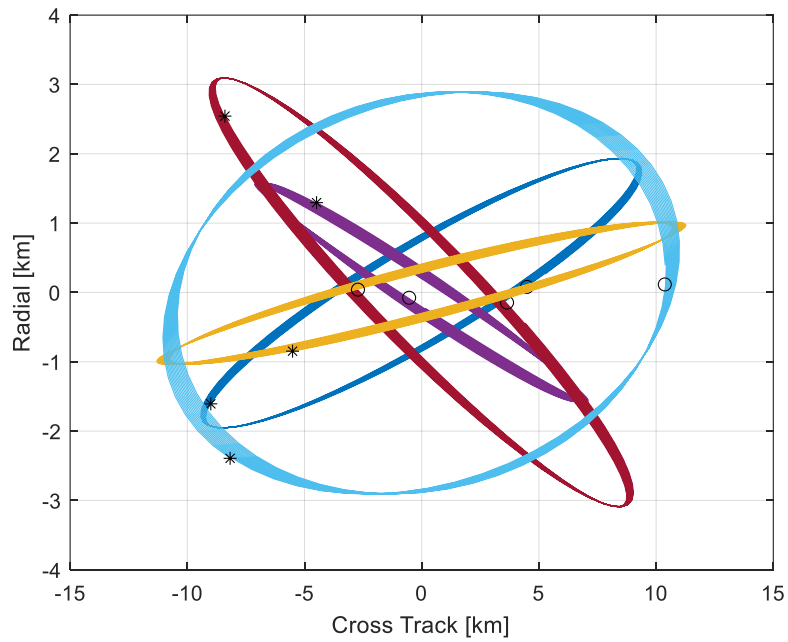
Figure 5.4. Cross-Track - Radial Distances of 3 Day-Result for 5 Spacecraft Heterogeneous Cluster with Safety Objective.
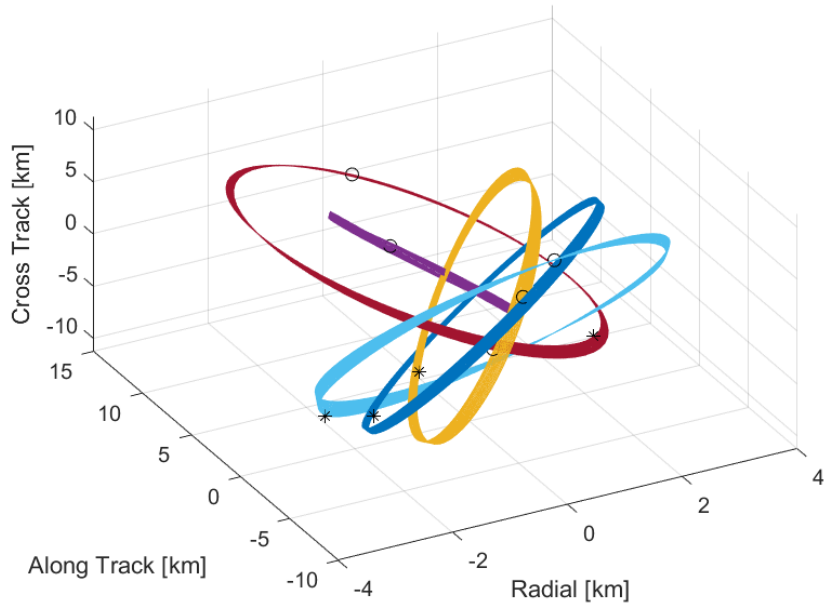
Figure 5.5. Radial – Along-Track – Cross-Track Distances of 3 Day-Result for 5 Spacecraft Heterogeneous Cluster with Safety Objective.

Here, the boundaries of the cluster are realized within a 6 x 20 x 20 km^3 volume for 5-spacecraft 3-day duration heterogeneous cluster with safety objective. When compared to the problem with station-keeping objective, the cluster with safety objective, is realized with more expansion in volume even for shorter duration. Therefore, it can be concluded that increasing safety requirements or objectives would result in more expansion in cluster size. Probabilities of collision between any 2 spacecraft for 3 days duration are shown in the Figure 5.6.
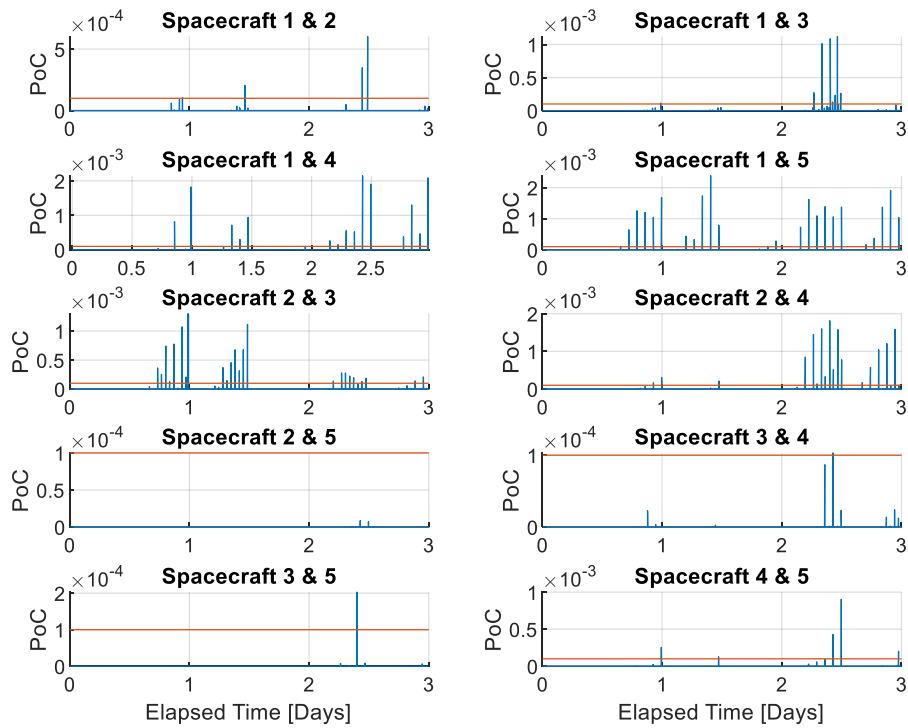
Figure 5.6. Probabilities of Collision Between 2 Spacecraft for 10 Combinations during the Simulation Duration. (Red line indicates the probability of $1\mathrm{x}10^{-4}$.)

It can be observed from the Figure 5.6 that the maximum probability of collision (PoC) between any 2 spacecraft is realized around $2\mathrm{x}10^{-3}$. Although the maximum probabilities reach the orders of 10^{-3}, they mostly stay below $1\mathrm{x}10^{-4}$. For the controlled cluster operations, these values can be acceptable depending on the operator's evaluation. Here, the maximum PoC occurs for the 4th combination where conjunction takes place between the spacecraft 1 and 5. This conjunction with associated uncertainty ellipsoids is shown in Figure 5.7.

111
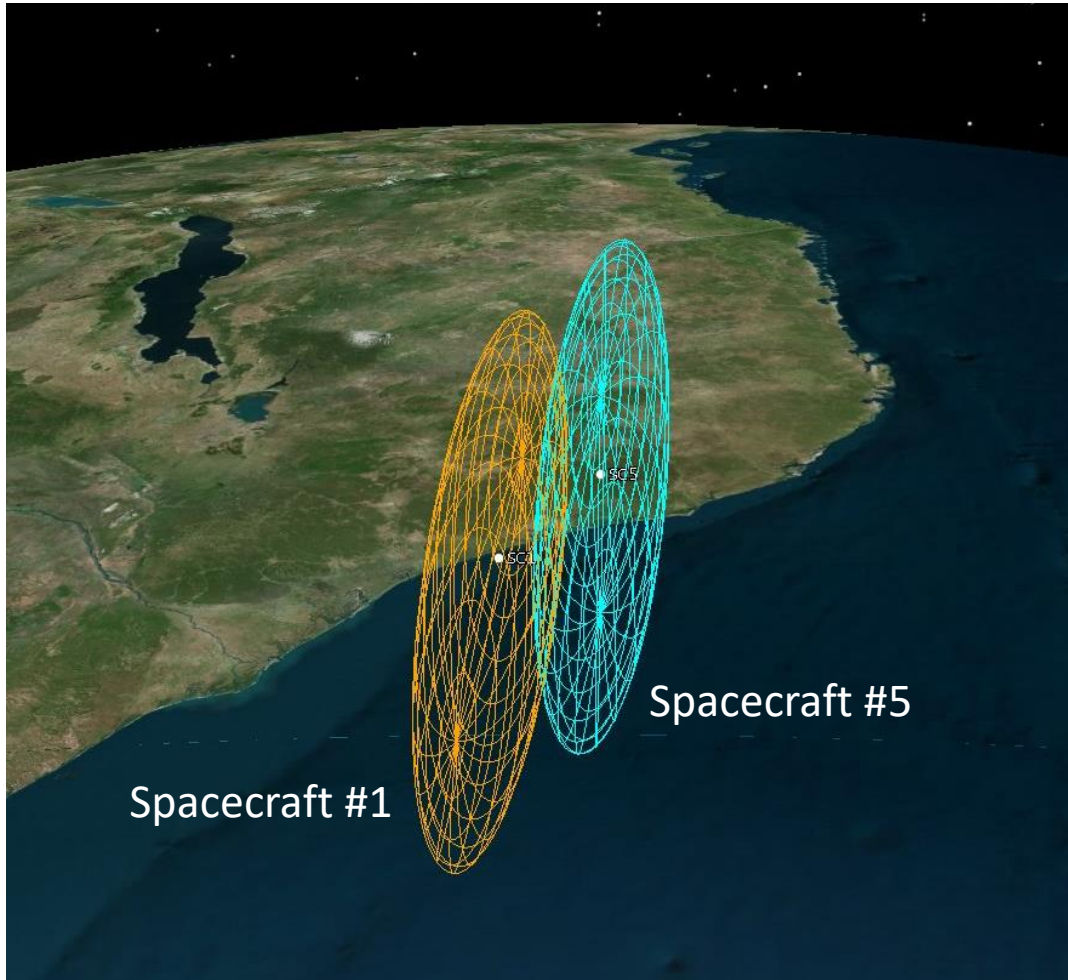
Figure 5.7. Conjunction Between Spacecraft 1 and 5 where PoC is around $2\text{x}10^{-3}$.

In Figure 5.7, it is seen that the 3 sigma covariances for spacecraft 1 and 5 intersect and the PoC value become considerable. However, the intersection is along the radial or cross track direction where the uncertainties are not the biggest and spacecraft motions are along the same direction. Also, in reality, the navigation uncertainties may be realized much lower than the values, which are defined to account for the worst cases, used in this simulation. Indeed, when good initial covariance values such as $P_{RTN,R0} = \text{diag}[\ 0.8^2,\ 1.5^2,\ 1.2^2]$ in meters^2 and $P_{RTN,V0} = [0.0016^2,\ 0.0014^2,\ 0.0009^2]$ in m^2/sec^2 are used, the maximum observed PoC occurs in the order of $1\text{x}10^{-23}$. Even in the worst-case analysis, the probabilities are observed to be within the acceptable levels for long time intervals (i.e., days). In this manner, it can be deduced

that reconfiguration maneuvers would not be required frequently for collision avoidance.

In the cluster flying design method with safety objective, the orbits are propagated with high precision and therefore it is possible to harness the natural dynamics further while designing cluster configurations. Also, navigation uncertainties are incorporated and safety measures are calculated to assess the boundaries of a cluster and its time validity (until control actions are necessary) with very high fidelity. In this manner, the method becomes ideal for a fine and precise analysis and/or assessment. However, it requires a quite high computational demand and it takes several hours to find an optimal solution for a 5-spacecraft 3-day cluster configuration.

CHAPTER 6

CLUSTER FLYING MINIMIZING DILUTION OF PRECISION

In Chapter 4 and Chapter 5, general cluster flying design methodologies are introduced with station-keeping and safety objectives. However, the developed methodology can be also applied for specific applications. One of the interesting utilizations of distributed space systems is the geolocation of ground-based (stationary) radio frequency (RF) emitters from space (Sarda, Roth, Zee, CaJacob, & Orr, 2018). In this problem, emitters are active targets with unknown positions and spaceborne receivers are used as passive sensors with known positions and velocities. In addition, the target is not cooperative which means that emitter does not transmit any information which may help the determination of its position. Therefore, the sensor is responsible for generating the measurement by processing the emitted signal. In this way, the multiple spacecraft in the distributed space system collect these signals simultaneously and generate measurements to determine the target's position information. In this chapter, introduction of mathematical performance index of Dilution of Precision (DOP) for RF geolocation and cluster design for spaceborne RF geolocation are provided in detail.

6.1   Geolocation of RF Emitters and Dilution of Precision

For RF geolocation (RFGL), mainly two methodologies can be considered in general: Frequency Difference of Arrival (FDOA) and Time Difference of Arrival (TDOA). Among these, TDOA is more widely utilized where signal time of arrivals from an emitter with respect to different observers are measured and these measurements are differenced to eliminate the unknown emission time (Nadav & Gurfil, 2022). In this way, TDOA measurements are generated to obtain relative

ranges with respect to the observers and a minimum of three observers are required to determine the emitter's position.

Firstly, let's denote $\mathbf{X}$ as the position of the terrestrial emitter to be located and s_i as the position of spacecraft in the cluster. Then, the slant range ρ_i between the spacecraft, l, with position vector, s_l, and the emitter is defined in Eq. (66).

$$\rho_i = \sqrt{(\mathbf{X} - s_l)(\mathbf{X} - s_l)^T} \tag{66}$$

The TDOA measurement between spacecraft l and m can be derived as in Eq. (67).

$$\tau_{l,m} = \frac{1}{c}(\rho_l - \rho_m) = \frac{1}{c}\left(\sqrt{(\mathbf{X} - s_l)(\mathbf{X} - s_l)^T} - \sqrt{(\mathbf{X} - s_m)(\mathbf{X} - s_m)^T}\right) \tag{67}$$

where, c is the speed of light and $l \neq m$. Based on these relations, the geometry of the TDOA geolocation is illustrated in Figure 6.1.
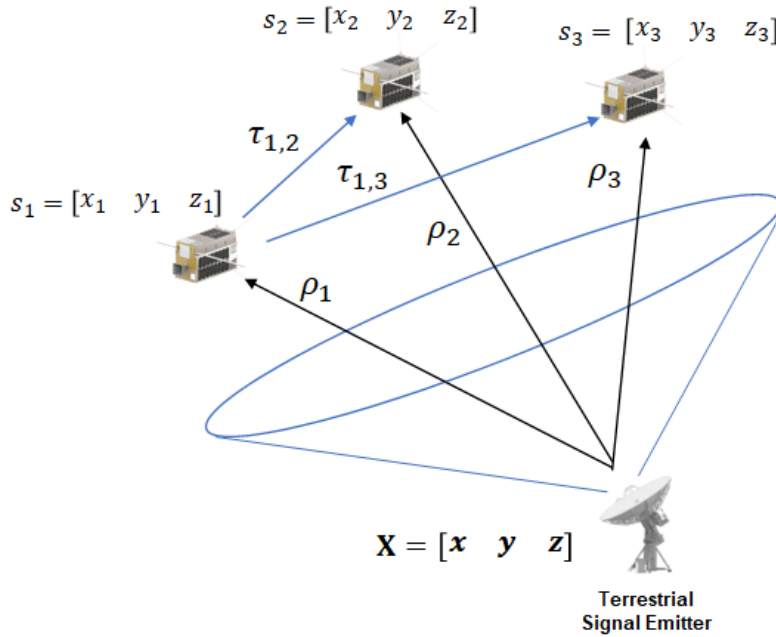
Figure 6.1. The Geometry of TDOA Geolocation

Based on this geometry, first spacecraft, $l = 1$, can be considered as reference and two TDOA measurements can be written as $\tau_{1,2}$ and $\tau_{1,3}$. Another constraint is that the RF emitter is located on the surface of the Earth and corresponding equation can be written as described in Eq. (68).

$$R_\oplus{}^2 = x^2 + y^2 + z^2 \tag{68}$$

With two equations derived from unique measurements and one constraint equation, three equations can be solved for the cartesian coordinates of emitter with three elements. However, the accuracy of the position estimation of emitter depends on the geometry between the spacecraft and the emitter which depend on the cluster design. Here, the performance index DOP for geometric distribution is derived such that minimizing it provides the most accurate position estimation. Defining the measurement function, $h(\mathbf{X})$, with equations (67) and (68), expanding it in a Taylor series about some nominal solution $\mathbf{X}_{nom}$ is provided in Eq. (69).

$$\mathbf{Z} = h(\mathbf{X}) = h(\mathbf{X}_{nom}) + \partial\mathbf{X}\left.\frac{\partial h(\mathbf{X})}{\partial \mathbf{X}}\right|_{\mathbf{X}=\mathbf{X}_{nom}} + higher\ order\ terms \tag{69}$$

where $\mathbf{Z}$ is the measurement and $\partial\mathbf{X} = \mathbf{X} - \mathbf{X}_{nom}$. The Eq. (69) can be modified as given in Eq. (70).

$$\partial\mathbf{Z} = h(\mathbf{X}) - h(\mathbf{X}_{nom}) = \partial\mathbf{X}\left.\frac{\partial h(\mathbf{X})}{\partial \mathbf{X}}\right|_{\mathbf{X}=\mathbf{X}_{nom}} \tag{70}$$

$$\partial\mathbf{Z} = H\,\partial\mathbf{X}$$

Defining $h_1(\mathbf{X})$ and $h_2(\mathbf{X})$ with $l = 1$ and $m = 2,3$ in Eq. (67) and $h_3(\mathbf{X})$ as Eq. (68), the matrix H can be written in the form of Eq. (71).

$$H = \begin{bmatrix} \dfrac{\partial h_1}{\partial x} & \dfrac{\partial h_1}{\partial y} & \dfrac{\partial h_1}{\partial z} \\ \dfrac{\partial h_2}{\partial x} & \dfrac{\partial h_2}{\partial y} & \dfrac{\partial h_2}{\partial z} \\ \dfrac{\partial h_3}{\partial x} & \dfrac{\partial h_3}{\partial y} & \dfrac{\partial h_3}{\partial z} \end{bmatrix}$$

$$= \begin{bmatrix} \dfrac{x_1-x}{\rho_1} - \dfrac{x_2-x}{\rho_2} & \dfrac{y_1-y}{\rho_1} - \dfrac{y_2-y}{\rho_2} & \dfrac{z_1-z}{\rho_1} - \dfrac{z_2-z}{\rho_2} \\ \dfrac{x_1-x}{\rho_1} - \dfrac{x_3-x}{\rho_3} & \dfrac{y_1-y}{\rho_1} - \dfrac{y_3-y}{\rho_3} & \dfrac{z_1-z}{\rho_1} - \dfrac{z_3-z}{\rho_3} \\ x & y & z \end{bmatrix} \tag{71}$$

If the Eq. (70) is solved for $\partial\mathbf{X}$, the Eq. (72) is obtained.

$$\partial \mathbf{X} = (H^T H)^{-1} H^T \partial \mathbf{Z} \tag{72}$$

If the $\partial \mathbf{X}$ and $\partial \mathbf{Z}$ are assumed to be random with zero mean, the expected error covariance would become

$$E\langle(\partial \mathbf{X})(\partial \mathbf{X})^T\rangle = E\langle(H^T H)^{-1} H^T \partial \mathbf{Z}((H^T H)^{-1} H^T \partial \mathbf{Z})^T\rangle$$
$$= (H^T H)^{-1} H^T E\langle\partial \mathbf{Z}\partial \mathbf{Z}^T\rangle H\ (H^T H)^{-1} \tag{73}$$

where $E\langle\partial \mathbf{Z}\partial \mathbf{Z}^T\rangle = \sigma^2 I$ and σ is the standard deviation of the measurement error. By re-writing Eq. (73) with this relation, the Eq. (74) is obtained.

$$E\langle(\partial \mathbf{X})(\partial \mathbf{X})^T\rangle = \sigma^2 (H^T H)^{-1} \tag{74}$$

In this manner, the minimization of the error depends on the right-hand side of the Eq. (74) which can be written in parametric form in Eq. (75).

$$(H^T H)^{-1} = \begin{bmatrix} A_{11} & A_{12} & A_{13} \\ A_{21} & A_{22} & A_{23} \\ A_{31} & A_{32} & A_{33} \end{bmatrix} = \begin{bmatrix} E\langle\Delta x^2\rangle & E\langle\Delta x\Delta y\rangle & E\langle\Delta x\Delta z\rangle \\ E\langle\Delta y\Delta x\rangle & E\langle\Delta y^2\rangle & E\langle\Delta y\Delta z\rangle \\ E\langle\Delta z\Delta x\rangle & E\langle\Delta z\Delta y\rangle & E\langle\Delta z^2\rangle \end{bmatrix} \tag{75}$$

With this, the DOP as a geometric performance parameter to be minimized is provided in Eq. (76).

$$DOP = \sqrt{A_{11} + A_{22} + A_{33}} \tag{76}$$

Finally, the performance index with non-dimensional form of DOP can be derived as given in Eq. (77).

$$J_{RFGL} = \frac{DOP}{\sigma} \tag{77}$$

where σ is the standard deviation of the receiver clock error for TDOA measurement. While designing a cluster for spaceborne RFGL applications, Eq. (77) can be utilized as a parameter to be minimized. Minimization of J_{RFGL} would provide the best accuracy for the position estimation of a specific terrestrial emitter.

6.2   Cluster Design for Spaceborne RF Geolocation

As discussed previously, designing a spacecraft cluster for spaceborne RFGL requires the minimization of geometric factor DOP. In order to achieve this, it is necessary to introduce large distances between the spacecraft when compared to close proximity examples. This is mainly due to the fact that if there is a small distance as in the case of close proximity, it results like all measurements are performed by the same receiver and therefore uniqueness of these measurements diminishes. Therefore, the bounds on design variables for spaceborne RFGL needs to be slightly different from close proximity clusters. Here, the relative semimajor axis and eccentricity differences can be set as $\Delta a_l = 0$ and $\Delta e_l = 0$ as it is more convenient to introduce large distance offsets in terms of mean anomaly or argument of latitude in the form of ΔM_l or Δu_l in general. In this manner, large along-track offsets can be obtained and out of plane differences can be introduced by relative inclination and right ascension of the ascending node, Δi_l and $\Delta \Omega_l$. With these, there would be only three design variables Δi_l, $\Delta \Omega_l$ and ΔM_l or Δu_l. For a cluster to be operated with 100 km maximum distances, the constraints on these design variables can be specified as described in Eq. (78).

$$
\begin{aligned}
-0.05° &\leq \Delta i_l \leq 0.05° \\
-0.5° &\leq \Delta \Omega_l \leq 0.5° \\
-0.5° &\leq \Delta u_l \leq 0.5°
\end{aligned}
\tag{78}
$$

In addition, it is necessary to incorporate the measurement conditions realistically by considering field of view (FoV) of the receiver and spacecraft-emitter geometry. In this manner, the nadir offset angle, ϑ, between the spacecraft and emitter as well as the angle between spacecraft and emitter positions, ϕ, can be checked whether it is possible to generate a measurement or not during the mission duration. For instance, it can be deduced that a measurement is generated if the conditions $\vartheta_j < \vartheta_{max}$ and $\phi_j < \phi_{max}$ are satisfied for time instants $j = 1, ..., T$. Here, the first condition would ensure the FoV compatibility and second condition would ensure that both spacecraft and emitter are on the same portion of the Earth's ellipsoid.

Finally, the performance index shall be checked for over the mission duration as there could be several unique measurement opportunities. Therefore, the mean of the performance index values over mission duration over a target emitter can be defined as objective function to be minimized as described in Eq. (79)

$$J = \frac{1}{M} \sum_{k=1}^{M} J_{k,RFGL} \tag{79}$$

Where k is measurement index and M is the total number of measurements generated over the mission duration. With this, a sample problem for RFGL cluster design with its assumptions is summarized in Table 6.1.

Table 6.1 RFGL Cluster Design Formulation with 3 Spacecraft and DOP Objective

Parameter	*Specification*	
Objective Function	Minimize Eq. (79)	
Constraint Function(s)	Eq. (60)	
Bounds on Design Variables	Eq. (78)	
Propagator	Analytical (SGP4)	
Inputs and Assumptions	Reference Orbit	SSO, LTDN 10:30 at 575 km altitude
	Emitter Coordinates	(39.925°, 32.866°)
	Spacecraft Number	3
	d_{min} and d_{max} in RTN Plane	30 km and 80 km
	Fixed Differences	$[\Delta a_l\ \Delta e_l] = [0\ 0]$
	Physical Differences	Defined by $\Delta \beta_l^* = 0$
	Measurement Conditions	$\vartheta_j < 50°,\ \phi_j < 21.5°$
	Duration, T_{max}	7, 14, 21 and 28 days
	Step Size	60 sec
	Sample Number	5000

In this problem, a reference orbit of Sun-Synchronous LTDN 10:30 at 575 km is specified. While the spacecraft number is fixed at 3 for a minimum number RFGL cluster, simulation duration is varied as 7, 14, 21 and 28 days. The physical differences through drag parameters, $\Delta\beta_l^*$, are not introduced as the spacecraft are assumed to be identical. While minimum and maximum distance constraints are set as 30 km and 80 km respectively, the semimajor axis and eccentricity differences, Δa and Δe, are set to 0. Finally, sample number is defined as 5000 to have a good representation of design space and generate several solutions for comparison. The sample results of an optimized solution for 3-spacecraft RFGL cluster and 28 day-duration are shown in Figure 6.2 and Figure 6.3.
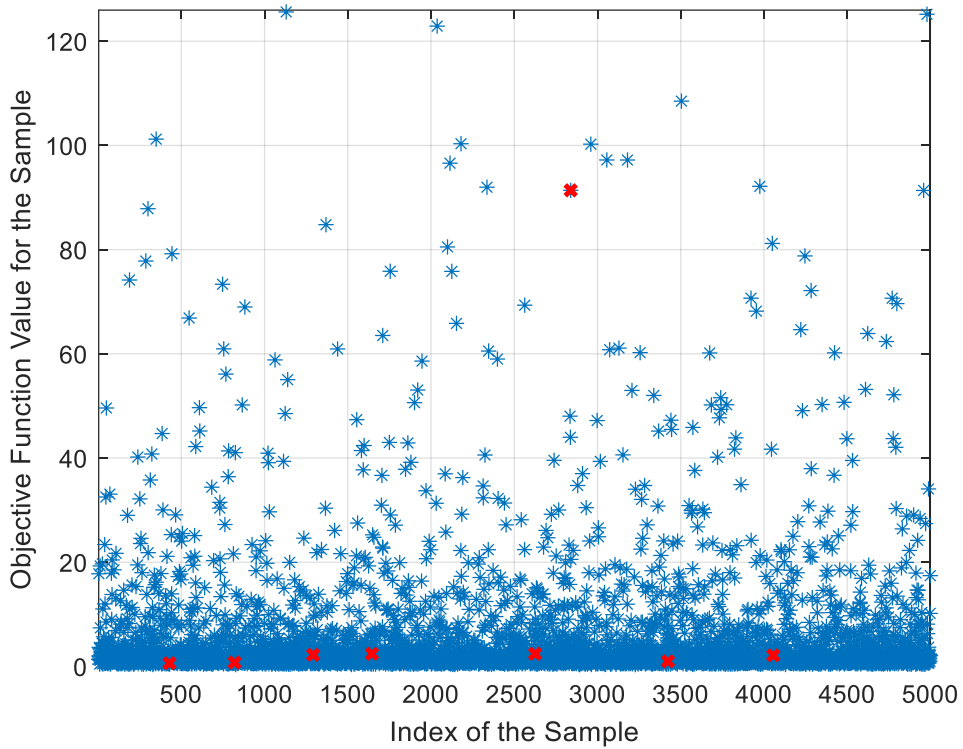
Figure 6.2. Feasible Solutions (red points) from 5000 Samples for 3-Spacecraft RFGL Cluster and 28 Day-Duration.

From Figure 6.2, it can be seen that there are 8 feasible solutions which is 0.16% of 5000 samples. Also, the objective function values, i.e., mean DOP, are quite various

121

ranging from less than 1 to higher than 100. Based on the objective function values of feasible solutions, the design point is selected such that the objective function has the minimum value of 0.627. The resulting relative distances for $C_2^3 = 3$ combinations are shown in Figure 6.3.
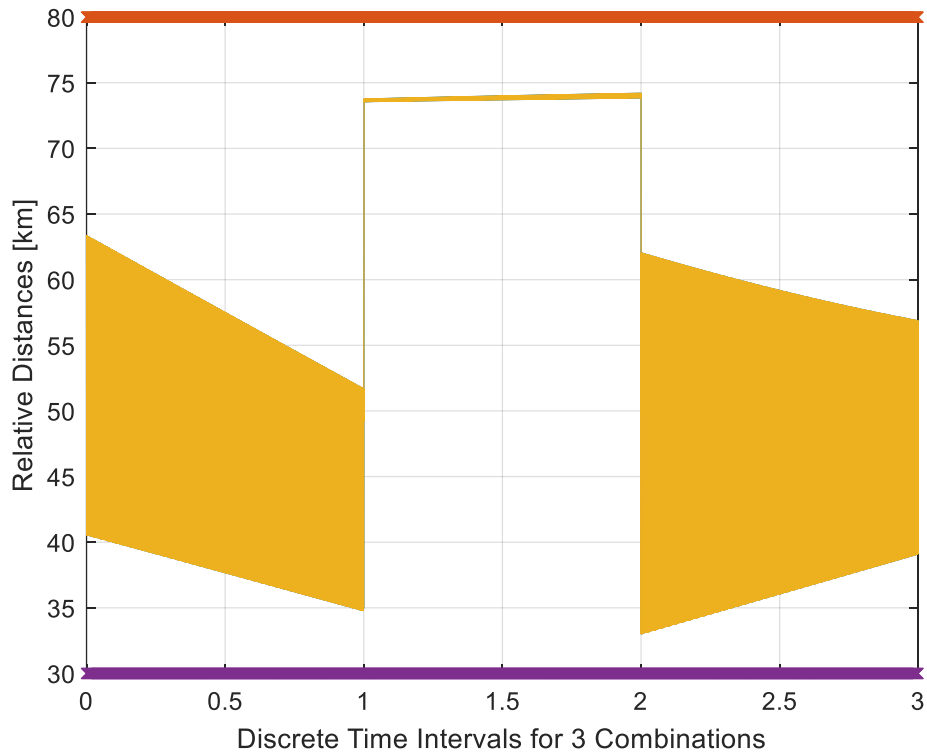
Figure 6.3. Cluster Flying 28 Day-Result for 3 Spacecraft with DOP objective.

From Figure 6.3, it can be concluded that the 3-spacecraft RFGL cluster flying design does not violate the minimum and maximum distance constraints of 30 km and 80 km respectively over 28-day period. The minimum distance occurs as 33 km. and maximum distance occurs as 74.2 km. in the cluster. The resulting geometry of RFGL spacecraft cluster over the emitter is shown in Figure 6.4. Here, the red points mark the spacecraft positions and white point marks the emitter position.

Figure 6.4. RFGL Cluster Geometry of 3 Spacecraft with Respect to Emitter.

The cluster geometry shown in Figure 6.4 indicates that the spacecraft are distributed such that large distance offsets between the spacecraft are achieved to minimize DOP while passing over the emitter. In addition, the results for several simulation durations from 7 to 28 days are provided in Table 6.2.

Table 6.2 RFGL Cluster Design Results with 3 Spacecraft for Various Durations

	7 days	*14 days*	*21 days*	*28 days*
Solution Percentage	0.92%	0.42%	0.28%	0.16%
Min. Objective Value	0.547	0.622	0.712	0.627

From Table 6.2, it can be deduced that the simulation duration does not have a significant impact on the objective function value. However, the solution number decreases as the simulation duration increases.

In order to see the effect of more spacecraft in the RFGL cluster, the problem defined in Table 6.1 is modified by specifying spacecraft number as 4 and minimum and maximum distance constraints are set as 20 km and 100 km. The resulting problem is defined in Table 6.3.

Table 6.3 RFGL Cluster Design Formulation with 4 spacecraft and DOP Objective

Parameter	Specification	
Objective Function	Minimize Eq. (79)	
Constraint Function(s)	Eq. (60)	
Bounds on Design Variables	Eq. (78)	
Propagator	Analytical (SGP4)	
Inputs and Assumptions	Reference Orbit	SSO, LTDN 10:30 at 575 km altitude
	Emitter Coordinates	(39.925°, 32.866°)
	Spacecraft Number	4
	d_{min} and d_{max} in RTN Plane	20 km and 100 km
	Fixed Differences	$[\Delta a_l \ \Delta e_l] = [0 \ 0]$
	Physical Differences	Defined by $\Delta \beta_l^* = 0$
	Measurement Conditions	$\vartheta_j < 50°, \ \phi_j < 21.5°$
	Duration, T_{max}	7, 14, 21 and 28 days
	Step Size	60 sec
	Sample Number	5000

The sample results of an optimized solution for 4-spacecraft RFGL cluster and 28 day-duration are shown in Figure 6.5 and Figure 6.6.
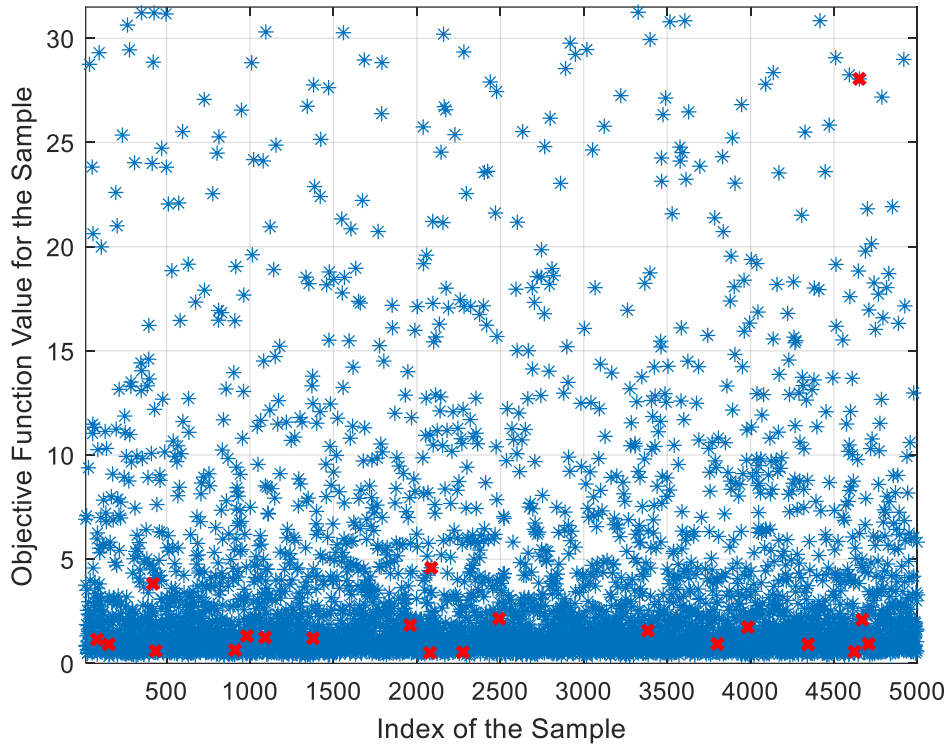
Figure 6.5. Feasible Solutions (red points) from 5000 Samples for 4-Spacecraft RFGL Cluster and 28 Day-Duration.

From Figure 6.5, it can be seen that there are 21 feasible solutions which is 0.42% of 5000 samples. Also, the objective function values, i.e., mean DOP, are quite various ranging from less than 1 to higher than 30. Based on the objective function values of feasible solutions, the design point is selected such that the objective function has the minimum value of 0.502. The resulting relative distances for $C_2^4 = 6$ combinations are shown in Figure 6.6.
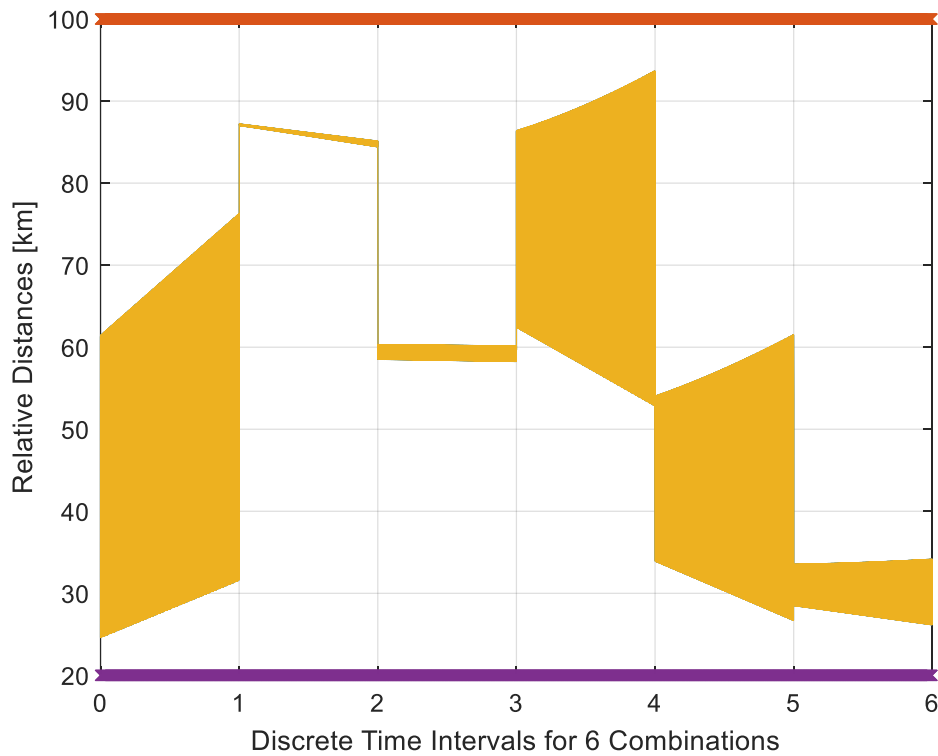
Figure 6.6. Cluster Flying 28 Day-Result for 4 Spacecraft with DOP objective.

From Figure 6.6, it can be concluded that the 4-spacecraft RFGL cluster flying design does not violate the minimum and maximum distance constraints of 20 km and 100 km respectively over 28-day period. The minimum distance occurs as 24.6 km. and maximum distance occurs as 93.7 km. in the cluster. The resulting geometry of RFGL spacecraft cluster over the emitter is shown in Figure 6.7. Here, the red points mark the spacecraft positions and white point marks the emitter position.

The cluster geometry shown in Figure 6.7 indicates that the spacecraft are distributed such that large distance offsets between the spacecraft are achieved to minimize DOP while passing over the emitter. In addition, the removal of any spacecraft from the cluster would still provide large distance offsets between the spacecraft and a reasonable DOP can be still achieved.
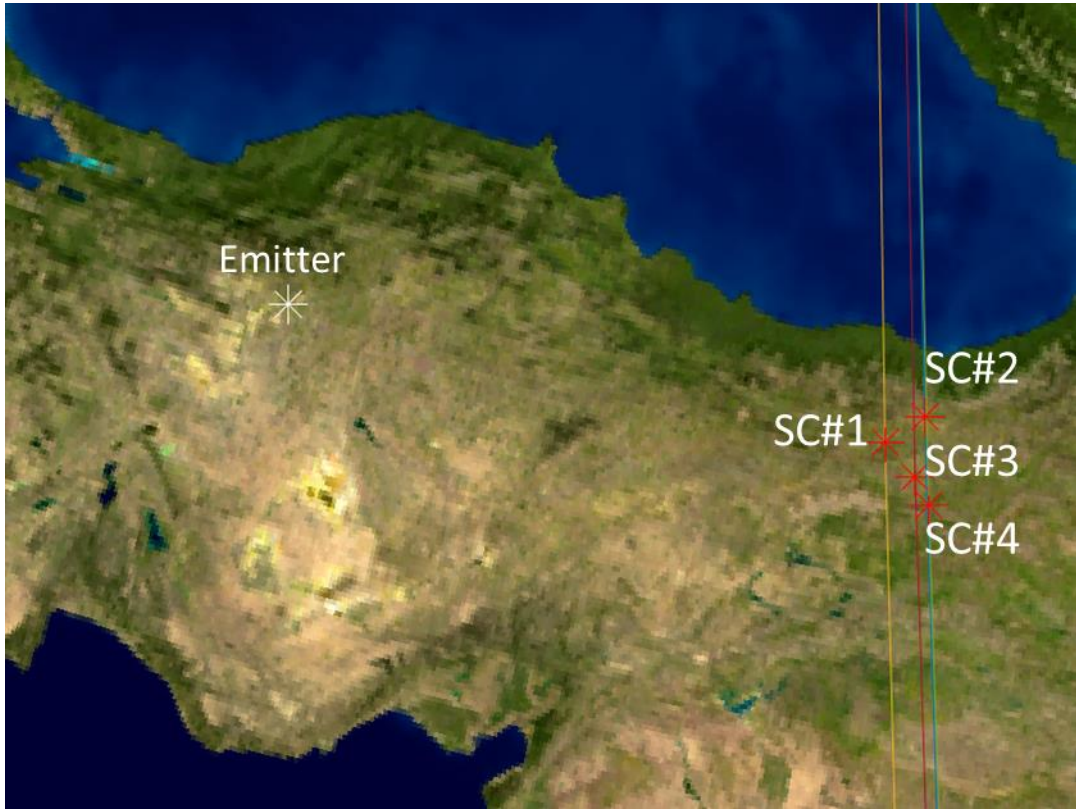
Figure 6.7. RFGL Cluster Geometry of 4 Spacecraft with Respect to Emitter.

The results for several simulation durations from 7 to 28 days are also provided in Table 6.4.

Table 6.4 RFGL Cluster Design Results with 4 Spacecraft for Various Durations

	7 days	*14 days*	*21 days*	*28 days*
Solution Percentage	1.1%	0.84%	0.6%	0.42%
Min. Objective Value	0.3795	0. 5631	0.5872	0.5024

From Table 6.4, it can be deduced that the simulation duration does not have a significant impact on the objective function value. However, the solution number decreases as the simulation duration increases. When compared to 3-spacecraft cluster, the 4-spacecraft cluster with more relaxed distance constraints becomes more robust with respect to spacecraft losses and DOP values are also improved.

CHAPTER 7

CLUSTER RECONFIGURATION WITH CONTROL CONSTRAINTS

In previous chapters, cluster flying design providing passively safe long-term operations which would not require any reconfiguration over a specific time interval is developed. However, as the time validity of the configuration expires through violation of constraints or mission requirements, reconfiguration of the cluster is necessary. In this chapter, cluster flying design methodology which is explained in Chapter 3 is extended to reconfiguration problem. Here, sequential cluster configurations are found by minimizing the total maneuvering effort which transfers initial cluster to the next one while bounding deviations from a reference mean orbit for long time intervals. The minimization of maneuvering effort is realized through generating delta-V (ΔV) maps and associating relative orbits on the current configuration to the next one using an auction algorithm. In this way, the auction algorithm provides the lowest total delta-V for whole cluster. Here, reference ΔV values for reconfiguration are calculated based on an optimal impulsive transfer (OIT) methodology to obtain theoretical minimum. Although new configurations are found through reconfiguration in this way, impulsive transfer results in infeasible ΔV requirements for real life systems. Therefore, the reconfiguration ΔV map is recalculated by utilizing constrained optimal control methodologies which incorporates ΔV limitations so that the realistic control inputs are found.

In the following chapters, the sequential cluster design and reconfiguration strategy as well as different methodologies for relative orbit transfer such as impulsive, model predictive control and nonlinear optimal control are introduced with their performance evaluation. Finally, a case study for the RFGL mission is provided.

7.1   Sequential Cluster Design and Reconfiguration

The reconfiguration of a spacecraft cluster is considered as designing sequential cluster configurations based on minimizing total maneuvering effort. Here, as described previously, sequential configurations of spacecraft clusters are found initially. Then, reconfiguration maneuvers are calculated for each spacecraft to change its orbit and move into another orbit in the next configuration. This process is illustrated in Figure 7.1.

1st Configuration
1. Calculate Reference Orbit
2. High Precision Propagation
3. Mean Orbit (TLE) Fitting
4. Distribute Spacecraft

2nd Configuration
1. High Precision Propagation
2. Mean Orbit (TLE) Fitting
3. Distribute Spacecraft
4. Calculate Reconfiguration
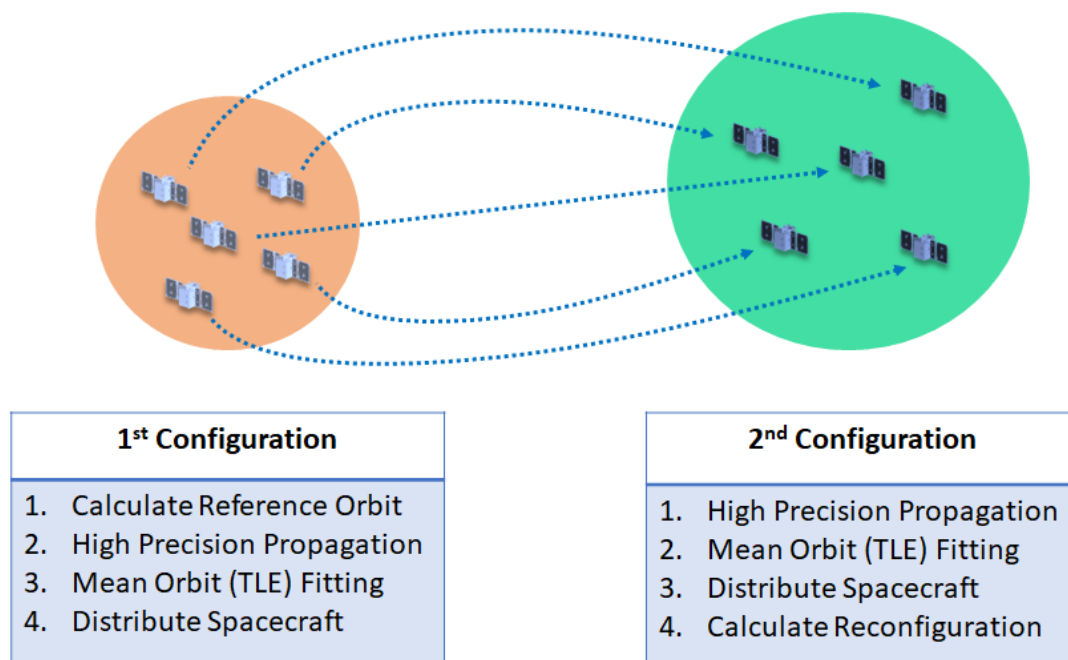
Figure 7.1. Overview of Sequential Cluster Design and Reconfiguration.

Firstly, an initial reference orbit is calculated, propagated for the cluster design time interval (i.e. days) and using the resulting ephemeris a mean orbit, or TLE, is fitted. Then a cluster is designed for station-keeping or safety objectives as described in previous chapters using the mean orbit or ephemeris. When the 1st configuration is expired, a 2nd configuration can be found by minimizing the total maneuver effort while satisfying the same distance constraints. The timeline representation and implementation of this process is shown in Figure 7.2.
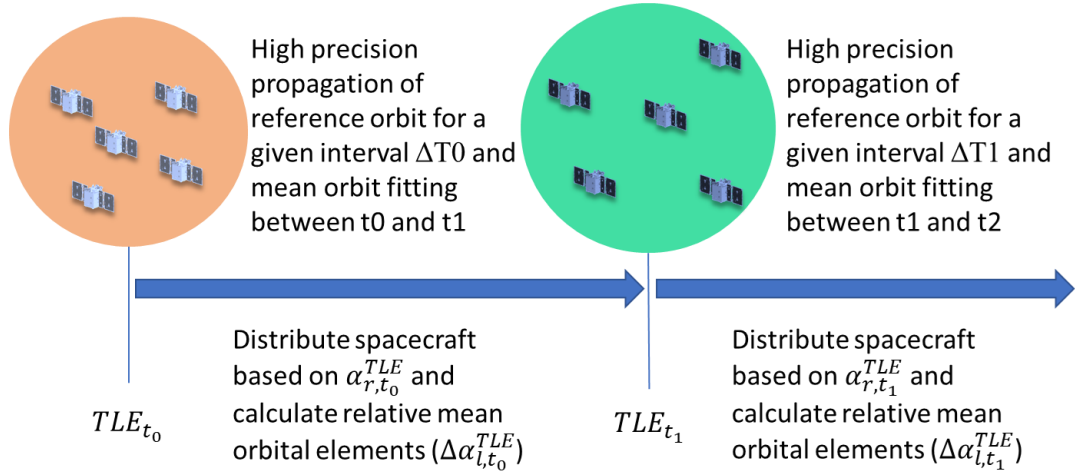
Figure 7.2. Implementation of Sequential Cluster Design and Reconfiguration.

As it can be seen from Figure 7.2, the relative orbital elements are found around the mean orbital elements which are fitted for the numerically propagated reference orbit. Then the differences between the relative orbital elements from initial cluster to next can be calculated by using Eq. (80).

$$\Delta oe = \left(\alpha_{r,t_1}^{TLE} + \Delta\alpha_{l,t_0}^{TLE}\right) - \left(\alpha_{r,t_1}^{TLE} + \Delta\alpha_{l,t_1}^{TLE}\right) \tag{80}$$

This difference in relative orbits determines the reconfiguration maneuver requirements. The reconfiguration is formulated such that each spacecraft assigned to a specific relative orbit within the initial cluster is transferred to each relative orbit in the next cluster. While calculating the orbital transfers, an algorithm by (Eagle, 2021) which is based on two-impulse optimal transfer methodology developed by (Lee, 1964) and (McCue & Bender, 1965) is utilized. Using the resulting information from orbital transfers, a ΔV map is generated to represent maneuvering requirements. A sample ΔV map for a 5-spacecraft cluster is given in Table 7.1. Here, $RO_{i,tj}$ stands for relative orbit i of the configuration at time instant j. For instance, orbital transfer from first relative orbit of first configuration at t_0 to the second relative orbit of second configuration at t_1 requires a ΔV of 2.43 meters per second. Then this table is used to assign spacecraft from initial cluster configuration to the next one by minimizing the total maneuver effort for whole cluster utilizing an auction algorithm developed by (Bertsekas, 1992).

Table 7.1 Sample ΔV Map for a Reconfiguration of 5 Spacecraft Cluster

ΔV [m/sec]	$RO_{1,t1}$	$RO_{2,t1}$	$RO_{3,t1}$	$RO_{4,t1}$	$RO_{5,t1}$
$RO_{1,t0}$	7.95	**2.43**	13.34	15.6	15
$RO_{2,t0}$	**3.1**	6.9	6.76	8.3	10.2
$RO_{3,t0}$	3.43	8.03	**4**	6.46	7.6
$RO_{4,t0}$	5.13	11.3	4.98	**4.34**	6.99
$RO_{5,t0}$	6.02	1.89	11.05	13.33	**12.99**

From the sample ΔV map given in Table 7.1, minimum total maneuvering effort is obtained if the reconfiguration is performed as follows: $RO_{1,t0}$ → $RO_{2,t1}$, $RO_{2,t0}$ → $RO_{1,t1}$, $RO_{3,t0}$ → $RO_{3,t1}$, $RO_{4,t0}$ → $RO_{3,t1}$, $RO_{5,t0}$ → $RO_{5,t1}$. The total ΔV requirement for whole cluster would become 26.9 m/sec. The final problem for cluster reconfiguration can be formulized with an objective to minimize the total transfer as described in (81).

$$J = \sum_{l=1}^{5} \sum_{j=1}^{T} \left| \begin{bmatrix} \Delta V_{l,j}^{R} & \Delta V_{l,j}^{T} & \Delta V_{l,j}^{N} \end{bmatrix} \right| \tag{81}$$

Using this cost function, it is possible to calculate the norm of the total maneuvering effort that is separately calculated for RTN directions. The resulting reconfiguration problem and parameters for a reference simulation are summarized in Table 7.2.

Table 7.2 Reconfiguration Problem with the Objective of Minimizing Total Maneuvering for a Cluster of 5 Spacecraft

Parameter	*Specification*
Objective Function	Minimize Eq. (81)
Constraint Function(s)	Eq. (59)
Bounds on Design Variables	Eq. (65)

Propagator	Analytical (SGP4)	
Inputs and Assumptions	Reference Orbit	SSO, LTDN 10:30 at 685 km altitude
	Spacecraft Number	5
	d_{min} and d_{max} in RTN Plane	0.1 km and 20 km
	Maneuver Calculation Methodology	OIT
	Physical Differences	Defined by $\Delta\beta_i^* = 0$
	Duration, T_{max}	3 days
	Step Size	10 sec
	Sample Number	1000

The design space exploration results for this problem are given in the Figure 7.3.
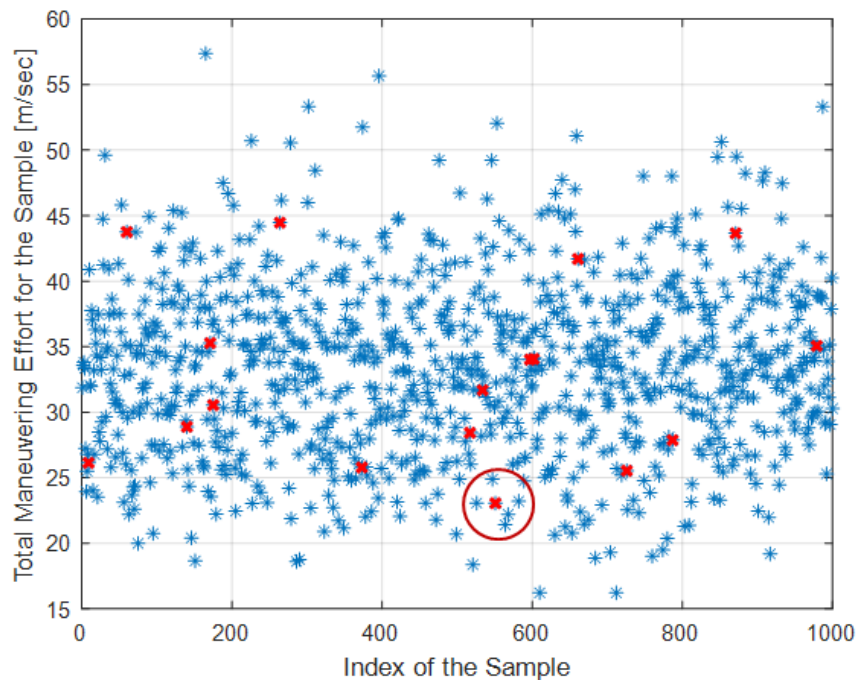
Figure 7.3. Design Space Exploration Results for 5 Spacecraft Cluster Reconfiguration.

From the Figure 7.3, it can be seen that there are 17 solutions and the solution with minimum maneuvering effort for the cluster results in 23 m/sec of total ΔV. In addition, the ΔV map for this solution is given in Table 7.3. Here, it should be noted that there are no solutions for 2 transfers.

Table 7.3 ΔV Map for a Reconfiguration of 5 Spacecraft Cluster with OIT

ΔV [m/sec]	$RO_{1,t1}$	$RO_{2,t1}$	$RO_{3,t1}$	$RO_{4,t1}$	$RO_{5,t1}$
$RO_{1,t0}$	**3.42**	6.95	9.83	10.85	15.24
$RO_{2,t0}$	9.67	**2.75**	6.61	7.33	8.96
$RO_{3,t0}$	9.17	-	**2.04**	4.69	6.1
$RO_{4,t0}$	13.72	6.95	7.4	6.57	**5.96**
$RO_{5,t0}$	-	4.96	7.63	**8.88**	13

From the ΔV map given in Table 7.3, minimum total maneuvering effort is obtained if the reconfiguration is performed as follows: $RO_{1,t0} \rightarrow RO_{1,t1}$, $RO_{2,t0} \rightarrow RO_{2,t1}$, $RO_{3,t0} \rightarrow RO_{3,t1}$, $RO_{4,t0} \rightarrow RO_{5,t1}$, $RO_{5,t0} \rightarrow RO_{4,t1}$. The resulting configuration is simulated for 3 days and the distances between any two spacecraft during each time instant for $C_2^5 = 10$ combinations are shown in the Figure 7.4. In the figure, each discrete time interval, for example 0 to 1, 1 to 2, etc. until 9 to 10, corresponds to 3-day simulation result for each combination of Spacecraft 1 and 2, Spacecraft 1 and 3, etc. until 10th combination of Spacecraft 4 and 5.
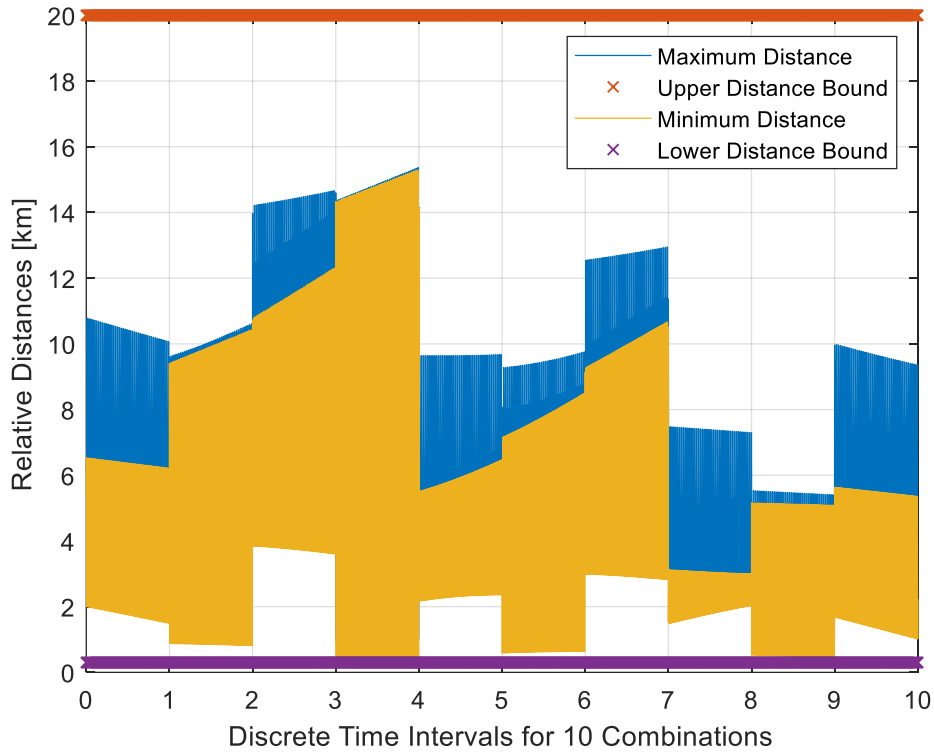
Figure 7.4. Cluster Flying 3 Day-Result for 5 Spacecraft with Minimum Impulsive Maneuvering Objective.

From Figure 7.4, it may be concluded that the 5-spacecraft reconfiguration does not violate the minimum and maximum distance constraints of 0.1 km and 20 km respectively over 3-day period. Here, the solution to the problem given in Table 7.2 provides the minimum theoretical maneuver requirement as the maneuvers are performed impulsive. In addition, impulsive transfer is computationally effective to identify potentially close orbits to calculate the reconfiguration. However, the required impulsive maneuvers are quite large or not possible to execute instantaneously (or quasi-instantaneously with a short duration) utilizing a real-life propulsion system. Therefore, it is necessary to introduce constraints on control inputs while transferring the cluster from current configuration to the next one. The solutions with input constraints are explained in Chapter 7.2 utilizing model predictive control (MPC) with linear time invariant (LTI) dynamics and in Chapter 7.3 utilizing nonlinear optimal control with linear time variant (LTV) dynamics.

7.2   Reconfiguration by Model Predictive Control

Another methodology to transfer a spacecraft to another orbit is the utilization of Model Predictive Control. Here, MPC is formulated to control relative motion where the objective is minimizing the overall control effort and state error with respect to the target orbit at the terminal time instant. To formulize this problem, the relative motion formulized in Eq. (42) is expressed as LTI system with Eq. (82) and Eq. (83).

$$
A = \begin{bmatrix} 0 & 0 & 0 & 1 & 0 & 0 \\ 0 & 0 & 0 & 0 & 1 & 0 \\ 0 & 0 & 0 & 0 & 0 & 1 \\ 3n^2 & 0 & 0 & 0 & 2n & 0 \\ 0 & 0 & 0 & -2n & 0 & 0 \\ 0 & 0 & -n^2 & 0 & 0 & 0 \end{bmatrix}, B = \begin{bmatrix} 0 & 0 & 0 \\ 0 & 0 & 0 \\ 0 & 0 & 0 \\ 1 & 0 & 0 \\ 0 & 1 & 0 \\ 0 & 0 & 1 \end{bmatrix} \tag{82}
$$

$$
x = \begin{bmatrix} x & y & z & \dot{x} & \dot{y} & \dot{z} \end{bmatrix}^T \qquad u = \begin{bmatrix} u_x & u_y & u_z \end{bmatrix}^T
$$

$$
Discrete\ System\ Dynamics:\ x_{k+1} = Ax_k + Bu_k \tag{83}
$$

Where n is the mean motion of the reference orbit, $k = 1, \dots, N$ are discrete time instants, x, y, z represents the relative states and u_x, u_y, u_z are control inputs in RTN directions. Then, MPC is formulated for N predictions as follows:

$$
Predictions:\quad X_k = \begin{bmatrix} x_{1|k} \\ \vdots \\ x_{N|k} \end{bmatrix}, U_k = \begin{bmatrix} u_{0|k} \\ \vdots \\ u_{N-1|k} \end{bmatrix} \tag{84}
$$

$$
Quadratic\ Cost:\quad J_k = J(x_k, u_k)
$$

$$
= \sum_{0}^{N-1} \left(\|x_{i|k}\|_Q^2 + \|u_{i|k}\|_R^2 + \|x_{N|k}\|_P^2 \right) \tag{85}
$$

where $\|x\|_Q^2 = x^T Q x$, $\|u\|_R^2 = u^T R u$ and Q, R and P are the weighting matrices for state, controls and terminal state respectively.

$$X_k = \mathcal{M}x_k + \mathcal{C}U_k$$

where

(86)

$$\mathcal{C} = \begin{bmatrix} B & 0 & \dots & 0 \\ AB & B & \dots & 0 \\ \vdots & \vdots & \ddots & \vdots \\ A^{N-1}B & A^{N-2}B & \dots & B \end{bmatrix}, \quad \mathcal{M} = \begin{bmatrix} A \\ A^2 \\ \vdots \\ A^N \end{bmatrix}$$

Predicted cost to be minimized becomes:

$$J_k = U_k^T H U_k + 2x_k^T F^T U_k$$

where

(87)

$$H = \mathcal{C}^T \mathcal{Q} \mathcal{C} + \mathcal{R}, \quad F = \mathcal{C}^T \mathcal{Q} \mathcal{M},$$

$$\mathcal{Q} = diag\{Q, \dots, Q, P\} \text{ and } \mathcal{R} = diag\{R, \dots, R, R\}$$

Constraints: $\qquad\qquad A_c U_k \le b_c + B_c x_k$ (88)

Having this formulation, the settings of the reconfiguration problem with MPC are summarized in Table 7.4.

Table 7.4 Orbital Transfer Formulation with LTI System MPC

Parameter	Specification
Target State	$x_{target} = [0\ 0\ 0\ 0\ 0\ 0]^T$
Stop Condition	$x_{position,error} < 10$ m.
Time Step	60 sec.
Prediction Horizon	300 (~3 orbits)
Bounds on ΔV Input	$u_{min} = -0.1$ m/sec, $u_{max} = 0.1$ m/sec

Using these settings, the solution found in Figure 7.3 is recalculated and the ΔV map is regenerated which is given in Table 7.5.

Table 7.5 ΔV Map for the Reconfiguration of 5 Spacecraft Cluster with MPC

ΔV [m/sec]	$RO_{1,t1}$	$RO_{2,t1}$	$RO_{3,t1}$	$RO_{4,t1}$	$RO_{5,t1}$
$RO_{1,t0}$	**7.36**	13.22	15.06	13.31	24.1
$RO_{2,t0}$	14.86	8.97	9.82	**9.03**	14.7
$RO_{3,t0}$	12.2	5.2	**3.16**	9.02	7.7
$RO_{4,t0}$	19.02	10.4	7.6	9.61	**7.2**
$RO_{5,t0}$	6.86	**10.0**	11.52	12.2	20.43

In addition, a sample reconfiguration result is given for $RO_{1,t0}$ → $RO_{1,t1}$ in Figure 7.5 and Figure 7.6.
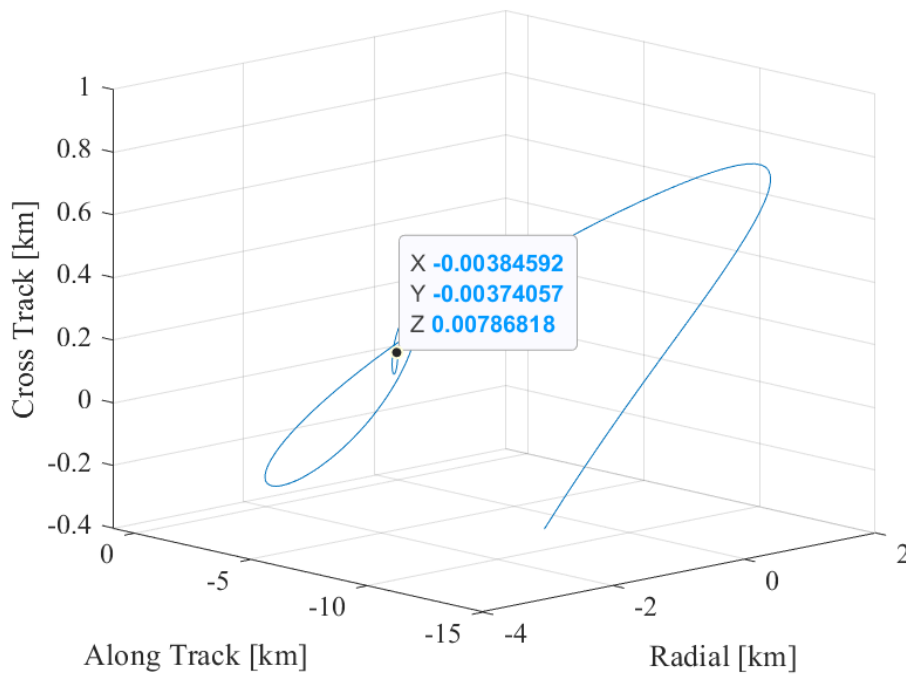
Figure 7.5. Relative Trajectory of MPC Reconfiguration $RO_{1,t0}$ → $RO_{1,t1}$.

Figure 7.6. Control History of MPC Reconfiguration $RO_{1,t0} \rightarrow RO_{1,t1}$.

From the ΔV map given in Table 7.3, minimum total maneuvering effort is obtained if the reconfiguration is performed as follows: $RO_{1,t0} \rightarrow RO_{1,t1}$, $RO_{2,t0} \rightarrow RO_{4,t1}$, $RO_{3,t0} \rightarrow RO_{3,t1}$, $RO_{4,t0} \rightarrow RO_{5,t1}$, $RO_{5,t0} \rightarrow RO_{2,t1}$. Here, the solution with minimum maneuvering effort for the cluster results in 36.8 m/sec of total ΔV. From the Figure 7.5 and Figure 7.6 it can be seen that the solution is found when the stopping condition for relative distance error is satisfied and controls are almost converged except cross track to reduce further the small relative position error. Also, the maximum control input is bounded by 0.1 m/sec which would result in a thrust level less than 0.167 N for a 100 kg satellite with step size of 60 seconds.

When OIT and MPC methodologies are compared, it can be observed that the MPC requires more maneuvering effort (about 1.6 times of the impulsive transfer requirement) as expected. However, with MPC, it is possible to put constraints on control inputs based on thruster limitations and find solutions where impulsive

transfer is not possible. While it takes half an orbit for impulsive transfer to be realized, it takes around 2 to 3 orbits for MPC solution to complete reconfiguration. The total cost, i.e. the maneuvering effort, can be reduced by increasing the penalty on control inputs via the term R in Eq. (85), however, this will result in more transfer time and need to be checked for safety conditions (Eq. (59)) continuously. Finally, as there is an extensive dynamics calculation for prediction horizon, MPC results in more computational demand when compared to OIT.

7.3   Reconfiguration by Nonlinear Optimal Control

In order to reduce computational demand and find solutions for optimal transfer, the problem defined in Chapter 7.2 is reformulated by utilizing a nonlinear optimal control (NOC) technique. Here, NOC is also formulated to control relative motion where the objective is minimizing the overall control effort and state error with respect to the target orbit at the terminal time instant. Here, the objective, or cost, function can be written for the overall control effort in Eq. (89).

$$J = \sum_{k=1}^{N} u_k^T u_k \tag{89}$$

Then the constraints for the relative dynamics, terminal states and control inputs are defined in Eq. (90).

$$
\begin{aligned}
x_{k+1} &= f(x_k, u_k), \\
x_{N+1} &= [0\ 0\ 0\ 0\ 0\ 0]^T, \\
u_{min} &\leq u_k \leq u_{max}.
\end{aligned}
\tag{90}
$$

Where $f(x_k, u_k)$ is the relative dynamics formulated in Eq. (82) and (83) which is integrated via RK4 and $N + 1$ is the terminal time instant where the relative position and velocity are expect to diminish with respect to target orbit. If the relative position and velocity diminish then spacecraft is totally transferred to the target orbit. The final formulation for the LTI system NOC is summarized in Table 7.6.

Table 7.6 Orbital Transfer Formulation with LTI System NOC

Parameter	Specification
Objective Function	Minimize Eq. (89)
Constraint Function(s)	Eq. (90)
System Dynamics	Eq. (82) and (83)
Time Step	60 sec.
Simulation Duration	N =300 steps (~3 orbits)
Bounds on ΔV Input	u_{min} = -0.1 m/sec, u_{max} = 0.1 m/sec

For the optimization, the Interior Point Optimizer (IPOPT) developed by (Wächter & Biegler, 2006) is used with the CasADi framework developed by (Andersson, Gillis, Horn, Rawlings, & Diehl, 2019). Using these settings, the solution found in Figure 7.3 is recalculated and the resulting ΔV map is given in Table 7.7.

Table 7.7 ΔV Map for the Reconfiguration of 5 Spacecraft Cluster with LTI NOC

ΔV [m/sec]	$RO_{1,t1}$	$RO_{2,t1}$	$RO_{3,t1}$	$RO_{4,t1}$	$RO_{5,t1}$
$RO_{1,t0}$	**4.27**	9.8	12.75	13.89	19.75
$RO_{2,t0}$	11.91	**4.85**	7.99	9.23	11.97
$RO_{3,t0}$	11.74	5.64	**2.66**	6.28	7.82
$RO_{4,t0}$	17.01	8.87	7.34	8.09	**6.74**
$RO_{5,t0}$	4.46	7.21	9.89	**11.41**	16.85

In addition, sample reconfiguration results are given for $RO_{1,t0} \rightarrow RO_{1,t1}$ and $RO_{3,t0} \rightarrow RO_{3,t1}$ in Figure 7.7.
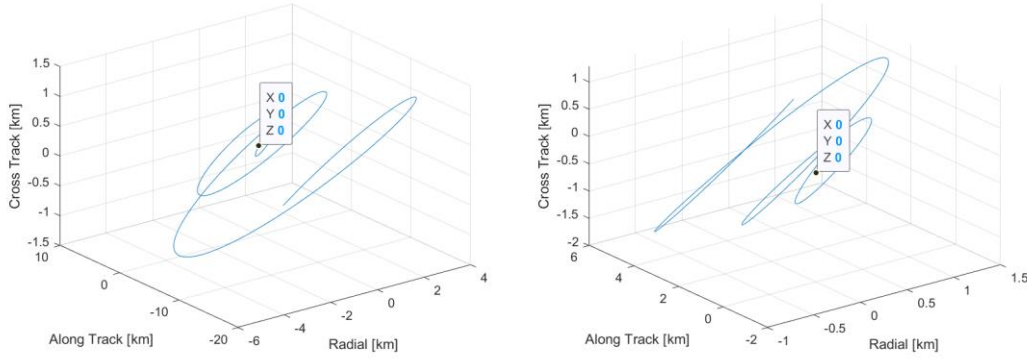
Figure 7.7. Relative Trajectory of LTI NOC Reconfiguration $RO_{1,t0} \rightarrow RO_{1,t1}$ (Left) and $RO_{3,t0} \rightarrow RO_{3,t1}$ (Right).
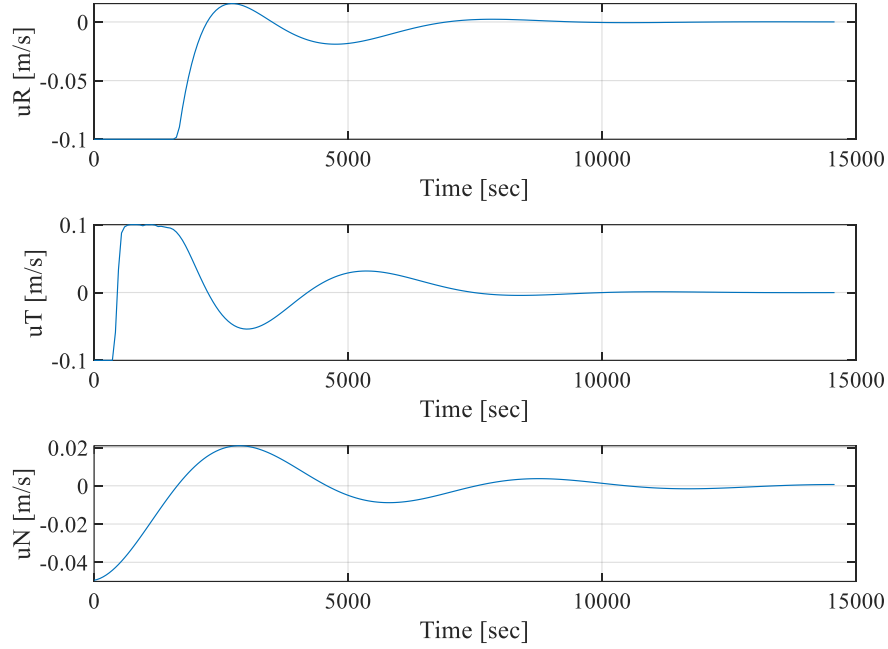
From the ΔV map given in Table 7.7, minimum total maneuvering effort is obtained if the reconfiguration is performed as follows: $RO_{1,t0} \rightarrow RO_{1,t1}$, $RO_{2,t0} \rightarrow RO_{2,t1}$, $RO_{3,t0} \rightarrow RO_{3,t1}$, $RO_{4,t0} \rightarrow RO_{5,t1}$, $RO_{5,t0} \rightarrow RO_{4,t1}$. Here, the solution with minimum maneuvering effort for the cluster results in 29.9 m/sec of total ΔV. From the Figure 7.7, it can be seen that the solution is found with relative distance diminished at the terminal time instant. Also, the maximum control input is bounded by 0.1 m/sec and the maximum thrust level required is less than 0.04 N for a 100 kg satellite with step size of 60 seconds.

When OIT and LTI NOC methodologies are compared, it can be observed that the LTI NOC requires more maneuvering effort (about 1.3 times of the impulsive transfer requirement) as expected. However, with LTI NOC, it is possible to put constraints on control inputs based on thruster limitations and find solutions where impulsive transfer is not possible. While it takes half an orbit for impulsive transfer to be realized, it takes around 3 orbits for LTI NOC solution to complete reconfiguration. The total cost, i.e. the maneuvering effort, can be reduced by increasing the transfer time, however, it needs to be checked for safety conditions (Eq. (59)) continuously. Finally, LTI NOC reconfiguration results in less computational demand (as there is no extensive dynamics calculation for prediction horizon) and less total ΔV when compared to LTI MPC reconfiguration.

142

In order to introduce the effects of realistic dynamics, the LTI system dynamics, $f(x_k, u_k)$, in Table 7.6 can be replaced with J2 incorporated relative STM provided with Eq. (47). With the use of this STM, the states would become the quasi non-singular mean relative orbital elements as described in Eq. (46). However, as the objective for orbital transfer is the minimization of the relative state error with respect to target orbit, the constraint for terminal time instant would be similar to the LTI NOC formulation and full constraints can be given as in the Eq. (91).

$$x_{k+1} = \Delta\alpha_{k+1}^{qns} = f(x_k, u_k),$$
$$x_{N+1} = \Delta\alpha_{N+1}^{qns} = [0 \quad 0 \quad 0 \quad 0 \quad 0 \quad 0]^T, \tag{91}$$
$$u_{min} \leq u_k \leq u_{max}.$$

With these, the final formulation for the resulting LTV system NOC is summarized in Table 7.8.

Table 7.8 Orbital Transfer Formulation with LTV System NOC

Parameter	*Specification*
Objective Function	Minimize Eq. (89)
Constraint Function(s)	Eq. (91)
System Dynamics	Eq. (47), (49) and (50)
Time Step	60 sec.
Simulation Duration	N =300 steps (~3 orbits)
Bounds on ΔV Input	u_{min} = -0.1 m/sec, u_{max} = 0.1 m/sec

Using these settings, the solution found in Figure 7.3 is recalculated and the resulting ΔV map is given in Table 7.9. These solutions are all achieved with the satisfaction of the constraints with $\Delta\alpha_{N+1}^{qns} = [0 \quad 0 \quad 0 \quad 0 \quad 0 \quad 0]^T$ meaning that spacecraft are totally transferred to the target orbit.

Table 7.9 ΔV Map for the Reconfiguration of 5 Spacecraft Cluster with LTV NOC

ΔV [m/sec]	$RO_{1,t1}$	$RO_{2,t1}$	$RO_{3,t1}$	$RO_{4,t1}$	$RO_{5,t1}$
$RO_{1,t0}$	**3.56**	8.82	12.56	13.92	19.44
$RO_{2,t0}$	11.59	**3.06**	7.80	9.31	11.61
$RO_{3,t0}$	11.74	5.75	**2.54**	5.52	7.82
$RO_{4,t0}$	17.12	8.83	7.81	7.81	**7.16**
$RO_{5,t0}$	4.01	6.30	9.78	**11.41**	16.60

From the ΔV map given in Table 7.7, minimum total maneuvering effort is obtained if the reconfiguration is performed as follows: $RO_{1,t0}$ → $RO_{1,t1}$, $RO_{2,t0}$ → $RO_{2,t1}$, $RO_{3,t0}$ → $RO_{3,t1}$, $RO_{4,t0}$ → $RO_{5,t1}$, $RO_{5,t0}$ → $RO_{4,t1}$. Here, the solution with minimum maneuvering effort for the cluster results in 27.73 m/sec of total ΔV. Also, the maximum control input is bounded by 0.1 m/sec and the maximum thrust level required is still less than 0.04 N for a 100 kg satellite with step size of 60 seconds.

When OIT and LTV NOC methodologies are compared, it can be observed that the LTV NOC still requires more maneuvering effort (about 1.2 times of the impulsive transfer requirement) as expected. However, with LTV NOC, it is possible to put constraints on control inputs based on thruster limitations and find solutions where impulsive transfer is not possible. While it takes half an orbit for impulsive transfer to be realized, it takes around 3 orbits for NOC solution to complete reconfiguration. The total cost, i.e. the maneuvering effort, can be reduced by increasing the transfer time, however, it needs to be checked for safety conditions (Eq. (59)) continuously. Finally, LTV NOC reconfiguration results in less computational demand (as there is no extensive dynamics calculation for prediction horizon) and less total ΔV when compared to LTI MPC reconfiguration.

7.4   Evaluation of Reconfiguration Methodologies

In terms of reconfiguration, several methodologies and dynamics models are applied as described in previous chapters. Here, the summary of the results of reconfiguration methodologies for 5 spacecraft cluster is given in the Table 7.10.

Table 7.10 Summary of Reconfiguration Results for 5 Spacecraft Cluster

Methodology	Dynamics	Total ΔV [m/sec]	Notes
OIT	LTI	23	Transfer is not possible for 2 cases Impulsive and not limited control
MPC	LTI	36.8	All transfer is possible with limited control Transfer allocation is different from OIT
NOC	LTI	29.9	All transfer is possible with limited control Transfer allocation is same as OIT
NOC	LTV	27.7	All transfer is possible with limited control Transfer allocation is same as OIT

Since OIT with LTI system would provide the theoretical minimum ΔV requirement and minimum transfer time (half orbit), it can be taken as reference for comparisons. First of all, MPC and NOC makes transfer possible between all relative orbits where transfer is not possible with OIT. Also, MPC and NOC incorporates control constraints while control is not limited for OIT. Secondly, NOC solutions provide same reconfiguration order with OIT however transfer allocation is slightly different for MPC. Here, the MPC performance can be tuned to provide similar

reconfiguration order and ΔV requirements, however, the transfer duration (~3 orbits) is kept the same for MPC and NOC solutions for comparison reasons. Therefore, MPC performance may differ from OIT and NOC solutions for same transfer duration with NOC. Finally, as it can be seen from Table 7.10, the NOC with LTV provides the closest ΔV requirement to the theoretical minimum case. Considering these results, it can be concluded that the use of NOC improves the overall solution performance with the existence of control constraints.

In order to see the real-life implications of these solutions to spacecraft design, the propellant budgets are also calculated for a spacecraft with 100 kg mass and with liquid monopropellant propulsion system (MPS) whose specific impulse is 200 seconds. In addition, assuming that the reconfiguration is performed each 3 days, 122 reconfigurations shall be performed on average per year. The resulting propellant budget is summarized in Table 7.11.

Table 7.11 Propellant Budget for Spacecraft Reconfiguration

Methodology	Total ΔV per Reconfiguration [m/sec]	Average ΔV per Spacecraft [m/sec]	Average ΔV per Year per Spacecraft [m/sec]	Average Propellant per Year per Spacecraft [kg]
OIT-LTI	23	4.60	561.20	24.88
MPC-LTI	36.8	7.36	897.92	36.72
NOC-LTI	29.9	5.98	729.56	31.05
NOC-LTV	27.7	5.54	675.88	29.14

As it can be seen from Table 7.11, the total propellant requirement per year just for reconfiguration is considerable for a conventional 100 kg class spacecraft.

7.5 Sequential Cluster Design and Reconfiguration with Relative Orbit Element Differences as Design Variable

As described in the previous chapter, sequential spacecraft cluster design with completely new relative orbital elements results in considerable amount of total reconfiguration ΔV and propellant budget even though the objective is minimizing it with OIT methodology. Instead of designing completely new relative orbital elements, an alternative way is introducing small differences in relative orbital elements to the first configuration. In this approach, the differences between the relative orbital elements from initial cluster to the next one are directly considered as design variables. This is described in Figure 7.8 and new orbital elements of the spacecraft in the cluster are calculated using Eq. (92).
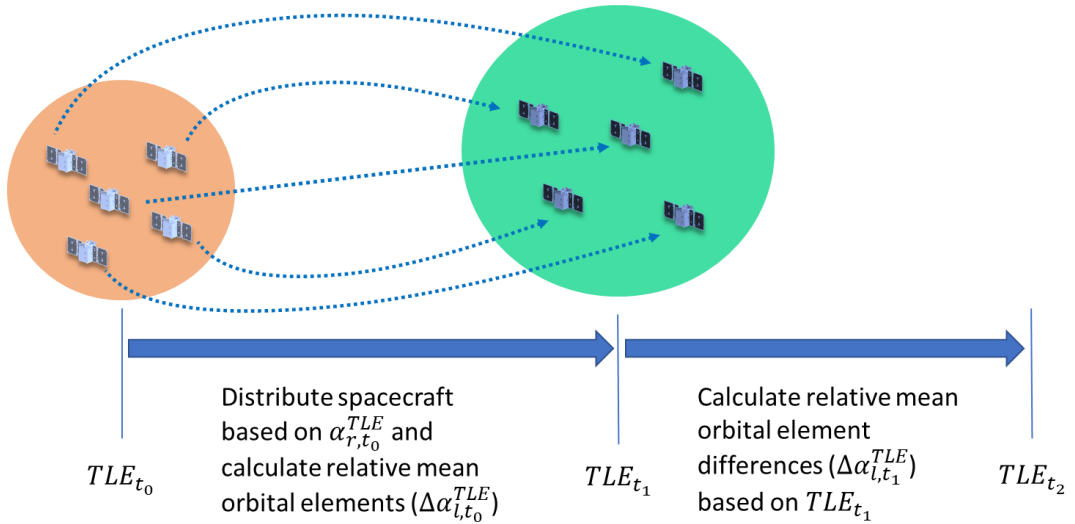
Figure 7.8. Implementation of Sequential Cluster Design and Reconfiguration with Relative Orbital Differences

$$\alpha_{l,t_1}^{TLE} = \left(\alpha_{r,t_1}^{TLE} + \Delta\alpha_{l,t_0}^{TLE}\right) + \Delta\alpha_{l,t_1}^{TLE} \tag{92}$$

Here, the differences in relative cross track elements, Δi and $\Delta\Omega$ are considered as design variables since the along-track elements can be controlled separately for each spacecraft. These design variables and their bounds are specified by the Eq. (93).

$$-0.001° \leq \Delta i_{l,t_1}^{TLE} \leq 0.001°$$
$$-0.001° \leq \Delta \Omega_{l,t_1}^{TLE} \leq 0.001° \tag{93}$$

In addition, the objective can still be selected as either to maximize station keeping or safety while reconfiguration ΔV is minimized for each spacecraft through nonlinear optimal control. Based on the previously utilized cluster flying objectives and newly introduced design variables, the reconfiguration of 5 spacecraft cluster studied in Chapter 7.1 is reformulated in Table 7.12.

Table 7.12 Reconfiguration Problem with Relative Orbital Element Differences as Design Variables

Parameter	*Specification*	
Objective Function	$Minimize \sum_{l=1}^{N} \sum_{j=1}^{T} \dfrac{\left(\Delta R_{l,j}^2 + \Delta T_{l,j}^2 + \Delta N_{l,j}^2\right)}{d_{max}^2}$	
Constraint Function(s)	Eq. (59)	
Bounds on Design Variables	Eq. (93)	
Propagator	Analytical (SGP4)	
Inputs and Assumptions	Reference Orbit	SSO, LTDN 10:30 at 685 km altitude
	Spacecraft Number	5
	d_{min} and d_{max} in RTN Plane	0.1 km and 20 km
	Physical Differences	Defined by $\Delta \beta_l^* = 0$
	Duration, T_{max}	3 days
	Step Size	10 sec
	Sample Number	1000

Based on this formulation, the resulting relative distances for $C_2^5 = 10$ combinations are shown in Figure 7.9.
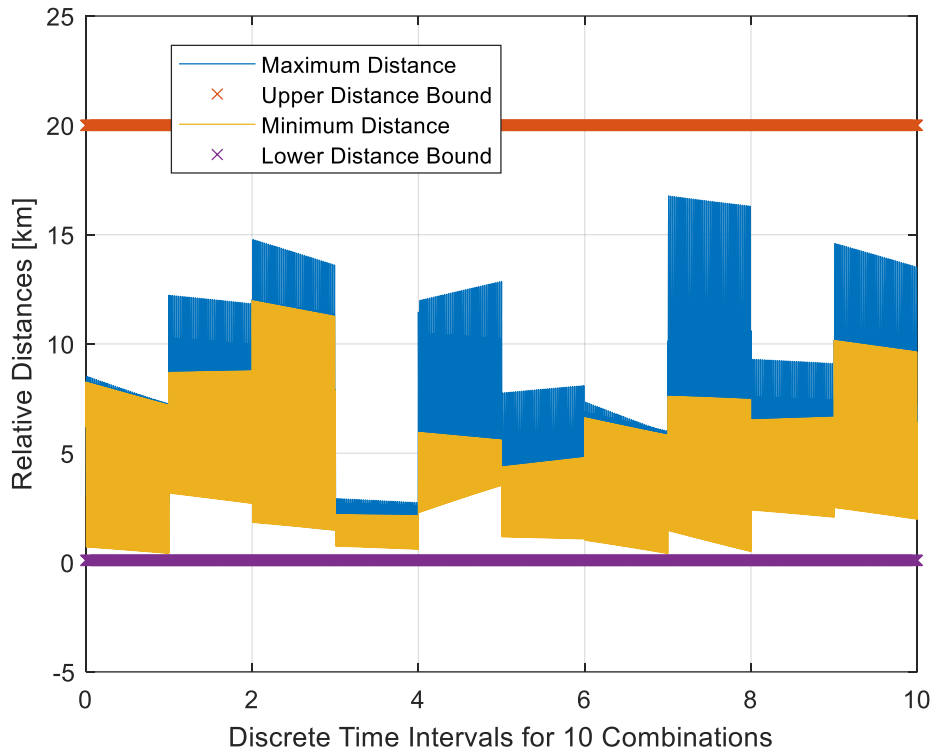
Figure 7.9. Cluster Flying 3 Day-Result for 5 Spacecraft with Relative Orbital Element Differences as Design Variable.

From Figure 7.9, it can be concluded that the 5-spacecraft cluster flying design does not violate the minimum and maximum distance constraints of 0.1 km and 20 km respectively over 3-day period. The minimum distance occurs as 0.4 km. in RN while corresponding RTN distance is 5 km. in the cluster. In addition, the minimum RTN distance occurs as 1.39 km. while corresponding RN distance is 1.14 km. Finally, the maximum relative distance in the cluster is 16.77 km.

Finally, the reconfiguration of 5 spacecraft cluster based on the modified relative orbital elements of the initial cluster with the formulation given in Table 7.8 results in the ΔV requirements which are summarized in Table 7.13. Here, it must be noted that the reconfiguration is performed for each spacecraft directly to its modified relative orbit without any re-allocation through auction algorithm.

Table 7.13 Summary of Reconfiguration Results for 5 Spacecraft Cluster with Relative Orbital Element Differences as Design Variable

Reconfiguration	Relative Orbital Element Difference: $[\Delta i_{l,t_1}^{TLE}, \Delta \Omega_{l,t_1}^{TLE}]$	ΔV [m/sec]
$RO_{1,t0} \rightarrow RO_{1,t1}$	$[9.15 \times 10^{-4}, 9.69 \times 10^{-4}]$	0.22
$RO_{2,t0} \rightarrow RO_{2,t1}$	$[7.09 \times 10^{-4}, -1.44 \times 10^{-4}]$	0.12
$RO_{3,t0} \rightarrow RO_{3,t1}$	$[9.72 \times 10^{-4}, -5.96 \times 10^{-4}]$	0.14
$RO_{4,t0} \rightarrow RO_{4,t1}$	$[-9.9 \times 10^{-4}, -8.42 \times 10^{-4}]$	0.22
$RO_{5,t0} \rightarrow RO_{5,t1}$	$[-1.93 \times 10^{-4}, 9.25 \times 10^{-4}]$	0.16
TOTAL		0.86

As it can be seen from this table, the total ΔV requirement is significantly improved by considering the relative orbital element differences as design variables. In addition, the propellant budgets are also given in Table 7.14 for spacecraft with 100 kg mass and with MPS whose specific impulse is 200 seconds.

Table 7.14 Propellant Budget for Spacecraft Reconfiguration with Relative Orbital Element Differences as Design Variables

Reconfiguration	Total ΔV per Reconfiguration [m/sec]	Total ΔV per Year [m/sec]	Total Propellant per Year [kg]
$RO_{1,t0} \rightarrow RO_{1,t1}$	0.22	26.84	1.36
$RO_{2,t0} \rightarrow RO_{2,t1}$	0.12	14.64	0.74
$RO_{3,t0} \rightarrow RO_{3,t1}$	0.14	17.08	0.87
$RO_{4,t0} \rightarrow RO_{4,t1}$	0.22	26.84	1.36
$RO_{5,t0} \rightarrow RO_{5,t1}$	0.16	19.52	0.99
TOTAL	0.86	104.92	5.32

As it can be seen from the Table 7.14, the total propellant requirement for each spacecraft for cluster maintenance is very reasonable. With the overall methodology, it is not only possible to keep cluster within distance constraints but also perform reconfiguration with reasonable maneuvering effort.

CHAPTER 8

CONCLUSION

In this thesis the problem of long term and safe cluster flying is addressed. To fill the gap between the formation flying and swarm missions, cluster flying is introduced with relatively loose geometry constraints and control accuracy requirements and more spacecraft were considered compared to formation flying which typically accommodates two spacecraft (a leader and a follower). In order to support long-duration semi-autonomous operations of such spacecraft clusters, a set of algorithms that enable the long-term station keeping, safety and reconfiguration of distance bounded multi-spacecraft clusters under realistic operational considerations are proposed. In terms of utilization of such algorithms, safety and availability through collision and evaporation avoidance as well as spacecraft physical characteristics, capabilities, navigation uncertainties and high-fidelity orbital dynamics are considered. The performances of the algorithms are shown and evaluated for different cases including design of multi-spacecraft homogeneous and heterogeneous clusters with relatively short relative distances as well as designing a spaceborne RF Geolocation cluster with long relative distance constraints. In this manner, three different problems with maximizing station-keeping or safety objective as well as minimizing dilution of precision are studied. While designing cluster flying configurations, the space-time boundaries are found and evaluated with respect to the derived performance metrics, or objective functions. In the case of reconfiguration of a cluster due to limited time validity or feasibility, different reconfiguration strategies with different methodologies and dynamics models are also studied. These reconfiguration methods, models and implementations are compared to find propellant optimum solutions for whole cluster.

For several scenarios and mission requirements, the station-keeping objective, mission duration and number of spacecraft in the cluster are analyzed and compared to evaluate the performance of the proposed cluster flying framework. First of all, long term and safe spacecraft clusters can be achieved and their time-space boundaries can be found. However, it is found that the number of feasible solutions varies with respect to cluster flying duration and number of spacecraft in the cluster. These two parameters are conflicting therefore an optimum choice has to be made by the mission designer. In this manner, it is observed that number of solutions exponentially decrease with increasing cluster flying duration and/or the number of spacecraft in the cluster. It is also observed that it is more likely to find solutions and optimize for homogeneous or heterogeneous clusters with 3 to 6 spacecraft for maximum distance constraints from 15 km. up to 50 km.. As it is expected, the cost function for station-keeping also increases exponentially with increasing cluster flying duration and/or the number of spacecraft in the cluster. In the case of safety, probability of collision is considered as a performance metric. It is found out that, maximum probability of collision within a cluster of 5 spacecraft may reach considerable levels (~0.001) if navigation uncertainties are moderate. However, this still depends on the operator's acceptable risk level decision based on the availabilities and capabilities. For instance, maximum probability of collision within a cluster of 5 spacecraft becomes ignorable if the navigation uncertainties are relatively low. If cluster design is performed for a specific mission, a specific performance measure and relative distance constraints can be also considered. This is also shown for a design of RF Geolocation cluster for which a specific cost function based on dilution of precision is developed. In addition, several configurations with 3 or 4 spacecraft are found and solution performances are evaluated. It is found that the algorithm is able to find optimum solution which does not vary over mission duration. However, the number of feasible solutions still decreases with increasing mission duration. Finally, two methodologies are considered for reconfiguration by utilizing sequential design of cluster configurations or by using relative orbital element differences as design variables.

154

Utilization of different dynamics models and optimal control methodologies are also considered, evaluated and compared. Based on the simulation results, nonlinear optimal control with linear time varying dynamics models requires the minimum maneuvering effort in the existence of control constraints. Also, utilizing cross-track relative orbital element differences as design variables significantly improves the maneuvering requirement for the cluster when compared to sequential design and reconfiguration of spacecraft clusters.

Within the proposed cluster flying framework, several original contributions are achieved. Firstly, a high-fidelity orbit propagation for cluster flying design is utilized which is a vital asset for real-life operational analysis. Secondly, heterogeneous systems with different physical parameters are considered to incorporate various types of spacecraft where cooperation of different space assets is required in the case of fractionated spacecraft architectures. Thirdly, the developed cluster flying design methodology supports time validity assessment which is an important capability for both design and operational analyses of distributed space systems. In addition, algorithms for identifying general time-space boundaries with less computational demand are also a part of this development. In terms of cluster flying design, safety as an objective through minimizing probability of collision is considered for the first time. Finally, reconfiguration algorithm that supports cluster's time-space validity through sequential design of clusters and propellant optimal reconfiguration in the case of violation of a safety and/or distance constraints is also proposed.

With this developed cluster flying design methodology and framework, it becomes possible to assess what type of clusters are operationally possible or not for a given set of parameters regarding constraints, availabilities, capabilities, physical characteristics, navigation uncertainties and mission requirements. In this manner, the framework is a powerful design and operational analysis tool for maximizing the feasibility and mission return of such cluster missions. Different types of clusters with different mission requirements can be designed and evaluated with reasonable or small computational demand for long term uninterrupted service and safety in all phases of distributed space missions.

In terms of future work, several improvements can be considered for the developed methodologies in this thesis. First of all, SGP4 is a very powerful model for analytical orbit propagation and it makes use of specific mean orbital elements called TLEs. However, the accuracy of this model is limited and the performance can be improved by studying specific analytical models associated with specific mean orbital elements. This may become especially important for missions demanding very short relative distances. Secondly, the uncertainty propagation is computationally demanding and therefore the cluster flying design with safety objective through probability of collision may become not practical for mission designer. Therefore, incorporation of computationally effective risk indicators for conjunction events can be studied further and assessed for cluster flying design. In addition, use of machine learning techniques for covariance or conjunction predictions can be evaluated. Thirdly, model predictive control technique can be improved and implemented for the reconfiguration incorporating time varying systems. Also, the utilization of solar sail or differential drag for the reconfiguration problem is very interesting to harness natural dynamics and therefor minimize the propellant requirements. Finally, finding cluster flying solutions considering Bellmann principle of optimality for whole mission lifetime can be interesting to achieve globally optimum solutions which may improve the "working" sub-optimal solutions.

REFERENCES

Akella, M. R., & Alfriend, K. T. (2000). Probability of Collision Between Space Objects. *Journal of Gudiance, Control, and Dynamics*, Vol. 23, No. 5, pp. 769-772.

Alfano, S., & Oltrogge, D. (2018). Probability of Collision: Valuation, Variability, Visualization, and Validity. *Acta Astronautica*, Vol.148, pp. 301-316.

Alfriend, K. T., & Yan, H. (2005). Evaluation and Comparison of Relative Motion Theories. *Journal of Guidance, Control, and Dynamics*, Vol. 28, No. 2, pp. 254-261.

Alfriend, K. T., Vadali, S. R., Gurfil, P., How, J., & Breger, L. (2010). *Spacecraft Formation Flying: Dynamics, Control and Navigation.* Oxford: Butterworth-Heinemann.

Alfriend, K., Akella, M., Lee, D., Frisbee, J., Foster, J., Lee, D., & Wilkins, M. (1999). Probability of Collision Error Analysis. *Space Debris*, Vol.1, No.1, pp. 21-35.

Andersson, J., Gillis, J., Horn, G., Rawlings, J. B., & Diehl, M. (2019). CasADi: a software framework for nonlinear optimization and optimal control. . *Mathematical Programming Computation*, Vol. 11, pp. 1–36.

Bertsekas, D. P. (1992). Auction Algorithms for Network Flow Problems: A Tutorial Introduction. *Computational Optimization and Applications*, Vol. 1, pp. 7-66.

Brouwer, D. (1959). Solution of the Problem of Artificial Satellite Theory without Drag. *Astronomical Journal*, Vol. 64, p. 378.

Brown, O., & Eremenko, P. (2006). The Value Proposition for Fractionated Space Architectures. *AIAA Space 2006.* San Jose, CA.

Campbell, M. E. (2005). Collision Monitoring within Satellite Clusters. *IEEE Transactions on Control Systems Technology*, Vol. 13, No. 1, pp. 42-55.

Chan, K. (2003). Improved Analytical Expressions for Computing Spacecraft Collision Probabilities. *Presentation at the AAS/AIAA Space Flight Mechanics Meeting, Paper No. 03-184*. Ponce, Puerto Rico.

Clohessy, W., & Wiltshire, R. (1960). Terminal Guidance Systems for Satellite Rendezvous. *Journal of Aerospace Sciences*, Vol. 27 pp. 653-658.

D'Amico, S., & Montenbruck, O. (2006). Proximity Operations of Formation-Flying Spacecraft Using an Eccentricity/Inclination Vector Separation. *Journal of Guidance, Control and Dynamics*, Vol. 29, No 3, pp. 554-563.

Eagle, D. (2021, July 22). *Optimal Impulsive Orbital Transfer*. Retrieved from MATLAB Central File Exchange: https://www.mathworks.com/matlabcentral/fileexchange/39160-optimal-impulsive-orbital-transfer

Eckstein, M., Rajasingh, C., & Blumer, P. (1989, November 6-10). Colocation Strategy and Collision Avoidance for the Geostationary Satellites at 19 Degrees West. Toulouse: International Symposium on Space Flight Dynamics.

Edlerman, E., & Gurfil, P. (2019). Cluster-Keeping Algorithms for the Satellite Swarm Sensor Network Project. *Journal of Spacecraft and Rockets*, Vol. 56, pp. 649-663.

Foster, J. L., & Estes, H. S. (1992, August). Parametric Analysis of Orbital Debris Collision Probability and Maneuver Rate for Space Vehicles. *NASA/JSC-25898*.

Funke, Q., Virgili, B., Braun, V., Flohrer, T., Krag, H., Lemmens, S., . . . Siminski, J. (2018). Operational Collision Avoidance at ESOC.

Gill, E. (2011). Control Approaches for Formations of Small Satellites. *NATO-RTO-EN-SCI-231*.

Hill, G. W. (1878). Researches in the Lunar Theory. *American Journal of Mathematics*, Vol. 1, pp. 5-26.

Hoots, F. R., Roehrich, R. L., & Kelso, T. (1988, December 31). Models for Propagation of NORAD Element Sets. *Spacetrack Report No. 3*. Colorado Springs, CO, USA: Office of Astrodynamics, Aerospace Defense Center.

Hur-Diaz, S., & O'Connor, B. (2014). Cluster Flight Application on System F6. *24th International Symposium on Space Flight Dynamics.* Laurel, MD.

Iman, R. L., Davenport, J. M., & Zeigler, D. K. (1980). *Latin hypercube sampling (program user's guide) [LHC, in FORTRAN].*

Iman, R., Helton J., C., & Campbell, J. E. (1981). An Approach to Sensitivity Analysis of Computer Models: Part I - Introduction, Input Variable Selection and Preliminary Variable Assessment. *Journal of Quality Technology*, Vol.13, No. 3, pp. 174-183.

Imre, S. E. (2006). *High Precision Relative Motion Modelling.* Surrey: University of Surrey.

Julier, S. J., & Uhlmann, J. K. (2002). Reduced Sigma Point Filters for the Propagation of Means and Covariances Through Nonlinear Transformations. *Proceedings of the 2002 American Control Conference* (pp. 887-892). Anchorage, AK: IEEE.

Julier, S. J., & Uhlmann, J. K. (2004). Unscented Filtering and Nonlinear Estimation. *Proceedings of the IEEE*, (pp. 401-422).

Julier, S. J., Uhlmann, J. K., & Durant-Whyte, H. F. (2000). A New Method for the Nonlinear Transformation of Means and Covariances in Filters and Estimators. *IEEE Transactions on Automatic Control*, Vol. 45, pp. 477-482.

Kaula, W. M. (1966). *Theory of Satellite Geodesy: Applications of Satellites to Geodesy.* New York: Dover.

Kirschner M., M. O. (2001). Flight Dynamics Aspects of the GRACE Formation Flying. *2nd International Workshop on Satellite Constellations and Formation Flying.* Haifa.

Koeing, A. W., & D'Amico, S. (2018). Robust and Safe N-Spacecraft Swarming in Perturbed Near-Circular Orbits. *Journal Of Guidance, Control, and Dynamics*, Vol. 41, No. 8, pp. 1643-1662.

Koenig, A. W., & D'Amico, S. (2019). Fast Algorithm for Fuel-Optimal Impulsive Control of Linear Systems with Time-Varying Cost. *IEEE Transactions on Automatic Control.*

Koenig, A. W., Guffanti, T., & D'Amico, S. (2016). New State Transition Matrices for Relative Motion of Spacecraft Formations in Perturbed Orbits. *AIAA/AAS Astrodynamics Specialist Conference.* Long Beach, CA.

Krag, H., Merz, K., Flohrer, T., Lemmens, S., Virgili, B. B., Funke, Q., & Braun, V. (2016). ESA's Modernised Collision Avoidance Service. *SpaceOps 2016 Conference.* Daejeon: AIAA.

Lee, G. (1964). An Analysis of Two-Impulse Orbital Transfer. *AIAA Journal*, Vol. 2, pp. 1767-1773.

Lim, Y., Jung, Y., & Bang, H. (2018). Robust model predictive control for satellite formation keeping with eccentricity/inclination vector separation. *Advances in Space Research*, Vol. 61, Issue 10, pp. 2661-2672.

McCue, G. A., & Bender, D. F. (1965). Numerical Investigation of Minimum Impulse Orbital Transfer. *AIAA Journal*, Vol. 3, pp. 2328-2334.

Mckay, M., Beckman, R., & Conover, W. (1979). A comparison of three methods for selecting values of input variables in the analysis of output from a computer code. *Technometrics*, Vol. 21, No. 2, pp. 239-245.

Mikkola, S. (1999). Efficient Symplectic Integration of Satellite Orbits. *Celestial Mechanics and Dynamical Astronomy*, 74 (4): 275–285.

Montenbruck, O. (2009). Orbital Mechanics. In W. Ley, K. Wittmann, & W. Halmann, *Handbook of Space Technology* (pp. 52-82). John Wiley & Sons.

Montenbruck, O., & Gill, E. (2011). *Satellite Orbits: Models, Methods, and Applications.* Springer.

Montenbruck, O., Kirschner, M., D'Amico, S., & Bettadpur, S. (2006). E/I-Vector Separation for Safe Switching of the GRACE Formation. *Aerospace Science and Technology*, Vol. 10, pp. 628-635.

Morgan, D., Chung, S., & Hadaegh, F. Y. (2014). Model Predictive Control of Swarms of Spacecraft Using Sequential Convex Programming. *Journal of Guidance, Control, and Dynamics*, Vol. 37, No. 6, pp. 1725-1740.

Morgan, D., Subramanian, P., G., Chung, S.-J., & Hadaegh, F. Y. (2016). Swarm Assignment and Trajectory Optimization Using Variable-Swarm, Distributed Auction Assignment and Sequential Convex Programming. *International Journal of Robotics Research*, Vol. 35, No. 10; pp. 1261-1285.

Mueller, J. B., Griesemer, P. R., & Thomas, S. J. (2013). Avoidance Maneuver Planning Incorporating Station-Keeping Constraints and Automatic Relaxation. *Journal of Aerospace Information Systems*, Vol. 10, No. 6, pp. 306-322.

Nadav, M., & Gurfil, P. (2022). Constellation Design for Regional Space-Borne Geolocation. *Journal of Guidance, Control, and Dynamics*, Vol. 45, No. 5, pp. 795*814.

NOAA NESDIS. (2022, July 10). Retrieved from Geomagnetic kp and ap Indices: https://www.ngdc.noaa.gov/stp/GEOMAG/kp_ap.html

NOAA SWPC. (2022, July 10). Retrieved from F10.7 cm Radio Emissions: https://www.swpc.noaa.gov/phenomena/f107-cm-radio-emissions

NOAA SWPC. (2022, July 10). Retrieved from Satellite Drag: https://www.swpc.noaa.gov/impacts/satellite-drag

Ortiz Longo, C. R., & Rickman, S. L. (1995, April). Method for the Calculation of Spacecraft Umbra and Penumbra Shadow Terminator Points. Houston, TX: NASA Technical Paper 3547.

Paek, S. W., Kim, S., & de Weck, O. L. (2019). Optimization of Reconfigurable Satellite Constellations Using Simulated Annealing and Genetic Algorithm. *Sensors*, Vol. 19, No. 4, pp. 765.

Patera, R. P. (2003). Satellite Collision Probability for Nonlinear Relative Motion. *Guidance, Control and Dynamics*, Vol. 26, No. 5, pp. 728-733.

Pengfei, L., Xiaoqian, C., & Yong, Z. (2019). Safe deployment of cluster-flying nano-satellites using relative E/I vector separation. *Advances in Space Research*, Vol. 64, Issue 4, pp. 964-981.

Persson, S., D'Amico, S., & Harr, J. (2010). Flight Results From PRISMA Formation Flying and Rendezvous Demonstration Mission. *61st International Astronautical Congress*, (pp. IAC-10-D9.2.8). Prague.

Picone, J. M., Hedin, A. E., & Drob, D. P. (2002). NRLMSISE-00 Empirical Model of the Atmosphere: Statistical Comparisons and Scientific Issues. *Journal of Geophysical Research*, SIA 15-1-SIA 15-16.

Sarda, K., Roth, N., Zee, R. E., CaJacob, D., & Orr, N. G. (2018). Making the Invisible Visible: Precision RF-Emitter Geolocation from Space by the HawkEye 360 Pathfinder Mission. *AIAA/USU Conference on Small Satellites*, (pp. SSC18-II-06).

Scharf, D. P., Hadaegh F., Y., & Ploen, S. R. (2004). A Survey of Spacecraft Formation Flying Guidance and Control. Part II: Control. *Proceedings of the 2004 American Control Conference,*, (pp. 2976-2985). Boston, MA.

Scharf, D. P., Hadaegh, Y., F., & Ploen, S. R. (2003). A Survey of Spacecraft Formation Flying Guidance and Control (Part 1): Guidance. *Proceedings of the 2003 American Control Conference*, (pp. 1733-1739). Denver, CO.

Schaub, H., & Junkins, J. L. (2003). *Analytical Mechanics of Space Systems.* Reston, VA: AIAA.

Selva, D., Golkar, A., Korobova, O., Cruz, I., Collopy, P., & de Weck, O. (2017). Distributed Earth satellite systems: What is needed to move forward? *Journal of Aerospace Information Systems*, Vol. 14, No. 8, , pp. 412-438.

Sullivan, J., Grimberg, S., & D'Amico, S. (2017). Comprehensive Survey and Assessment of Spacecraft Relative Motion Dynamics Models. *Journal of Guidance, Control and Dynamics*, Vol. 40, No. 8, pp 1837-1859.

Tillerson, M., Inalhan, G., & How, J. P. (2002). Coordination and control of distributed spacecraft systems using convex optimization techniques. *Journal of Robust and Nonlinear Control*, Vol. 12, No. 2-3, pp. 207-242.

Vallado, D. A. (2013). *Fundamentals of Astrodynamics and Applications.* Hawthorne: Microcosm Press.

Wächter, A., & Biegler, L. T. (2006). On the implementation of an interior-point filter line-search algorithm for large-scale nonlinear programming. *Mathematical Programming*, Vol. 106, pp. 25–57.

Wan, E. A., & van der Merwe, R. (2001). The Unscented Kalman Filter for Nonlinear Estimation. In E. S. Haykin, *Kalman Filtering and Neural Networks* (pp. 221-279). John Wiley & Sons, Inc.

Wang, J., & Nakasuka, S. (2012). Cluster flight orbit design method for fractionated spacecraft. *Aircraft Engineering and Aerospace Technology*, Vol. 84, No. 5, pp. 330-343.

Wang, W., Mengali, G., Quarta, A. A., & Yuan, J. (2017). Formation flying for electric sails in dis-placed orbits. Part I: Geometrical analysis. *Advances in Space Research*, Vol. 60, Issue 6, pp. 1115-1129.

Wen, C., Zhang, H., & Gurfil, P. (2015). Orbit Injection Considerations for Cluster Flight of Nanosatellites. *Journal of Spacecraft and Rockets,*, Vol. 52, No. 1, pp. 196-208.

Xin, L. (2015). *Monte Carlo analysis II: Latin hypercube sampling & importance sampling, Lecture25*. Retrieved from Numerical Methods for Engineering Design and Optimization (18-660 @ CMU): https://users.ece.cmu.edu/~xinli/classes/cmu_18660/Lec25.pdf

Yaglioglu, B. (2011). A Fractionated Spacecraft Architecture for Earth Observation Missions. *Master Thesis*. Sweden: Lulea University of Technology, Department of Computer Science, Electrical and Space Engineering.

Yaglioglu, B., & Wang, J. (2011). Cluster Flying Configuration Evaluation in the Case of Fractionated Spacecraft Architecture. *Proceedings of the 6th Ankara International Aerospace Conference,*, (s. Paper No. AIAC-2011-075.). Ankara, Turkey.

Ya-zhong, L., & Zhen, Y. (2017). A Review of Uncertainty Propagation in Orbital Mechanics. *Progress in Aerospace Sciences*, 262-268.

Yoshida, H. (1990). Construction of Higher Order Symplectic Integrators. *Physics Letters A*, 150: 262–268.

Zhang, Y., Dang, Z., Fan, L., & Wang, Z. (2017). A rapid method for calculating maximal and mini-mal inter-satellite distances. *Advances in Space Research,*, Volume 59, Issue 1, pp. 401-412.

Zhong, W., & Gurfil, P. (2013). Mean Orbital Elements Estimation for Autonomous Satellite Guidance and Orbit Control. *Journal of Guidance, Control and Dynamics*, Vol. 36, No. 6, pp. 1624-1641.

A. Two-Impulse Optimal Transfer

In this annex, the technical notes by (Eagle, 2021) for the implementation of two-impulse optimal transfer between non-coplanar circular and elliptical orbits which is utilized in Chapter 7.1 are provided for reference.

The formulation of the two-impulse optimal transfer is based on a reference coordinate system whose fundamental reference plane is the final orbit plane and the x-axis is aligned with the intersection of the planes of initial and final orbits. The z-axis of the system is aligned with the angular momentum vector of the final orbit and the y-axis completes this orthogonal coordinate system. The geometry of the two impulse orbital transfer is provided in Figure A.1.
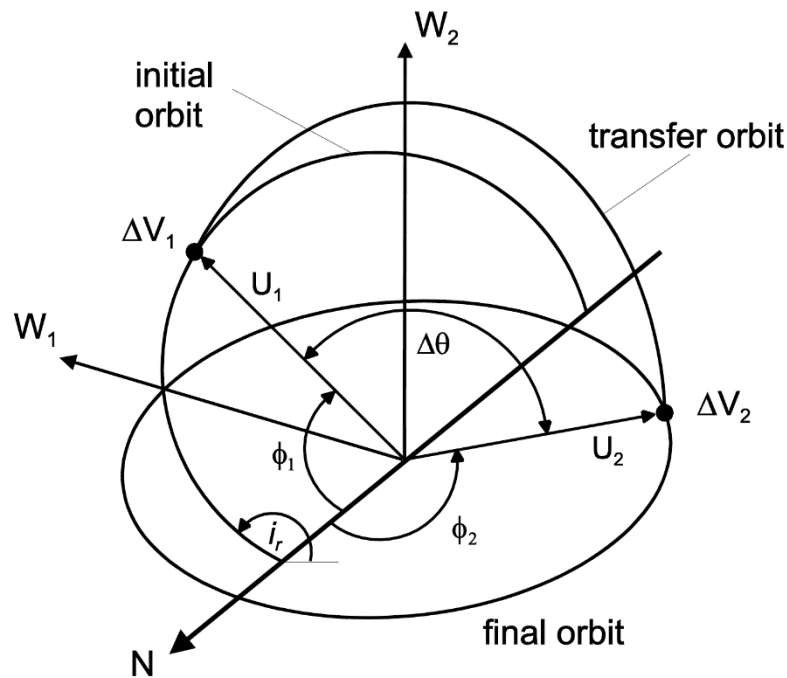
Figure A.1. The geometry of two-impulse optimal transfer between non-coplanar circular and elliptical orbits. (Eagle, 2021)

In Figure A.1, i_r represents the relative inclination between the initial and final orbit planes, $\Delta\theta$ is the is the transfer angle which is the angle from the first and second impulse measured in the plane of the transfer orbit. **N** is in the direction of the x-axis, **W₁** is in the direction of the initial orbit angular momentum vector, and **W₂** is in the direction of the angular momentum vector of the final orbit.

The independent variables for this problem are ϕ_1, ϕ_2 and p_t , where ϕ_1 is the angle from the N axis to the first impulse as measured in the initial orbit plane, ϕ_2 is the angle from the N axis to the second impulse as measured in the final orbit plane, and p_t is the semi-parameter of the transfer orbit. The expression for N is provided in the

$$N = \frac{W_1 \times W_2}{|W_1 \times W_2|} \tag{94}$$

where $W_1 = [0 \quad -\sin i_r \quad \cos i_r]^T$ and $W_1 = [0 \quad 0 \quad 1]^T$. Here the relative inclination i_r is determined from

$$i_r = \cos^{-1}(w_1 \cdot w_2) \tag{95}$$

where w_k (k is 1 or 2) is the ECI unit angular momentum vector of the initial orbit given by

$$w_k = \begin{bmatrix} \sin \Omega_k \sin i_k \\ -\cos \Omega_k \sin i_k \\ \cos i_k \end{bmatrix} \tag{96}$$

The unit position vector at the first impulse in the reference coordinate system is

$$U_1 = \begin{bmatrix} \cos \phi_1 \\ \sin \phi_1 \cos i_r \\ \sin \phi_1 \sin i_r \end{bmatrix} \tag{97}$$

and the unit position vector of the second impulse, also in the reference coordinate system, is determined from

$$U_2 = \begin{bmatrix} \cos \phi_2 \\ \sin \phi_2 \\ 0 \end{bmatrix} \tag{98}$$

The transfer angle can be computed from the following dot product

$$\Delta\theta = \cos^{-1}(U_1 \cdot U_2) \tag{99}$$

The minimum and maximum bounds on the semi-parameter of the transfer orbit can be determined from the following two expressions

$$
\begin{aligned}
p_{min} &= \frac{r_1 r_2 - \boldsymbol{r_1} \cdot \boldsymbol{r_2}}{r_1 + r_2 + \sqrt{2(r_1 r_2 + \boldsymbol{r_1} \cdot \boldsymbol{r_2})}} \\
p_{max} &= \frac{r_1 r_2 - \boldsymbol{r_1} \cdot \boldsymbol{r_2}}{r_1 + r_2 - \sqrt{2(r_1 r_2 + \boldsymbol{r_1} \cdot \boldsymbol{r_2})}}
\end{aligned}
\tag{100}
$$

The partial derivative of the total required ΔV with respect to the semi-parameter of the transfer orbit is as follows

$$\frac{\partial V_t}{\partial p_t} = \frac{1}{2p_t}\left(\frac{\Delta \boldsymbol{V_1} \cdot (\boldsymbol{V} - z\boldsymbol{U_1})}{|\Delta \boldsymbol{V_1}|} - \frac{\Delta \boldsymbol{V_2} \cdot (\boldsymbol{V} + z\boldsymbol{U_2})}{|\Delta \boldsymbol{V_2}|}\right) \tag{101}$$

Part of the optimal orbital transfer solution involves finding the value of p_t which lies between p_{min} and p_{max} which makes this partial derivative expression equal to zero.

The $\Delta \boldsymbol{V}$ vectors in the reference coordinate system are given by the following two expressions

$$
\begin{aligned}
\Delta \boldsymbol{V_1} &= \mp(\boldsymbol{V} + z\boldsymbol{U_1}) - \boldsymbol{V_1} \\
\Delta \boldsymbol{V_2} &= \boldsymbol{V_2} \mp (\boldsymbol{V} - z\boldsymbol{U_2})
\end{aligned}
\tag{102}
$$

where the upper sign in these two equations corresponds to the short transfer and

$$z = \sqrt{\frac{\mu}{p}}\tan\frac{\Delta\theta}{2} \tag{103}$$

with

$$\boldsymbol{V} = \sqrt{\mu\, p_t}\,\frac{(\boldsymbol{r_2} - \boldsymbol{r_1})}{|\boldsymbol{r_1} \times \boldsymbol{r_2}|} \tag{104}$$

The velocity vector of the satellite prior to the first ($k = 1$) or second ($k = 2$) impulse with respect to the reference coordinate system is calculated from

167

$$V_k = \sqrt{\frac{\mu}{p_k}}\, W_k \times (e_k + U_k) \qquad (105)$$

In these expressions, e_1 is the reference coordinate system eccentricity vector of the initial orbit which is given by

$$e_1 = e_1[\cos\omega_1 \quad \sin\omega_1 \cos i_r \quad \sin\omega_1 \sin i_r]^T \qquad (106)$$

and e_2 is the eccentricity of the final orbit defined by

$$e_2 = e_2[\cos\omega_2 \quad \sin\omega_2 \quad 0]^T \qquad (107)$$

where e_1 and e_2 are the scalar eccentricity of the initial and final orbits, respectively.

The total scalar delta-v required for the orbit transfer is given by $\Delta V = |\Delta V_1| + |\Delta V_2|$. The objective is to minimize this scalar quantity of ΔV which can be described by the ECI components of the two as follows:

$$\Delta V = \sqrt{\Delta V_{1x}^2 + \Delta V_{1y}^2 + \Delta V_{1z}^2} + \sqrt{\Delta V_{2x}^2 + \Delta V_{2y}^2 + \Delta V_{2z}^2} \qquad (108)$$

Here, to convert from reference coordinate system solution to ECI vectors, the transformation matrix β_{rcs}^{ECI} can be written as follows:

$$\beta_{rcs}^{ECI}$$
$$= \begin{bmatrix} \cos\Omega_2\cos\emptyset - \sin\Omega_2\cos i_2\sin\emptyset & -\cos\Omega_2\sin\emptyset - \sin\Omega_2\cos i_2\cos\emptyset & \sin\Omega_2\cos i_2 \\ \sin\Omega_2\cos\emptyset + \cos\Omega_2\cos i_2\sin\emptyset & -\sin\Omega_2\sin\emptyset + \cos\Omega_2\cos i_2\cos\emptyset & -\cos\Omega_2\sin i_2 \\ \sin i_2\sin\emptyset & \sin i_2\cos\emptyset & \cos i_2 \end{bmatrix} \qquad (109)$$

where

$$\emptyset = \cos^{-1}(N \cdot U)\, sign(N_z) \qquad (110)$$

and

$$U = [\cos\Omega_2 \quad \sin\Omega_2 \quad 0]^T \qquad (111)$$

The position vector of the initial and transfer orbits at the first impulse ($k = 1$) and the position vector of the transfer and final orbit at the second impulse ($k = 2$) in the reference coordinate system is

$$r_k = \left(\frac{p_k}{1 + e_k \cos(\phi_k - \omega_k)} \right) \tag{112}$$

In these equations the arguments of perigee ω_1 and ω_2 are with respect to the reference coordinate system. They can be determined with the following three equations

$$\omega_{rcs} = \beta_{rcs}^{ECI} \omega_{ECI}$$

$$\omega_1 = \cos^{-1} \omega_x \tag{113}$$

$$\omega_2 = \tan^{-1}(\omega_y, \omega_z)$$

where the inverse tangent calculation here is a four-quadrant operation. Then the ECI argument of perigee vectors ($k = 1,2$) at each impulse are given by

$$\omega_{ECI,k} = \begin{bmatrix} \cos \omega_k \cos \Omega_k - \sin \omega_k \sin \Omega_k \cos i_k \\ \cos \omega_k \sin \Omega_k + \sin \omega_k \cos \Omega_k \cos i_k \\ \sin \omega_k \sin i_k \end{bmatrix} \tag{114}$$

where all the orbital elements in these two equations are with respect to the ECI.

The semi-parameter of the initial ($k = 1$) and final ($k = 2$) orbit can be determined from

$$p_k = a_k(1 - e_k^2) \tag{115}$$

where a_k is the semi-major axes of the initial and final orbits.

The transfer orbit velocity vectors prior to the first and second impulses in the reference coordinate system are calculated from the next two equations

$$V_{t_1} = V + zU_1, \qquad V_{t_2} = V - zU_2 \tag{116}$$

The transfer orbit position and velocity vectors can be transformed into the ECI coordinate system using the transpose of the β_{rcs}^{ECI} matrix as described above, and then converted to classical orbital elements.

CURRICULUM VITAE

Surname, Name: Yağlıoğlu, Burak

EDUCATION

Degree	Institution	Year of Graduation
MS (Double Degree)	Lulea University of Technology (LTU) Computer Science, Electrical and Space Engineering	2011
MS (Double Degree)	Julius Maximilians University of Würzburg (JMUW) Department of Informatics, Chair of Robotics and Telematics	2011
BS	Middle East Technical University (METU) Aerospace Engineering	2008
High School	Bolu Science High School, Bolu	2003

PROFESSIONAL EXPERIENCE

Year	Place	Enrollment
2011-Present	TUBITAK UZAY – Space Technologies Research Institute	Researcher
2018-2020	UTAA Astronautical Engineering	Part Time Lecturer

RESEARCH INTERESTS

Space Mission Design and Analysis, System Design and Optimization, Spaceflight Operations, Orbital Mechanics, Modeling, Estimation and Control of Orbital Motion

FOREIGN LANGUAGES

English, German (Basic)

PUBLICATIONS

1. **Yağlıoğlu B**., Tekinalp O., "Long Term and Safe Relative Orbit Design for Heterogeneous Spacecraft Clusters", Advances in Space Research, 67(11), 3546-3558, 2021.
2. **Yağlıoğlu, B.**, "Türkiye'nin Ay Görevi ve Hedefleri", Anahtar, 396, 22-24, Aralık 2021.
3. **Yağlıoğlu B**., Tekinalp O., "Long Term and Safe Reconfiguration for Spacecraft Clusters", 31st AAS/AIAA Astrodynamics Specialist Conference, Big Sky, Virtual, 9-11 August 2021.
4. **Yağlıoğlu B**., Khesroh,M., Senturk, N., Tasdemir, M., Abramovich, R., Atasever, T., "Spacefaring Future of the Middle East: The Role of Moon Missions", IAC-20-A3-2C-20, The 71st International Astronautical Congress, 12-14 October 2020.
5. Canbulut, E., Aydıngül, V., **Yağlıoğlu B.**, "Application of Model Based Systems Engineering to a Small Satellite Project", Ankara International Aerospace Conference 2019, Ankara, Türkiye, September 18-20, 2019
6. Köprücü, Ş., U., Ozcelik, H., A., Altunay, S., **Yağlıoğlu B.**, "A Mission Analysis Software for Small Satellites", Ankara International Aerospace Conference 2019, Ankara, Türkiye, September 18-20, 2019
7. **Yağlıoğlu B**., Tekinalp O., "Long Term and Safe Relative Orbit Design for Heterogeneous Spacecraft Cluster", IWSCFF 19-1958, The 10th International Satellite Constellations and Formation Flying Workshop (IWSCFF'19), Glasgow, UK, 16-19 July 2019.
8. **Yağlıoğlu B**., Tekinalp O., "Passively Safe Relative Orbit Configurations Over Long Time Intervals for Heterogeneously Distributed Spacecraft Clusters", The 8th European Conference for Aeronautics and Space Sciences (EUCASS), Madrid, Spain, 1-4 July 2019.
9. Saka, Y., Paça, O., Özdemir, G., T., Korkut, B., Ataş, Ö., **Yağlıoğlu, B.**, "Characterization of a Geostationary Satellite Thruster Plumes Using Response Surface Generation", IEEE Xplore/RAST 2019, Istanbul, Türkiye, 11-14 June 2019.
10. İmre, E., **Yağlıoğlu, B.**., Gokce, M., Aydın, S., Koker, A., Geden, M., R., Dag., E., Arberkli, F., "Orbital Dynamics System of TUBITAK UZAY for Earth Orbiting Spacecraft", IEEE Xplore/RAST 2019, Istanbul, Türkiye, 11-14 June 2019.
11. **Yağlıoğlu, B.**, Ataş, Ö., Kahraman, D., Köse, S., Tekinalp, O., Süer, M., "A Multi-National Multi-Institutional Education Framework: APSCO SSS-2B CubeSat Project ", IEEE Xplore/RAST 2019, Istanbul, Türkiye, 11-14 June 2019.
12. Dudak, C., Utku, A., **Yağlıoğlu, B.**, "Authorization of Commercial Communication Satellite Grounds for Promoting Turkish Data Relay System", ICSSC 2106: 18th International Conference on Satellite and Space Communication, London, UK, 23-24 June 2016.

13. **Yağlıoğlu B.**, "Effective and Sustainable Outreach of Space Science and Technology: Middle East and Central America Cases", IAC-15-B2.8, The 66th International Astronautical Congress, Jerusalem, Israel, 12-16 October 2015.
14. Kara O., Brunner M., Birkeland R., Schor D., **Yağlıoğlu B.**, Smith T., Hornig A., "Communication Architecture and International Policy Recommendations Enabling the Development of Global CubeSat Space Networks", IAC-15-B2.8, The 66th International Astronautical Congress, Jerusalem, Israel, 12-16 October 2015.
15. Findlay R., Kayıhan A., Lu Z., **Yağlıoğlu B.**, Yeh J., "Space for Humanitarian Relief: The Centre for Responsive Information for Safety and Security (CRISIS)", IAC-13-E5.5.5, The 64th International Astronautical Congress, Beijing, China, 23-27 September 2013.
16. **Yağlıoğlu, B.**, Yılmaz, Ö., Utku, A., Özdemir, B.G., "Surveillance of Space: an Overview and a Vision for Turkey's Roadmap", IEEE Xplore/RAST 2013, Istanbul, Türkiye, 12-14 June 2013.
17. Türkmenoğlu, M., **Yağlıoğlu, B.**, "On-Orbit Modulation Transfer Function Estimation for RASAT", IEEE Xplore/RAST 2013, Istanbul, Türkiye, 12-14 June 2013.
18. **Yağlıoğlu B.,** Kutdemir E., Yılmaz Ö., İmre E., "Towards a European Collision Warning and Avoidance Centre", IAC-12-A6.6.9, The 63rd International Astronautical Congress, Naples, Italy, 1-5 October 2012.
19. **Yağlıoğlu B.**, İmre E., Tesmer, V., Scheper, M., "Mission Operations to Improve Space Mission Protection", 12th International Conference on Space Operations (SpaceOps'12), Stockholm, Sweden, 11-15 June 2012.
20. **Yağlıoğlu B.**, Nakasuka S., "A Fractionated Spacecraft Architecture for Earth Observation Missions", 32nd Asian Conference on Remote Sensing, Taipei,Taiwan, October 3-7, 2011.
21. **Yağlıoğlu B.**, Wang J., "Cluster Flying Configuration Evaluation in the Case of Fractionated Spacecraft Architecture", Ankara International Aerospace Conference 2011, Ankara, Türkiye, September 14-16, 2011.